PHD

Dynamic behaviour of masonry structures

Shi, Yanan

Award date:
2017

Awarding institution:
University of Bath

DYNAMIC BEHAVIOUR OF MASONRY STRUCTURES

YA-NAN SHI

A Thesis Submitted for the Degree of Doctor of Philosophy

University of Bath

Department of Architecture and Civil Engineering

November 2016

Table of Contents

Acknowledgements

I would like to thank my supervisor, Dr. D. F. D'Ayala, for her professional guidance during last few years. It is her scientific, patient and tolerant supervision that has led me to finish my doctoral studies and to finalize this thesis.

I would like to thank the Engineering and Physical Science Research Council (EPSRC) for awarding me a Dorothy Hodgkin Postgraduate Awards (DHPA) scholarship during 2005-2008 to support my doctoral studies.

I would like to thank Brian, Graham, Neil and Sophie in the structures laboratory, and Bernard Roe in the Department of Mechanical Engineering for their help with testing.

I would like to thank everyone who offered help, support and kindness to me in my life and studies during these years.

Last but not least, this thesis is jointly dedicated to my husband, Yi Wang, my parents and my parents in law who are always beside me, providing unconditional love, patience, edification and support.

Abstract

Masonry structures are especially vulnerable to earthquakes. Previous studies have focused mostly on their mechanical characteristics, while masonry structures vary greatly in terms of structural and material properties. This thesis aims to present the post-crack dynamic behaviour of masonry structures on mechanism. Systematic studies, including pseudo-static experiments, shaking-table experiments and mathematical modelling, were carried out.

In the pseudo-static experiments, scaled masonry walls with different geometric forms, bond types and corner connections were tested. The static-phase in-plane and out-of-plane damage mechanisms of masonry walls were classified. Their load factors and the influence of structural configurations were discussed. Experimental load factors are compared with theoretical ones derived from a limit-analysis procedure.

The shaking-table experiments successfully captured the dynamic-phase response mechanisms. Three 3D dry masonry models were tested according to sinusoidal excitation based on either constant amplitudes or constant peak accelerations. Conclusions on the dynamic behaviour of the masonry structure were presented. The experimental basis for the theoretical model was presented. The influence of structural configuration and excitation figure were clarified. The critical factors were clarified as being the excitation frequency and *L/H* ratio of the façade. The consistent damage behaviour variations arising from these two factors were analyzed.

A nonlinear dynamic mathematical model for the rocking of the masonry façade was developed, using a two-rigid-body model. The loads and frictional force on the top were included, with a horizontal excitation being applied. Assumptions of rigid ground, inelastic impact and point contact were applied. Six possible patterns were defined. The rocking, the impact and the possible transitions were formulated. Models in the shaking-table experiments were simulated to evaluate this model. Parametric studies were performed and future works were recommended.

Chapter 1 Introduction

Masonry is one of the oldest materials still used in the construction industry. This simple technique has been proved durable and successful. However, the properties of a masonry structure depend on “direction” because of the existence of joints between individual masonry blocks. This heterogeneity in a masonry structure makes for complex seismic behaviour.

The heavy damage inflicted on masonry structures by the earthquake of 1997 in Umbria-Marche, Italy, of 2005 in Kashmir, Pakistan, of 2008 in Wenchuan, China, and of 2010 in Darfield, New Zealand all especially emphasised the high seismic vulnerability of historic areas. Although complicated, intensive research on the seismic behaviour of masonry structures is, therefore, essential. The topic has only gained much attention since the 1990s, both experimentally and theoretically. Research objectives have included establishing mechanical characteristics, the response of typical components, damage patterns and repair and strengthening measures. Although considerable achievements have been made, systematic descriptions of the behaviour of common masonry structures subjected to seismic forces are very few. This is due to complexities in the structural, architectural and material characteristics of masonry structures throughout the world. These complexities create difficulties in drawing general conclusions on their seismic behaviour. It is considered more practical, therefore, to study the mechanisms which form in masonry after damage under seismic loading. Experimental and theoretical work on masonry subjected to static loads has provided much information but the dynamic load studies reported in the literature have not yet led to systematic conclusions.

The development of stress in the masonry structure during damage is complicated and varies according to the material and structural characteristics. However, cracks usually occur along the joints which are weak points in masonry structures under horizontal excitations. The mortar and its cohesion effect can be ignored at the post-crack stage. The mechanisms can be looked as the motions of a multi-rigid-body system. And by studying the topic in this way, we can get more generalized conclusions that can be applied to many masonry structures.

1.1 Objectives of the Research

This study is concerned with the dynamic behaviour of masonry structures when they reach the mechanism stage. The main emphasis is on the cracking process and the failure patterns in the walls and how and why they vary with different excitation parameters. Both experimental and mathematical studies have been carried out. The main objective is to describe the mechanisms which form in response to dynamic loads exerted on masonry structures, the characteristics of these mechanisms and their variation as produced by different excitation parameters and structural configurations. It will be possible to prove that the masonry structure can be looked as a rigid-body dynamic system through experimental studies. The mathematical model is expected to be based on application of rigid-body dynamics according to the experimental observations.

The objectives of this research are

- To identify the in-plane and out-of-plane damage mechanisms of masonry walls subjected to static loads by pseudo-static tests on scaled dry masonry walls. This work also aims to validate existing limit-analysis theoretical work on the failure mechanisms of masonry walls. The influences of the geometrical properties, the corner connections as well as on roof loadings of the masonry walls on their load bearing capacity to increasing horizontal forces needs to be summarised experimentally.
- To collect information on the post-crack behaviour of 3D masonry models under dynamic loading on a shaking table. This includes damage patterns and determining the influence of structural configuration and excitation parameters. The whole process of structural response when damaged by dynamic excitation is to be studied. The dynamic behaviour of different models should follow some consistent principles and yet variations with different structural configurations can be expected. Whether the discrete model responds globally needs to be verified. Any critical factors that determine the magnitude and mechanism of the responses must be clarified. The study will especially focus on out-of-plane rocking, which can be used as the basis of the mathematical model used in the theoretical study.
- To establish a dynamic mathematical model based on the dynamics of multi rigid bodies to describe the out-of-plane rocking behaviour of masonry structures. The two-rigid-body model is expected to be set up based on the experimental observations. The impact at joints, the transitions of response patterns at joints and the influence of constraints at the top of the walls need to be included. The model is expected to present consistent results with the shaking-table models. The characteristics of the rocking behaviour in the

theoretical model and the influences of the parameters are also expected to be analysed.

These three objectives are interrelated. The shaking-table experiments add value by modelling from pseudo-static to dynamic loading and from 2D cases to 3D cases. The experimental results, together with the previous theoretical studies based on limit analysis, provide an important basis for subsequent mathematical modelling work. Meanwhile, the theoretical model based on rigid-body dynamics also enables a theoretical study at dynamic performance.

1.2 Outline of the Thesis

Chapter 2, based on a literature study, gives an overview of past research on the dynamic behaviour of masonry structures. The achievements, the experiments and the theoretical work to date are all highlighted. The necessity to establish an experimental programme to illustrate the general dynamic behaviour of common masonry structures and to establish the systematic principles which govern variations in behaviour with different structural configurations and input parameters is highlighted. The possibilities and difficulties connected with the mathematical modelling work are illustrated.

In Chapter 3, results from pseudo-static experiments on dry masonry wall are presented. The dry masonry walls were constructed on a tilting table, with and without wings, with different geometrical ratios, with different connection conditions at the edges and different top-level loadings. Possible wall damage mechanisms and the corresponding load factors, caused by lateral forces, are given. Influence factors, representative of geometrical form, connecting condition and roof loading, are presented and analyzed in detail. Previous analytical work based on limit analysis is validated based on the experimental results.

In Chapter 4, dry masonry model shaking-table experimental program results are given. Three models, differing in corner constraint conditions and heights, are set up. A series of sinusoidal excitations with varying frequency are applied, respectively with constant peak acceleration and constant amplitudes. General dynamic behaviour mechanisms for common masonry structures are presented. Variations in the dynamic behaviour of masonry structure with facade height and corner constraint condition are illustrated. Whether the dynamic characteristics of a discrete masonry model vary globally is clarified. With the input sinusoidal signals varying in frequency, whether or not the level of dynamic response of a masonry structure is determined by displacement or by frequency is demonstrated. The excitations supplied separately along

the x and y axes also make it possible to compare the behaviour of different length facades in two orthogonal directions.

Chapter 5 is concerned with a dynamic mathematical model of the out-of-plane rocking of the masonry facade. The out-of-plane rocking in the masonry structure is modelled by the rigid rocking of a two-rigid-body system based on a series of assumptions, which is discontinuous with impact. The impact is assumed to be inelastic. Six possible rocking patterns are defined and the possible transitions between them after impact are formulated. Nonlinearities in the equations of motions and in conditions of transition are allowed. The shaking-table experiments models are given as examples. Theoretical and experimental results are compared. Parametric studies are then performed to further investigate the rocking characteristics.

In Chapter 6, final conclusions, drawn from the whole research study are given, summarizing the experimental results and the theoretical modelling. Limitations of the research are also discussed, generating suggestions for future work.

Chapter 2 Literature Review

2.1 Introduction

Masonry structures, due to their lack of ductility and their corresponding inability to dissipate energy through inelastic deformation, are very vulnerable to earthquakes. Research on the seismic behaviour of masonry structures increased in the 1990s. Relevant studies have been both theoretical and experimental in nature, based on different theoretical frameworks and focussing on many different factors affecting seismic behaviour. The research areas covered range from mechanical studies and simulations of seismic responses to effective strengthening and repair measures. Significant progress has been made around the world during these years. However, it is a relatively short period of time for a research area of great complexity. There are many issues still needing further research.

2.2 Review of Case Studies on Actual Masonry Buildings

As the most direct approach, extensive case studies on the states of damage of real masonry buildings after earthquakes have been carried out using various experimental techniques. For a complete on-site structural damage investigation an accurate geometrical survey must be carried out first. Afterwards, a crack pattern investigation should be performed. In addition, an analysis of the construction history is necessary to identify the structural building phases, the construction techniques used and possible strengthening interventions in the past. On-site case studies can provide abundant reliable knowledge of structural responses and offer effective strengthening suggestions. Seismic vulnerability assessment methodologies for masonry structures have been built up and validated by extensive case studies.

D'Ayala (1998) made a study of the historic churches and residential houses hit by the Umbria-Marche, Italy earthquake of 1997. The seismic behaviour and damage patterns are related to their particular typologies and strengthening devices. A vulnerability assessment model was developed based on calculation of shear capacity which proved to be effective.

Different types of structures in this earthquake were studied (Dolce, M., Masi et al. 1998). The poor quality of materials, the poor connections between the vertical components and floors, roofs outward thrusting and their poor connections to external walls have been identified as critical factors in the worst seismic performances. Lagomarsino (1998) then collected data from over 100 churches after the earthquake. Structures were subdivided into macro-elements and 16 collapse mechanisms were identified. A vulnerability analysis methodology based on a damage probability matrix was established. Binda and Saisi (2005) also noted the contribution made by these post earthquake examinations towards re-thinking masonry evaluation and strengthening methods.

An extensive survey of damage in Molise, Italy by Lagomarsino and Podesta (2004) identified the most frequent type of damage as being cracking and collapse of vaults, damage due to crushing and shearing of masonry pillars, sliding or overturning of spires over bell towers and out-of-plane failure of facade gables and apses. Another case study after this earthquake by Decanini (2004), reached similar conclusions. The construction criteria and site effects are stated as the most significant features contributing to the damage patterns observed.

The earthquake of 2008 in Wenchuan, China highlighted the seismic vulnerability of masonry structures to researchers. Many reports have mentioned on-site studies of the masonry structures. Lessons learnt from this strong earthquake disaster are discussed through investigations of typical structural damage. Seismic principles, key problems and design suggestions to improve the seismic capacity of masonry structures have been proposed by Wei and Ying (2008). Various seismic evaluation methods for masonry buildings with different criteria have been proposed based on on-site investigations (Ren, Lu et al. 2008, Su and Zhao 2010). Case studies following the Darfield earthquake of 2010, New Zealand mainly focussed on unreinforced masonry buildings. Anagnostopoulou et al. (2010) identified patterns of damage to churches of various architectural styles, structural systems and properties of the underlying soil. The report by Dizhur et al. (2011) also provides details on the characteristics of typical buildings, their damage and failure modes. Ismail (2011) focused on the performance of Christchurch and the retrofitting techniques employed.

The weakness in masonry structures due to structural modification and the use of non-compatible materials is repeatedly stressed through case studies (L. Ramos and Lourenco 2004, Anagnostopoulou, Bruneau et al. 2010). This illustrates the necessity for an understanding of the principles underlying the dynamic behaviour of masonry structures. In spite of the large variety of masonry structures around the world, damage mechanisms in

masonry structures have only been related to geometrical and connections criteria. Analysis of structural damage mechanisms is complex for most masonry structures and this situation provides the drive behind the work of this thesis. In particular, the achievements made by the above case studies have provided the background for the pseudo-static experiments based on limit state analysis which have been conducted by the author.

2.3 Review of the Experimental work on Masonry Walls

Carrying out a thorough case study is very time-consuming. Even then, case studies can only provide us with ultimate damage patterns to masonry structures. The complete damage and failure process can hardly be reconstructed. At present laboratory experiments are the most practical means of studying masonry structures. Experimental models are usually simplifications of real structural configurations and can be flexible as to the scales used. Long term environmental effects cannot be reproduced in the laboratory but tests can be performed to a convenient time schedule. Large numbers of tests can be performed to minimise error effects. Experimental work varying in objectives is described in the literature providing more understanding of the seismic response of masonry structures. The models have various structural configurations, scales and material properties.

Masonry walls are those elements of masonry structures which bear the horizontal forces caused by earthquakes and wind. Experimental studies on separate masonry walls show simpler and clearer damage patterns, which occur without the influences of other components. This can help to define the principal response of a complex masonry structure. Many experimental programme have been performed on this aspect, with both in-plane and out-of-plane wall behaviour explored and discussed.

2.3.1 Review of the in-plane experiments

The experiments of Magenes and Calvi (1998) on a full scale masonry prototype subject to cyclic shear is a pioneering experimental study on the in-plane seismic behaviour of masonry walls. This study shows strength and stiffness degradation behaviour as a crack increases. The in-plane damage patterns are defined as diagonal cracking at mortar joints for the lower values of axial load and aspect ratio, the cracking of bricks for higher values of axial load and aspect ratio and mixed joint and brick failure for intermediate combinations of these parameters. The response of masonry walls is seen to be strongly nonlinear because of the low tensile strength

of joints. Indeed, the shaking-table tests on the in-plane seismic response of masonry walls conducted by Wight and Kowalsky (2007) demonstrated reduced structural stiffness and increased wall displacement at reduced loading levels. They also defined sliding as a typical, but small component of overall in-plane wall displacement.

2.3.2 Review of the out-of-plane static experiments

The experimental work by Tomazevic and Lutman (1996) on out-of-plane behaviour is widely referred to by other researchers. Four damage indexes are distinguished, identified to be independent of the testing procedure but related to the loading conditions. A higher level of vertical load improves lateral resistance but reduces deformability and ductility. A more rigid initial behaviour under dynamic loading are also noted. The set of displacement-controlled tests on dry masonry couplets by Lourenco and Oliveira (2005) associates failure modes more clearly with vertical loads. Their work also showed that rotation and sliding occurs with low vertical load while rapid crack propagation occurs under high compressive stresses. The deformation is seen to be linear with high stiffness for a long period of time before continuous stiffness degradation sets in. They also illustrate the significant differences between the initial and the final Coulomb friction angles under moderate stress levels (Lourenco and Ramos 2004). Treating the masonry wall as a continuum, Tominaga and Nishimura (2008) confirm the out-of-plane bending characteristics of brick walls through bending tests on an English bond, 2-brick-thick, wall.

2.3.3 Review of the out-of-plane dynamic experiments

Out-of-plane shaking-table tests on unreinforced masonry walls conducted by Paquette and Bruneau (2001) simulated ground motion of progressively increased intensity. They demonstrated a significant capacity for masonry walls to resist out-of-plane inertial accelerations without failure. Similarly, the performance of walls was found to be related to the boundary conditions at roof level. Out-of-plane collapse of masonry walls, was demonstrated by Griffith and Lam (2004) to be determined by displacement. Static, free-vibration and dynamic tests with harmonic signals, impulse signals and earthquake signals were applied to unreinforced brick panels. In addition, the capacity to dissipate energy within masonry walls was noted by Ehsani and Saadatmanesh (1999) with out-of-plane cyclic loading, in spite of the generally considered brittle nature of brickwork. Recently, Derakhshan and Ingham (2010) stated that increasing wall slenderness ratios resulted in poorer out-of-plane post-cracking dynamic stability. They tested unreinforced masonry walls representing New Zealand buildings with

various ground motion scenarios. A total of 30 representative time-history records for walls with different slenderness ratios were analyzed.

2.4 Review of the Experimental work on 3D Masonry Models

Distinct from the experimental work on masonry walls, experiments on complete masonry models have enabled the study of the responses of different components of masonry structures and their interactions. Researchers have tested a variety of models with different scales and configurations in the laboratory.

2.4.1 Review of quasi-static experiments

Experimental study of the complete masonry model starts at the static loading stage. The possible structural response mechanisms are roughly defined as rocking, sliding and their combinations (Paquette, J., Bruneau et al. 2004). The model proved to be stable in spite of the inputs (Paquette, J., Bruneau et al. 2004, Yi, Moon et al. 2006). In quasi-static tests of a full-scale two-storey unreinforced masonry model by Yi and Moon (2006), whether the walls were damaged by local or global rocking is stated to depend on their opening ratios. The flange effect was found to significantly increase the out-of-plane load resistance. A large initial stiffness exists at the beginning of damage which decreased rapidly with lateral deformation. In a pseudo-dynamic study (Paquette, J., Bruneau et al. 2004), with a flexible wooden diaphragm and a gap on one corner, the full-scale unreinforced brick model, the flexible-floor/rigid-wall interactions were studied. The influence of discontinuous corners was found to be negligible during high intensity seismic excitation. The strength degradation was stated to have no significance even with large deformations.

More experimental work on 3D masonry models shows that structural failure occurs along regular patterns of lines which depend on the nature of the structural supports and height-to-width ratios (Hendry 1973, Anderson 1976, West, Hodgkinson et al. 1977, Tomazevic and Weiss 2010). Further experimental studies have clarified the relationships between geometrical characteristics of the structure and damage mechanisms. Structural performance can be understood provided the following factors are known (Binda, L., Saisi et al. 2000, Tomazevic and Weiss 2010): (i) its geometry; (ii) the characteristics of its bond type; (iii) the physical, chemical and mechanical characteristics of the components; (iv) the characteristics of masonry as a composite material. These conclusions have inspired

approximation methods based on fracture line theory (Sinha 1978).

2.4.2 Review of dynamic experiments

Some studies have highlighted the differences between dynamic and corresponding static experimental results (Adams 1996, Dolce, Mauro, Cardone et al. 2005). They indicate the difficulty in directly comparing these two series of results (Adams 1996) and illustrate that dynamic experiments predict a better seismic capacity of masonry models than do static tests (Dolce, Mauro, Cardone et al. 2005). Dynamic experimental research represents seismic behaviour more realistically. Shaking-table experiments have been widely carried out. Conclusions on the dynamic characteristics of the masonry structure, including its mechanical properties, dynamic behaviour and development of cracks have been accumulated.

Manos and Clough (1986) identified the contributions made by displacement and torsion on unreinforced masonry structural cracks. The importance of the minimum stagger length and shear capacity on seismic capacity is illustrated. Juhasova and Hurak (2002) recorded the development of cracks due to increasing intensity of loading. Dolce and Cardone (2005) provided a new index describing the potential for diaphragm damage caused by drift through his experimental studies on the shaking table. Through their 119 shaking-table tests on 24 ½-scale masonry models with base motions of similar peak acceleration and increased intensity, Benedetti and Carydis (1998) summarised how changes in structural dynamic properties correlated with increases in damage. The substantive homogenate property of the masonry construction was identified. A significant reduction in fundamental frequency with damage was illustrated. On this basis, Benedetti and Carydis (2001) also correlated the evolution of input energy with changes in damage patterns and compared the behaviour of buildings of different types. The behaviour of each building during an entire set of shocks was analyzed to assess the occurrence of damage in relation to the energy functions they were proposing.

Recently, Elvin and Uzoegbo (2011) recorded damage as bricks shifting, a few bricks splitting and cracking, and the skim plaster cracking and spalling by studying a 4m×4m mortar-less structure subject to earthquake loads. Magenes and Penna (2010) related the final failure to out-of-plane shaking through a model representative of a typical local stone building of two storeys with a pitched roof. From a one-half-scale model representative of houses in New Zealand under simulated earthquake ground excitation, Bothara and Dhakal (2010) stated that in plane damage in walls is mostly concentrated in zones of high shear stress notably in the

bottom storey. Out of plane wall damage is likely to occur mostly in zones of high response acceleration starting from the top storey. The nonlinear response directions were identified provided a good bond exists between brick layers. Some researchers (Hanazato, Minowa et al. 2008, Nakagawa, T. Narafu et al. 2011) specifically studied the collapse process and the movement of each structural component on a 3m×3m×3m brick masonry model simulating actual houses in the mountainous area of Pakistan. Sorrentino and Alshawa (2011) evaluated the earthquake energy damping effects of unreinforced masonry rocking mechanisms both experimentally and theoretically. The coefficient of restitution for one-sided and two-sided rocking and the effects were analyzed.

However, as dynamic studies still consist of theoretically oriented experimental work on simplified models, a gap exists between the behaviour of laboratory models and the response of real buildings due to artificial loading rates and component characterizations with scaled materials. For example, Juhasova and Hurak (2002) found that the model-shaking table interaction effect increases with increase of the mass and stiffness of the model from their shaking-table experiments on a 1/2-scale asymmetrical two-storey model. They concluded that boundary conditions representing soil–structure interactions should be included when testing large heavy models.

2.5 Review of Theoretical Masonry Building Models

2.5.1 Review of the static modelling based on limit analysis

To model the seismic behaviour of masonry structures, static-loading mathematical models have been developed since the 1960s based on lower bound and upper bound limit analysis methods. Livesley (Livesley 1978) adapted the technique for the analysis of rigid-plastic structural frames to provide a find the limit load of any structure formed from rigid blocks. Then this work was extended to the limit analysis of three-dimensional masonry structures (Livesley 1992). These equations only relate to the failure pattern and load-bearing capacity of the masonry wall at the time of failure and actual time-dependent characteristics cannot be modelled. In addition, since the ductility of masonry structures during shaking cannot be recognized by a static state analysis a conservative prediction of dynamic lateral capacity is given (Doherty, Grith et al. 2002). Additionally, since any cohesive forces bridging a crack surface gradually diminish as the crack gets wider, the strain-softening is also a feature not modelled by a static mechanical analysis.

2.5.2 Review of the dynamic simulation for masonry structures

Masonry, having a composite nature, is formed by discrete units (bricks or stones) and separated by mortared or dry joints. To model masonry structures theoretically, there are basically two fundamental approaches: the continuum and dis-continuum idealizations (Lourenço, P. B. 2002).

The continuum models represent the masonry structure with appropriate constitutive relations. As the preferred tools for engineering design, they are widely applied in practice using Finite Element (FE) methods. The discontinuous models represent the unit and joints separately. They are primarily used in research with increasing applications in practice. The discontinuous idealization can be accomplished with FE models containing joints or interface elements. It can also be represented by Discrete Element (DE) models where masonry is modelled as an assembly of component blocks or particles in mechanical interaction.

The FE model, due to the larger degrees of freedom in each element and the complex constitution to simulate the joints, requires much heavier computational work. In comparison, the DE method, starting from a discontinuous system, provides a more efficient procedure to study masonry structures, especially the historical masonry constructions which could be considered as made of dry stone blocks. The DE method was proposed by Cundall (1971). The solution procedure selected was the integration of the equations of motion of the blocks, which allowed the possibility of considering large displacements.

In the DE models, its simplest assumption is the block behaves like a rigid body. Interaction between blocks is represented by sets of point contacts or sets of edge-to-edge contacts, with no attempt to obtain a continuous stress distribution throughout the contact surface. The blocks then can be meshed independently with point contacts. Full separation is allowed between blocks and most of them permit the large displacement regime. Besides, DE models tend to employ time-stepping algorithms. All these features are present in the 2D program UDEC (Itasca, Minneapolis, MN, USA), which evolved from Cundall's original work (1971), and its 3D counterpart, the program 3DEC (Cundall 1988, Hart, Cundall et al. 1988).

Caliò et al. (2008) presented a 3D nonlinear discrete element approach for the evaluation of the seismic behaviour of masonry buildings. The well-known Rondelet out-of-plane mechanism are numerically simulated together with an example of the global behaviour of a typical masonry single nave church showing the capability of the proposed approach as an

advanced-but-simple tool for the estimation of the seismic vulnerability of masonry structures.

The distinction between finite and discrete elements codes has become somewhat blurred with their evolution. For example, blocks in DE models need no longer to be rigid, but may have internal FE meshes. Conversely, FE models are being used to represent discontinua at smaller scales. The incorporation of deformation kinematics into the discrete element formulation has also led naturally to a combined finite/discrete element approach in which the problem is analyzed by a combination of the two methods (Cundall and Hart 1989, Munjiza, Owen et al. 1995, Owen, Munjiza et al. 1995, Owen, Peric et al. 1998).

The FE and DE models, based on simulational software packages, can present the dynamic response of the complete masonry structure mechanically. Therefore, they are convenient to be applied in practical engineering works. However, usually sufficient material properties of the masonry and mortar are required to define the elements in order to derive the stress status and distribution in the structure. This largely increases the computational effort required to perform a simulation. In particular, for many historic buildings this kind of information is unavailable. On the other hand, the collapse and post-crack behaviour of the masonry structure relies mostly on mechanisms other than mechanical characteristics. Focusing on the theoretical damage mechanism of the masonry structure, the study presented here follows the assumption of rigid block masonry and simplifies the models by very limited numbers of blocks. This simpler mathematical model firstly requires much less computational work. The mathematical equations of the dynamic behaviour can be given to present clearer descriptions on the out-of-plane shaking with these mechanisms.

2.5.3 Review of the dynamic modelling based on rigid bodies

In recent years, following observations of the rocking and rotation of free standing tombstones during earthquakes in Japan, dynamic analysis has received an increasing amount of attention. As the bricks in a masonry structure have relatively low-stress levels and deformation capacities, a rigid block hypothesis is widely applied. Two elements need to be taken into account in the modelling of masonry structure. These are the masonry brick element as a rigid body and the mortar joint as an interface element. The masonry structure is treated in two different ways in mathematical models. It may be treated either as a homogeneous continuous model or as a system of several discrete blocks. The homogeneous models may offer good information on the global behaviour of a masonry structure before cracks are initiated, especially those structures with strong mortar cohesion. Trovalusci and Masiani (2005) derived

the macroscopic constitutive equations of a linear elastic equivalent multifield continuum based on a description of the materials at microscopic level. Their numerical examples showed the correspondence between discrete and continuum modelling, in both the linear and nonlinear contexts.

Due to the high complexity of masonry behaviour, numerical simulation approaches have also lead researchers to develop several constitutive models. The models are characterized by different levels of complexity (Lourenço, P. B. 2002) based on their objectives and their theoretical bases. Both linear analysis (Doherty, Grith et al. 2002, Trovalusci and Masiani 2005) and nonlinear analysis models (Berto, Saetta et al. 2004, Zucchini and Lourenco 2004) have been proposed. The determinant of the final collapse of masonry wall is either a displacement or a force criterion, with some studies stating displacement-based procedures gives better predictions, particularly for earthquake ground motions with high accelerations and low displacements (Doherty, Grith et al. 2002).

2.5.4 Review of the homogeneous models based on rigid-body dynamics

At present, most of these theoretical models emphasize on the mechanical properties and the masonry and joints variations in calculations of dynamic rocking, rotation and sliding (Cecchi and Sab 2009, Hammoud, Sab et al. 2011, Menon and Magenes 2011a, b). However, as mentioned above, models of mechanical properties are usually too specific for descriptions of the generalized characteristics of common masonry structures. In the study of response mechanisms some researchers have simulated the mortar in homogenous models. Zucchini and Lourenco (2004) addressed the formulation and implementation of a coupling between a micro-mechanical homogeneous model and an isotropic damage model. Their algorithm was applied to a nonlinear problem which simulated the behaviour up to complete failure caused by tensile loading parallel to the bed joint. They showed that neglecting the shear deformation of the unit leads to an overestimation of the masonry stiffness. However, in a parametric study by Berto and Saetta (2004), an isotropic microscopic model was used in simulating the behaviour of mortar and the orthotropic macroscopic model was used to reproduce the nonlinear behaviour of masonry. These studies proved once more that the mortar itself has little effect on the damage mechanisms of masonry walls (Cecchi and Sab 2002, Berto, Saetta et al. 2004).

Pietruszczak and Ushaksaraei (2003) described the progressive failure in structural masonry

using a continuum formulation. The conditions at failure were defined by a critical plane, the orientation of which was found by solving a constrained optimization problem. The response of the brickwork for different orientations of the bed joints relative to the loading direction was examined. The rigid-body numerical approach developed by Gilbert and Hobbs (2002) estimated the likely response of an unreinforced masonry wall subjected to out-of-plane impact loading. They identified the out-of-plane sliding mechanism as likely to be the most critical for a particular impact location with five possible mechanisms. Sensitivity studies indicated that wall thickness and the coefficient of base friction were particularly important parameters.

2.5.5 Review of the discrete models based on rigid-body dynamics

Through these studies, it has been concluded that accurate analysis of the nonlinear response of masonry is difficult to achieve using the homogenization technique (Berto, Saetta et al. 2004). Therefore, the necessity is stressed for discrete models to give a better description of the response mechanism of masonry structures under dynamic excitation. Mendola and Papia (1995) has proposed a block-interface method for calculating the out-of-plane response of unreinforced masonry walls. The approach focuses on tension cracking and large displacements, neglecting compression failures and assuming zero tension resistance for the material. Martini (1998) used the block-interface model and solid rectangular volume elements in representing two-way out-of-plane behaviour of unreinforced masonry walls. The nonlinear structural analysis method was applied to archaeological questions concerning the reconstruction of the ancient city of Pompeii and how it might be affected by a major earthquake.

Casolo and Neumair (2000) modelled the large walls of monuments with plane rigid elements to predict the out-of-plane damage behaviour caused by seismic loading. The elements are quadrilateral and connected to each other in the middle of their adjoining sides by hinges at which all the deformation takes place. The mechanical characteristics of the connections are defined to approximate the brittle behaviour of masonry. This model was then further improved by considering hysteretic behaviour and the degradation of stiffness and strength (Casolo 2000). The validity of this model was proved by investigating large walls in old masonry churches using geometric and material parameters based on damage data collected from the Friuli earthquake of 1976 (Casolo 1999). Results showed that the input acceleration may affect both the level of damage and the type of mechanism. But for the old non-engineered structures any correlation between damage level and peak ground acceleration is not necessarily strong, indicating the need to utilize more than one single earthquake-related parameter. Additionally, with comparable acceleration levels, for those earthquakes of longer significant

duration more complete pattern collapse mechanisms can form.

2.6 Summary

Seismic behaviour of masonry structures, although only first receiving attention in the 1960s, has become of much interest recently. Achievements have been made, in the areas of on-site investigations, experiments and theoretical modelling with various objectives in mind and in various contexts.

The on-site case study immediately following an earthquake is now commonplace and is increasingly intensive and elaborate. Useful information and analysis of the actual damage patterns which occur has led to assessment, repair and construction suggestions. The case study has provided the strongest catalyst for further studies on the dynamic behaviour of masonry structures.

Both static and dynamic experimental loading research studies vary in the scales and configurations of the models tested and the exciting procedures, as well as the study objectives due to the complexity of seismic behaviour of the masonry structure. Different dynamic response characteristics are being gradually clarified. Although some disagreements still exist, the principle that damage pattern is dependent on the type of input and relates only to the structural configuration has been identified. Structural damage mechanisms and their characteristics have been distinguished clearly for cases of static loading and used in practice. More experimental studies are described in this thesis, attempting to derive damage descriptions which are more complete, generic and systematic.

Dynamic loading experimental studies have received more attention recently, to obtain more understanding of practical dynamic collapse behaviour and its development in masonry structures. These have also provided much understanding of the development of stress, stiffness and displacement during the shaking of mechanical models. Most shaking-table studies in the literature have focussed on the mechanical status of the structure or the dynamic responses of models of buildings typical of some local area of the world. These are too specific to be applied to masonry structures in general. The descriptions of damage mechanisms and their characteristics under dynamic loading still have no systematic foundation. This situation justifies the aims of the experimental research on 3D masonry models described in this thesis.
Theoretical masonry research under conditions of static loading has become well developed

and been applied in cases of real building design. But for dynamic loading conditions, the mathematical modelling work based on the dynamics of rigid bodies is still far from representing reality because of the complexities of the mathematical dynamic equations describing the behaviour of multi rigid bodies and the difficulty in solving those equations under highly nonlinear conditions. Studies at present are mostly restricted to single rigid body systems which, however, avoid the difficulties associated with the multiple degrees of freedom inherent in the dynamic equation formulations. For this reason, possible movements of brickwork sections are usually studied separately. Theories of movement patterns and their transitions as loadings increase have been much discussed in the literature. At present more studies are needed to provide descriptions which are closer to observed reality, based on multiple-body models which allow for the interactions between different response mechanisms. It is hoped that study of the two rigid body model detailed below in this thesis will improve the description of the out-of-plane rocking of masonry façades.

Chapter 3 Pseudo-static Experiments on Seismic Behaviour of Masonry Walls

3.1 Introduction

Walls are the main components in masonry buildings carrying lateral loads produced by wind and earthquakes. Hence, most attention should be paid to walls when analysing the seismic behaviour of masonry structures. Walls in masonry structures may be damaged by earthquakes either as in-plane collapses or out-of-plane collapses, depending on the directions of the dominant forces they bear. In practice, generally both kinds of damages exist simultaneously in different places in a building. Static tests on dry masonry walls have been performed since the 1990s.

The pseudo-static experiments carried out here studied the out-of-plane and in-plane damage of dry masonry walls. As has already been stressed in the literature (Magenes, G. and Calvi 1997, Lourenço, P., Oliveira et al. 2005, Tomazevic and Weiss 2010), material properties have little influence on damage mechanisms. The post-crack behaviour remains consistent between dry brick walls and normally mortared walls. Therefore scaled dry masonry walls with different configurations were used. The damage mechanisms under the action of a steadily increasing horizontal force are classified. Clear damage characteristics, including damage mechanisms and collapse load factors, under increasing horizontal forces have been identified. The influences of the structural and geometrical parameters, such as geometric dimensions, connection conditions and bond types on damage mechanisms of the masonry wall, have been analysed. The validation of an existing seismic vulnerability assessment procedure FaMIVE for masonry buildings (D'Ayala, D. and Speranza 2003) has also been carried out. This series of pseudo-static experiments on scaled masonry walls provides a foundation for subsequent shaking-table experiments and further theoretical modelling work.

3.2 Theoretical Background

3.2.1 Theory of damage mechanism of masonry wall based on limit analysis

The series of tests on scaled masonry walls are based on previous theoretical work on limit analysis of damage mechanisms of masonry walls (D'Ayala, D. and Speranza 2003, D'Ayala, D. 2005). The mechanical model is based on the assumption that dry block masonry is essentially frictional in behaviour. If the structure has not been strengthened, it is assumed that the only means of restraint exerted between wall elements is governed by the friction between contact surfaces. The masonry walls are simulated with a system of rigid bodies, articulated by hinges. On this basis, scaled isolated masonry walls, walls with side walls and different degrees of connection at two corners were analysed.

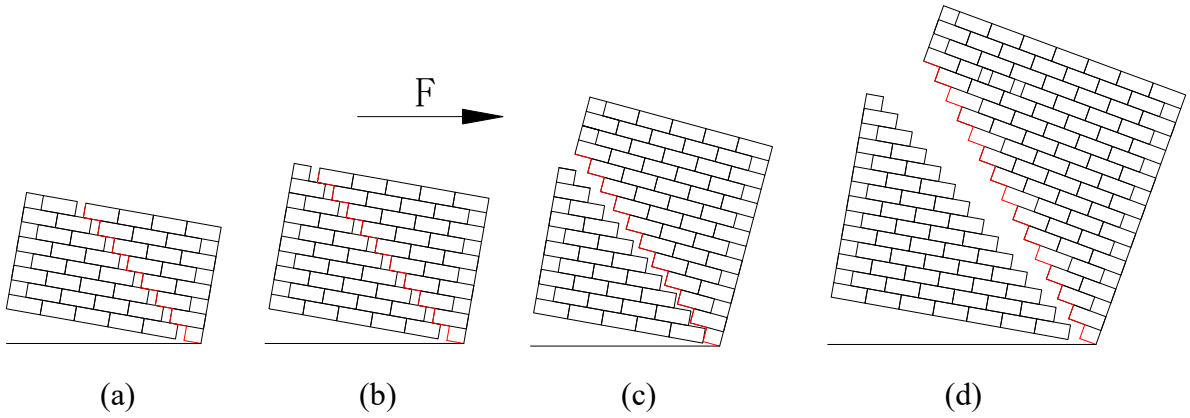

Figure 3.1 Observed In-plane damage mechanisms
((a) Sliding in triangular portion; (b) Sliding in diagonal plane;
(c) Overturning in trapezoidal portion; (d) Mixed mode in trapezoidal portion)

In-plane damage mechanisms, classified as sliding or overturning in Figure 3.1, are directly related to the geometry of the masonry wall itself (D'Ayala, D. and Speranza 2003). The out-of-plane damage mechanisms are more complicated. Classification of the out-of-plane damage mechanisms is presented in Figure 3.2 (D'Ayala, D. and Speranza 2003). The collapse load factor for each mechanism is based on a limit-state approach as the ratio between the lateral acceleration and the gravitational acceleration at incipient collapse, i.e. $\lambda = a / g$.

Parameters representing the geometric characteristics of bricks and walls are shown in Figure 3.3. The staggering length s is defined as the smallest length of overlapping between two

bricks pertaining to superposed courses.

When a horizontal force is applied in the in-plane direction to a masonry wall, a diagonal crack will separate the wall into two portions. As shown in Figure 3.1, if the left-hand part does not participate in the failure, the right-hand part may be triangular, trapezoidal or rectangular, depending on the angle formed by the crack with the vertical edge. In the treatment of this problem, it is assumed that only one crack will form in the wall, which will start from the lower corner, about which overturning is expected to take place. It can be seen from the experimental results that this is true at incipient collapse, and this is typically followed by a series of parallel cracks forming in the brickwork as the mechanism develops.

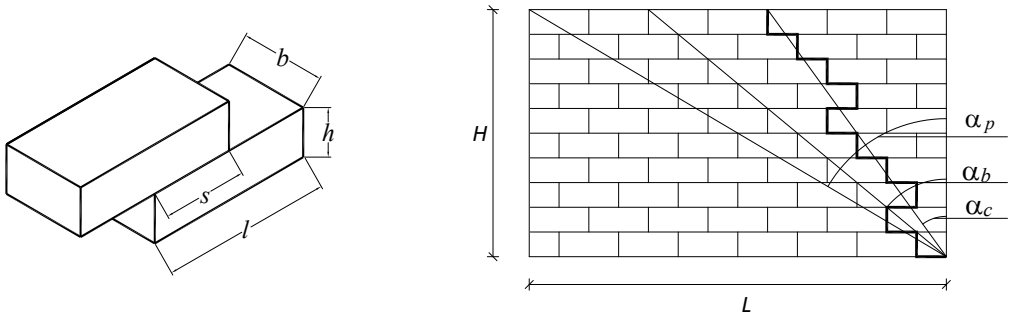

(a) (b)

Figure 3.2. Model configurations (D'Ayala, D. and Speranza 2003)

((a) Brick and stagger dimensions; (b) Angles defining the unit and wall shape ratios and the variable angle of crack.)

The in-plane damage mechanism is influenced by the wall dimensions, the stagger ratios and the type of bond in the wall. Whether sliding or overturning takes place is a function of the friction coefficient μ, the shape of the brick, the stagger ratio *s/h* and the shape ratio *L/H*. The horizontal static action is defined as proportion of the body mass, by means of a load factor λ, corresponding to the ratio *a/g* between the lateral acceleration and the gravitational acceleration.

If the total shear strength developed on the crack from friction is defined as $C_{\cot}(\alpha_c)$, the load factor λ_s that governs the sliding mechanism can be derived as:

$$\lambda_s = \frac{C_{\cot}(\alpha_c)}{M(\alpha_c)} = \frac{\mu}{\tan\alpha_c} \cdot \frac{s}{h} \tag{3-1}$$

where $M(\alpha_c)$ is the mass of the mobilised portion at incipient failure (D'Ayala, D. and Speranza 2003).

Considering the overturning mechanism, the collapse load factor λ_o is obtained as

$$\lambda_o(\alpha_c \le \min(\alpha_p, \alpha_b)) = \frac{\tan^2 \alpha_c + \mu \frac{s}{h}}{2 \tan \alpha_c} \tag{3-2a}$$

$$\lambda_o(\alpha_p > \alpha_c > \alpha_b) = \frac{\tan \alpha_c}{2} \tag{3-2b}$$

$$\lambda_o(\alpha_b > \alpha_c > \alpha_p) = \frac{\tan^2 \alpha_c (3 \tan \alpha_c - 2 \tan \alpha_p + 2\mu) - \mu \tan \alpha_p \left(2 \tan \alpha_c - \frac{s}{h} \right)}{(3 \tan^2 \alpha_c - \tan^2 \alpha_p)} \cdot \frac{\tan \alpha_p}{\tan \alpha_c} \tag{3-2c}$$

$$\lambda_o(\alpha_c > \max(\alpha_b, \alpha_p)) = \frac{\tan \alpha_c \tan \alpha_p (3 \tan \alpha_c - 2 \tan \alpha_p)}{(3 \tan^2 \alpha_c - \tan^2 \alpha_p)} \tag{3-2d}$$

Due to staggering of the blocks, overturning can only take place if sufficient sliding also takes place, so that a free horizontal surface equivalent to the length of the wall can be identified.

For sliding, the lower limit of the load factor corresponds to the friction coefficient μ, occurring at a crack angle α_c. For overturning, a free continuous surface separating the rotating portion from the fixed portion occurs when $\tan \alpha_c = s/h$. In this case, collapse occurs without involving friction and the minimum load factor is $\lambda = s/2h$, if *s/h<L/H*. Otherwise it is a function of *L/H*. The load factor for the limit state configuration of the masonry wall to avoid collapse is therefore the one for which

$$\lambda_c(\alpha_c) = \min(\lambda_o, \lambda_s) \tag{3-3}$$

The out-of-plane wall response possesses a wider range of possible damage mechanisms because of the greater number of façade structural configurations. According to the theoretical study (D'Ayala, D. and Speranza 2003), the out-of-plane load factor for a masonry wall is a function of its shape parameter *L/H* and the restraining action due to friction and the corner connections with the side walls. Superimposed vertical loads and specifically the loadings on orthogonal walls, also have an influence. The usual damage mechanisms are shown in Figure 3.3.

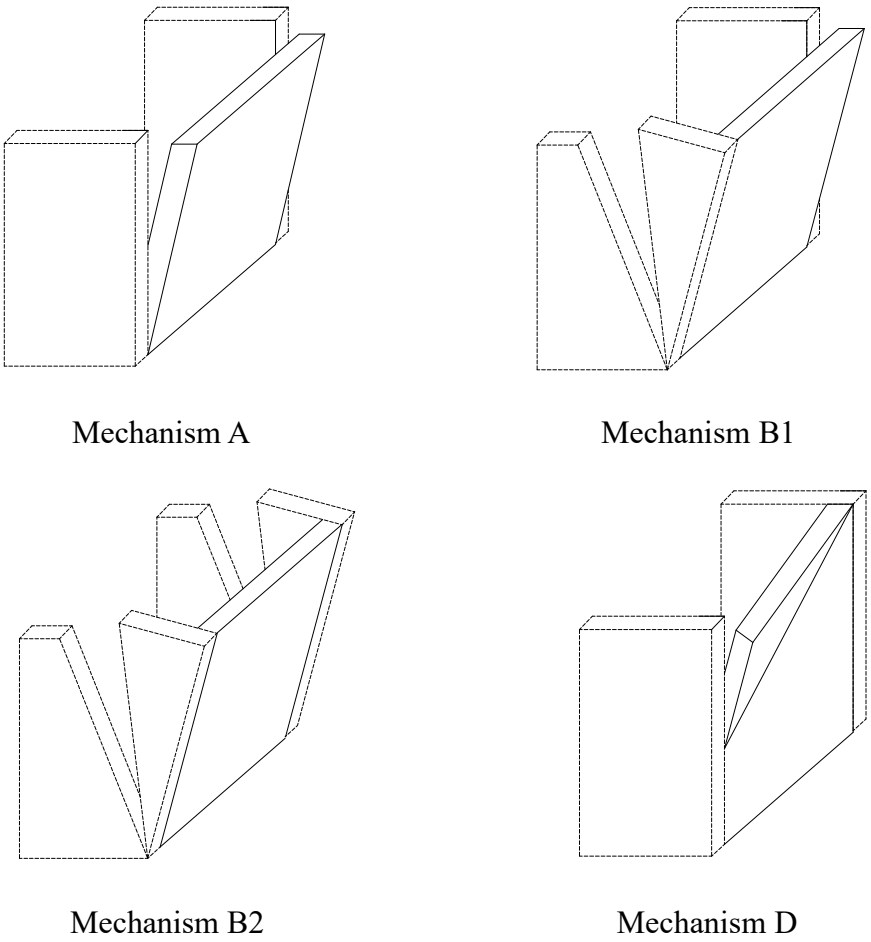

Figure 3.3 Out-of-plane damage mechanisms

3.2.2 The FaMIVE programme based on theoretical studies (D'Ayala, D. and Speranza 2003)

Theoretical load factors and damage mechanisms for the tested walls are calculated using the FaMIVE procedure (D'Ayala, D. and Speranza 2003). This Excel program is designed to predict the damage mechanism and load bearing capacity of a masonry wall according to its structural and geometrical parameters. It originates from a previous theoretical study on the in-plane and out-of-plane collapse mechanism of the masonry wall, based on the theory of limit analysis (D'Ayala, D. and Speranza 2003).

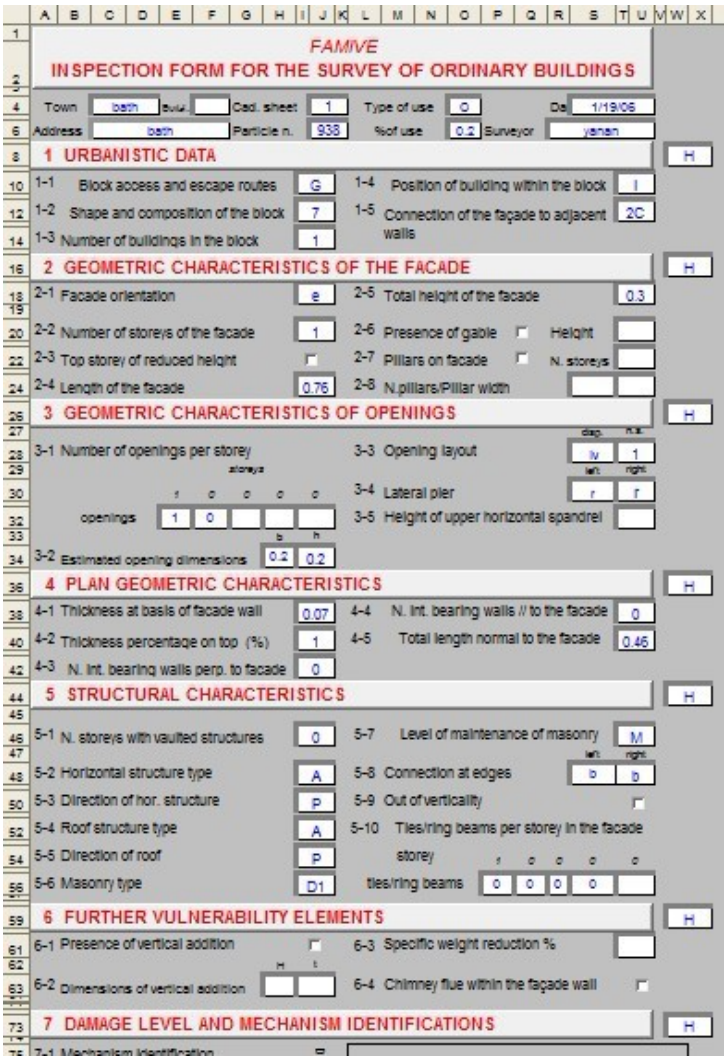

FAMIVE

INSPECTION FORM FOR THE SURVEY OF ORDINARY BUILDINGS

Town: bath | Cad. sheet: 1 | Type of use: O | Da: 1/19/06

Address: bath | Particle n.: 938 | %of use: 0.2 | Surveyor: yanan

1 URBANISTIC DATA — H

1-1 Block access and escape routes: G
1-2 Shape and composition of the block: 7
1-3 Number of buildings in the block: 1
1-4 Position of building within the block: I
1-5 Connection of the façade to adjacent walls: 2C

2 GEOMETRIC CHARACTERISTICS OF THE FACADE — H

2-1 Facade orientation: e
2-2 Number of storeys of the facade: 1
2-3 Top storey of reduced height:
2-4 Length of the facade: 0.76
2-5 Total height of the facade: 0.3
2-6 Presence of gable: Height:
2-7 Pillars on facade: N. storeys:
2-8 N.pillars/Pillar width:

3 GEOMETRIC CHARACTERISTICS OF OPENINGS — H

3-1 Number of openings per storey (storeys: 1 0 0 0 0; openings: 1 0)
3-2 Estimated opening dimensions: b 0.2, h 0.2
3-3 Opening layout: disp. IV, n.s. 1
3-4 Lateral pier: left r, right r
3-5 Height of upper horizontal spandrel:

4 PLAN GEOMETRIC CHARACTERISTICS — H

4-1 Thickness at basis of facade wall: 0.07
4-2 Thickness percentage on top (%): 1
4-3 N. Int. bearing walls perp. to facade: 0
4-4 N. Int. bearing walls // to the facade: 0
4-5 Total length normal to the facade: 0.46

5 STRUCTURAL CHARACTERISTICS — H

5-1 N. storeys with vaulted structures: 0
5-2 Horizontal structure type: A
5-3 Direction of hor. structure: P
5-4 Roof structure type: A
5-5 Direction of roof: P
5-6 Masonry type: D1
5-7 Level of maintenance of masonry: M
5-8 Connection at edges: left b, right b
5-9 Out of verticality:
5-10 Ties/ring beams per storey in the facade (storey: 1 0 0 0 0; ties/ring beams: 0 0 0 0)

6 FURTHER VULNERABILITY ELEMENTS — H

6-1 Presence of vertical addition:
6-2 Dimensions of vertical addition: H, L
6-3 Specific weight reduction %:
6-4 Chimney flue within the façade wall:

7 DAMAGE LEVEL AND MECHANISM IDENTIFICATIONS — H

7-1 Mechanism identification:

(a)

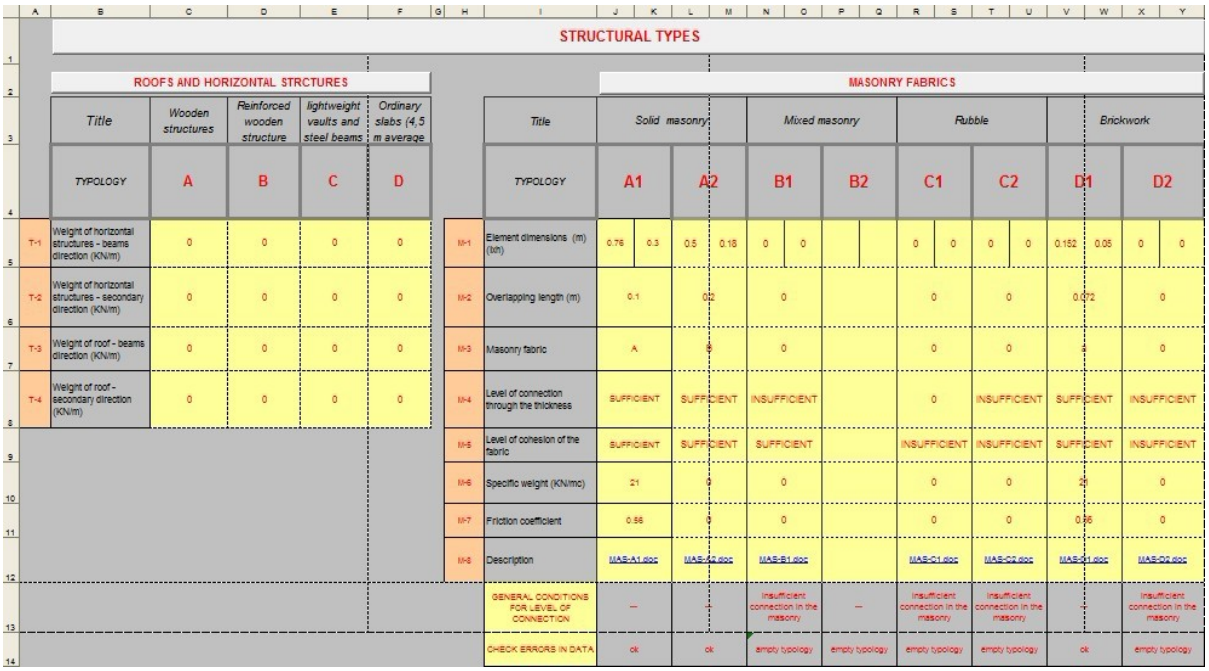

STRUCTURAL TYPES

ROOFS AND HORIZONTAL STRCTURES

	Title	Wooden structures	Reinforced wooden structure	lightweight vaults and steel beams	Ordinary slabs (4,5 m average
	TYPOLOGY	A	B	C	D
T-1	Weight of horizontal structures - beams direction (KN/m)	0	0	0	0
T-2	Weight of horizontal structures - secondary direction (KN/m)	0	0	0	0
T-3	Weight of roof - beams direction (KN/m)	0	0	0	0
T-4	Weight of roof - secondary direction (KN/m)	0	0	0	0

MASONRY FABRICS

	Title	Solid masonry		Mixed masonry		Rubble		Brickwork	
	TYPOLOGY	A1	A2	B1	B2	C1	C2	D1	D2
M-1	Element dimensions (m) (bh)	0.76 0.3	0.5 0.18	0 0		0 0	0 0	0.152 0.05	0 0
M-2	Overlapping length (m)	0.1	0.2	0		0	0	0.072	0
M-3	Masonry fabric	A	B	0		0	0	C	0
M-4	Level of connection through the thickness	SUFFICIENT	SUFFICIENT	INSUFFICIENT		0	INSUFFICIENT	SUFFICIENT	INSUFFICIENT
M-5	Level of cohesion of the fabric	SUFFICIENT	SUFFICIENT	SUFFICIENT		INSUFFICIENT	INSUFFICIENT	SUFFICIENT	INSUFFICIENT
M-6	Specific weight (KN/mc)	21	0	0		0	0	20	0
M-7	Friction coefficient	0.56	0	0		0	0	0.56	0
M-8	Description	MAS-A1.doc	MAS-A2.doc	MAS-B1.doc		MAS-C1.doc	MAS-C2.doc	MAS-D1.doc	MAS-D2.doc
	GENERAL CONDITIONS FOR LEVEL OF CONNECTION	—	—	Insufficient connection in the masonry	—	Insufficient connection in the masonry	Insufficient connection in the masonry	—	Insufficient connection in the masonry
	CHECK ERRORS IN DATA	ok	ok	empty typology	empty typology	empty typology	empty typology	ok	empty typology

(b)

A	B1	B2	C	D	E	F	G/Gs	H	M	I	L	LOAD FACTOR
0.22	---	---	0.76	---	---	---	---	0.56	---	---	---	0.22
0.22	---	---	0.76	---	---	---	---	0.56	---	---	---	0.22
0.22	---	---	0.76	---	---	---	---	0.56	---	---	---	0.22
0.22	---	---	0.76	---	---	---	#VALUE!	0.56	---	---	---	#VALUE!
0.15	---	---	0.75	---	---	---	#VALUE!	0.56	---	---	---	#VALUE!
0.15	---	---	0.75	---	---	---	#VALUE!	0.56	---	---	---	#VALUE!
0.18	---	---	0.75	---	---	---	#VALUE!	0.56	---	---	---	#VALUE!

(c)

Figure 3.4 The FaMIVE program being validated

((a) the input parameters; (b) the top loading conditions and the masonry fabric;

(c) the load factors obtained for each mechanism)

Figure 3.4(a-c) shows the interfaces of the program. Firstly the basic information of the masonry wall being analysed needs to be input in Figure 3.4(a), such as geometric characteristics for the façade, structure and openings. The weight of the roof and other horizontal structure is required in Figure 3.4(b) to obtain the top loading conditions. The characteristics of the masonry fabric are also input in this sheet, including the type of masonry, the friction coefficient and the stagger length, which are required in the load factor calculations. The load factors for each possible damage mechanism according to the input information based on the previous theory (D'Ayala, D. and Speranza 2003) are then presented in the sheet shown in Figure 3.4(c). The mechanism that contains the lowest load factor is defined as the vulnerable damage mechanism for the masonry wall being studied. The load bearing capacity before collapse of the masonry wall under a one-way horizontal force is then identified.

For in-plane collapse, with regard to the mass of the collapsed part identified by the crack angle, the sliding load factor is independent of L/H and only relates to s/h and the friction coefficient μ of the brick. In the case of overturning, based on the assumption that friction does not impede overturning motion because there is a clean separation of the surfaces along the crack line, a theoretical minimum load factor can be established. On the other hand, if the crack line is identified by optimisation, a corresponding maximum theoretical load factor can be obtained by assuming that the friction on that surface is fully active. In most cases where mixed mode failures occur, these two values provide upper and lower bounds to the real collapse load factor, in comparison to the discrete element analysis approach.

3.3 Experimental Programme

This experimental programme aims to study the one-way collapse mechanism of the masonry walls under horizontal forces. Gradually increasing horizontal forces were applied separately in the in-plane and out-of-plane directions on the masonry specimens. Scaled dry masonry walls with different structural and geometric configurations were tested. The damage mechanisms were classified and their characteristics were analysed. This is also the basis of the dynamic experiments on the 3D model on the shaking table.

3.3.1 Specimen fabrication

Tests were conducted with the two sets of bricks shown in Figure 3.5. The first set used 3/4-scale the standard bricks, with dimensions of 152mm×75mm×50mm ($L \times W \times H$). The second used 1/2-scale bricks (105mm×50mm×35mm). The smaller bricks are new and less dusty. The smaller dimensions also make it easier to simulate walls containing large numbers of bricks and show crack patterns more clearly. They are also used in the shaking-table experiments below. Walls in the tests were constructed without mortar so that the specimens could be reconstructed quickly, using the same bricks, thereby reducing preparation time between tests.

Figure 3.5 Bricks used in the walls

The friction coefficients of the two types of bricks were measured using a shear box. One brick was fixed at the bottom, with the upper part being placed on its top. The upper part can be pulled to slide on top of the bottom brick, with the force being measurable. The friction force F between the two parts of bricks was defined when sliding at a constant speed. Based on the Coulomb friction equation $\mu = F / N$, the friction coefficient can be obtained. The tests that have been carried out on these two kinds of bricks are listed in Table 3.1 and Table 3.2. The loads on the upper part N were varied in repeat tests to obtain an averaged value. The average value of the friction coefficient measured was 0.56 for the large brick and 0.81 for the small

one, as shown in Figure 3.6 and Figure 3.7.

Table 3.1 Measured data from tests on large bricks

Test No.	Mass(*g*)	Load(*N*)	Weight (*N*)	Force(*N*)
1	891	4.8	8.731	5.633
2	1768	8.7	17.326	9.533
3	1761	8.5	17.258	9.333
4	1778	8.9	17.424	9.733
5	1259	5.7	12.338	6.533
6	1273	5.5	12.475	6.333
7	2648	13.7	25.950	14.533
8	2655	15.0	26.019	15.833
9	1610	8.4	15.778	9.233
10	1704	8.9	16.699	9.733
11	3062	14.5	30.008	15.333
12	3029	15.5	29.684	16.333

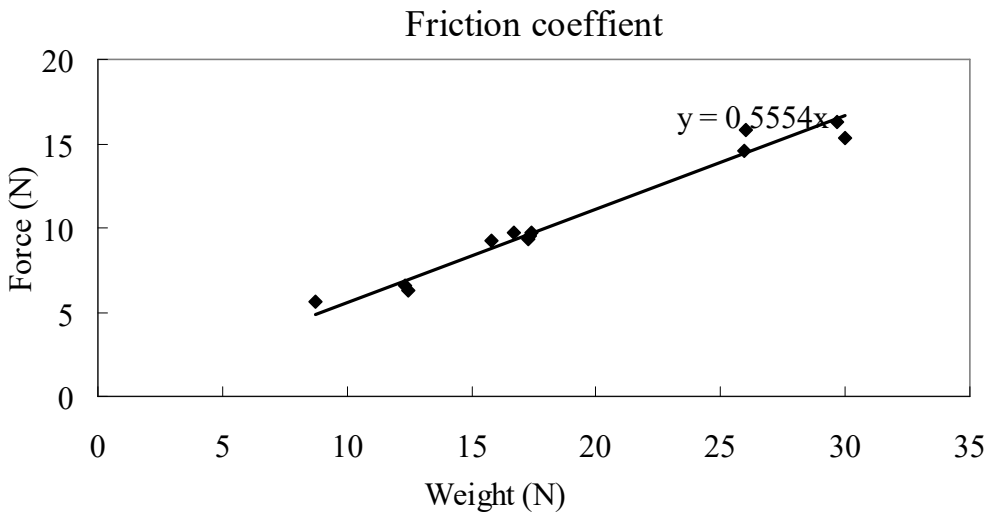

Figure 3.6 The distribution of measured friction coefficient and averaged value for large brick

Table 3.2 Measured data from tests on small bricks

Test No.	Mass(g)	Load(N)	Weight (N)	Force(N)
1	336	2.0	3.293	2.813
2	647	4.5	6.340	5.313
3	979	7.0	9.594	7.813
4	537	3.0	5.263	3.813
5	720	4.5	7.056	5.313
6	759	5.5	7.438	6.313
7	832	6.0	8.154	6.813

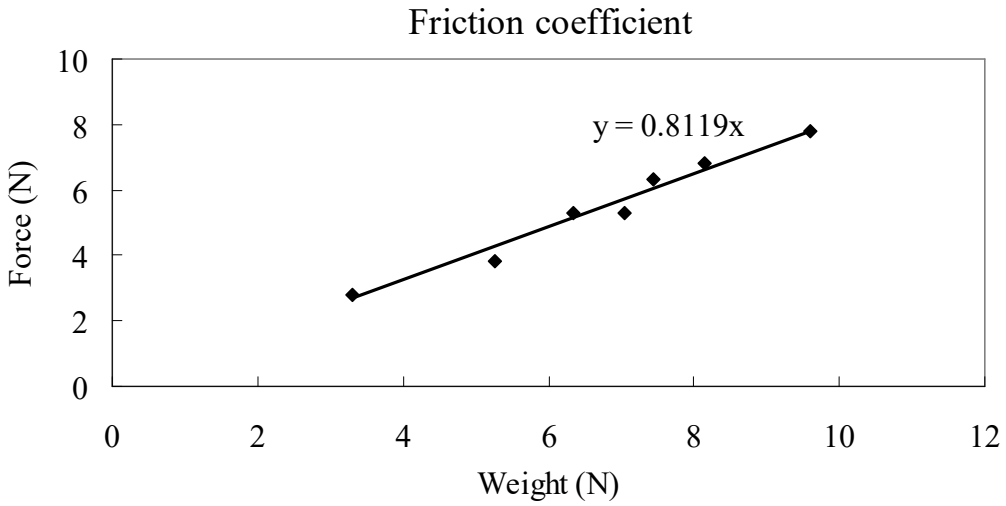

Figure 3.7 The distribution of measured friction coefficient and averaged value for small brick

3.3.2 Experimental setup

A timber table that could be tilted gradually from one edge by an electrically controlled crane was set up. Dry masonry walls with various structural configurations were placed on this table and tilted until final collapse occurred. The table, as shown in Figure 3.8(a), is constrained by two steel hinges. The stiffness of the table is sufficient to maintain the weight of the wall with negligible out-of-plane deformation. As the lateral distributed force due to tilting of the masonry walls is a gravity-induced force, and is only balanced by the friction developed between layers, the corresponding collapse load factor will be equal to the tangent of the tilting angle of the table. The angle of tilt was measured by a digital inclinometer.


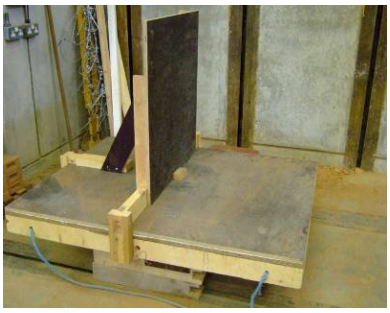

(a) (b)

Figure 3.8 Experimental tests set up

((a) the tilting table; (b) the vertical board on the table)

In the in-plane tests, a vertical board parallel to the wall was set up, as shown in Figure 3.8(b), designed to remain vertical and stable during construction and testing. This enables specimens to be constructed with larger slenderness ratios. Comparisons between test results from shorter walls with and without the vertical board while tilting indicate that the influence of friction between the board and the wall can be ignored.

3.3.3 Test procedure

The in-plane tests were basically classified into two groups, as shown in Figure 3.6. The large bricks were laid in two different ways to obtain different slenderness *h/t* values of 50/75 and 75/50. Two kinds of bond types, that is, stretcher bond and English bond, were considered. Figure 3.9 shows walls with the same dimensions in three different layouts.


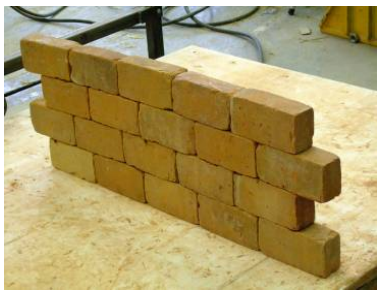


Stretcher bond (*t/h*=75/50) Stretcher bond (*t/h*=50/75) English bond

Figure 3.9 Walls constructed in different ways

For large bricks with *h/t*=50/75, both the stagger ratio *s/h* and the shape ratio *L/H* varied over a large number of tests. For *L*=3 and 5, the shape ratio *L/H* ranged from 0.5 to 3, with stagger ratios *s/h* at 1.5 and 1 respectively. In the case of *h/t*=75/50, the shape ratios were set at 2.63 and 1.75, with *L*=5 and stagger ratios equal to 0.8 and 1. For the small bricks, only stretcher

bond with *t/h*=50/35 was used. The stagger *s* was chosen as 10mm, 50mm and 75mm, yielding *s/h* values of 0.28, 1 and 1.5 respectively. The number of brick lengths varied from 3 to 5, 7 to 9 in this case to obtain situations where *L/H*<1 and *L/H*>1.

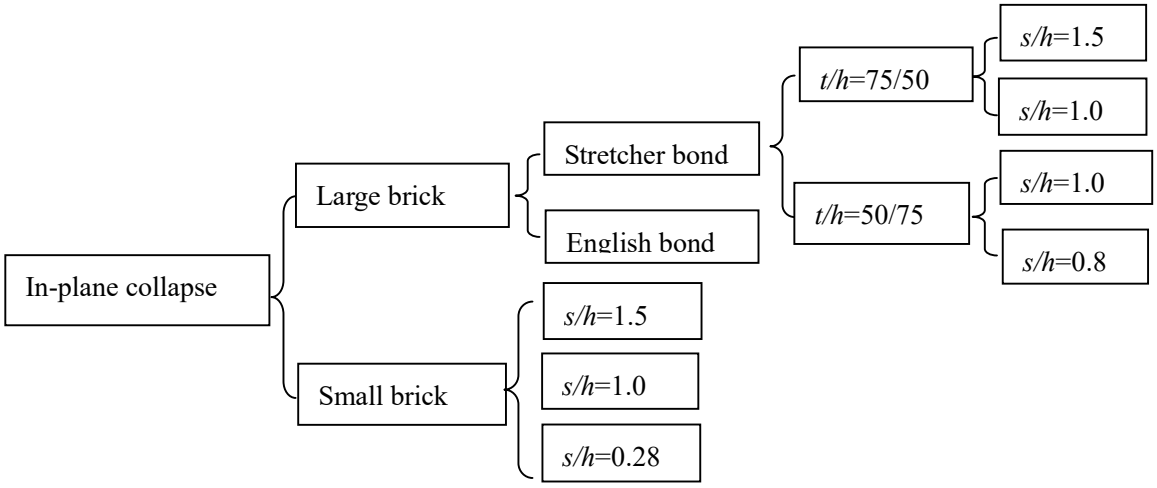

Figure 3.10 Classification of in-plane tests

For the walls constructed with the large bricks, while maintaining *L*=5, the number of courses varied from 6, 9 to 11. Two kinds of side wall, respectively with 3-brick lengths and 6-brick lengths, were used for each façade. When using small bricks, walls were constructed with 15, 21 and 27 courses. The dimensions of the side walls were the same as those of the corresponding façade walls. This set of small-brick walls contained a larger number of bricks in the models so that damage behaviour, especially the arching effect and the crack locations, could be studied more clearly.

In terms of the out-of-plane tests, different kinds of corner connections were used in the tests to explore the effects of corner combinations on the resulting damage mechanisms. The poor, good and strong connections for the walls using large bricks are respectively defined as those with staggers of 10mm, 50mm and 75mm and stagger ratios of 0.2, 1.0 and 1.5. For walls using small bricks, the corresponding staggers were 10mm, 35mm and 50mm, with ratios of 0.3, 1 and 1.5. Walls were first constructed with strong connections in both corners. In addition, with one corner maintained as a poor connection, façade walls were respectively built with a poor connection, a good connection and a strong connection in the other corner.

Taking into account variations in the size of the bricks and the dry configuration used, the timber table was tilted slowly and carefully to maintain a steady collapse of the specimens. For each test, if, for example an individual bricks fell out, the test was repeated until a steady

collapse was observed.

3.3.4 Test results

Damage of masonry walls is expressed in terms of load bearing capacity, collapse mechanism and crack pattern in the test results. During testing, the tilting procedure was recorded by a camera. The collapse pattern was photographed for future classification and analysis. The tilting was stopped as soon as collapse was initiated. The tilting angle whose tangent value was defined as the load factor in each test was measured by a digital inclinometer.

The tests were performed and analysed in several groups, in each of which one structural configuration was kept, to permit comparison. Focus was placed on the *L/H* ratio for the in-plane collapse and on the corner connection for the out-of-plane collapse when discussing the damage mechanisms and the corresponding load factor.

The test results were also used to verify the program FaMIVE for seismic vulnerability of masonry structures. The theoretical results for the same masonry specimens being tested were obtained. Both the in-plane and out-of-plane load factor and damage mechanism are compared between the experimental and theoretical studies.

3.4 Analysis of In-plane Tilting Tests (Shi and D'Ayala 2006)

3.4.1 Analysis of the test results

If an in-plane horizontal force is present, masonry walls will either slide or overturn, usually along a diagonal crack line whose inclination depends on the geometrical configurations of the walls.

Figure 3.11 demonstrates the relationship between the load factor and different geometrical and structural parameters. Figure 3.11(a) and (b) both illustrate the size effect of the masonry wall irrespective of the size of the bricks. At the same *L/H* ratio, a constant crack line is observed from the bottom of the inclined side. On this basis, the load factor decreases when either the size of the wall or the number of bricks in the wall increases. This supports the size effect being defined theoretically by comparing the nominal strength of geometrically similar structures of different size. Comparison between Figure 3.11(a) and (c) shows that when the walls have the same dimension the load factor increases with the increase of the stagger ratio.

This is because better connection conditions, associated with the increased stagger, offer larger frictional resistance. Figure 3.11(d) shows that with the same number of bricks and the same wall shapes, the use of small bricks leads to higher load factors than the large bricks. As the two types of bricks are of the same shape but have different friction coefficients, the higher load factors given by the small bricks (which have a higher friction coefficient) indicate that friction does have an effect on joints along the crack line when collapse occurs. The extent of the influence may vary for different damage mechanisms and crack angles. Therefore, the load factor in practical dry wall cases should be larger than the load factors suggested in the theoretical work (D'Ayala, D. and Speranza 2003), which assumes that friction is not present at crack surfaces.

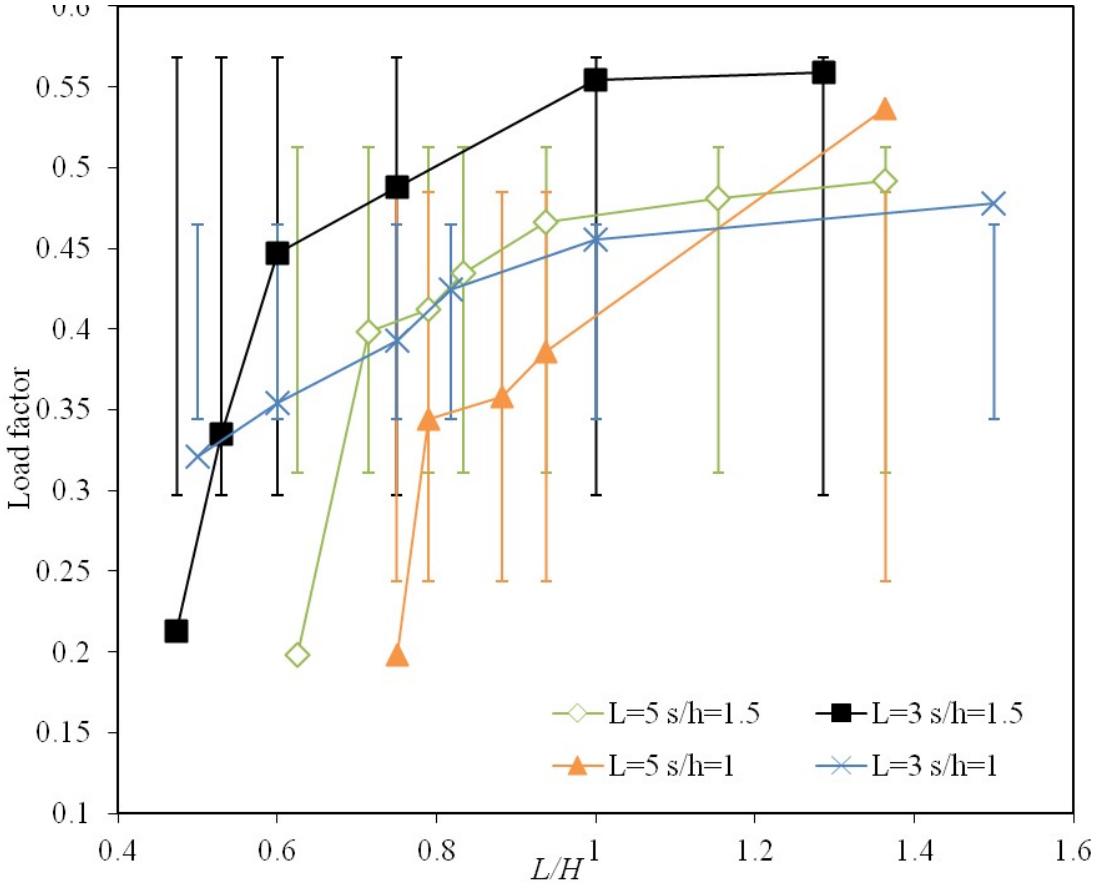

(a)

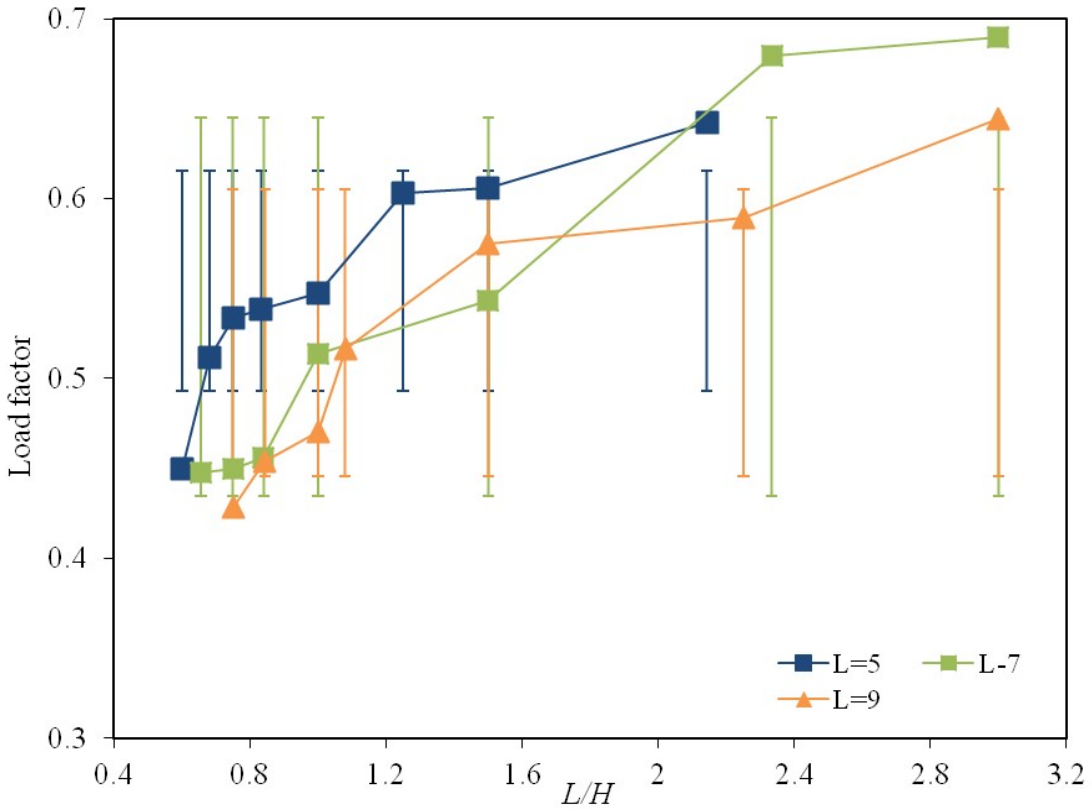
0.7
0.6
0.5
0.4
0.3
Load factor
0.4
0.8
1.2
1.6
2
2.4
2.8
3.2
L/H
L=5
L-7
L=9

(b)

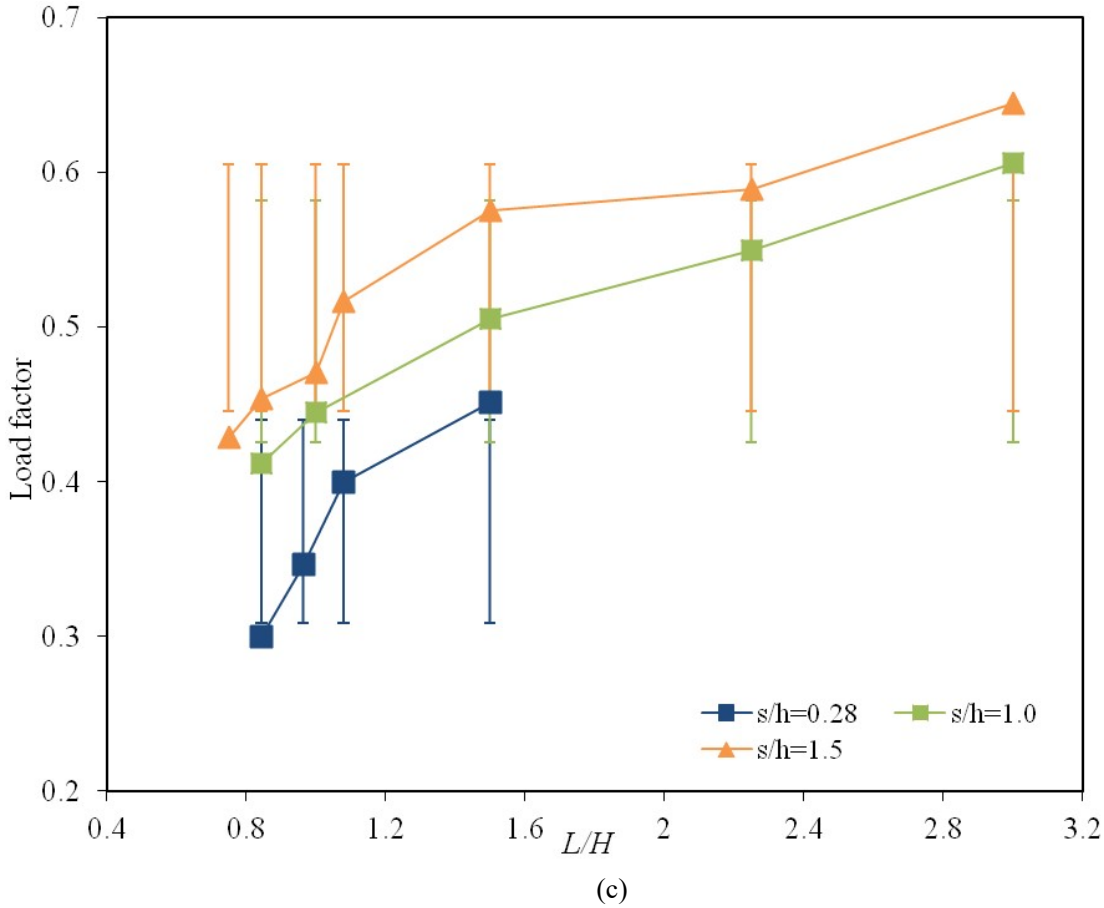
0.7
0.6
0.5
0.4
0.3
0.2
Load factor
0.4
0.8
1.2
1.6
2
2.4
2.8
3.2
L/H
s/h=0.28
s/h=1.0
s/h=1.5

(c)

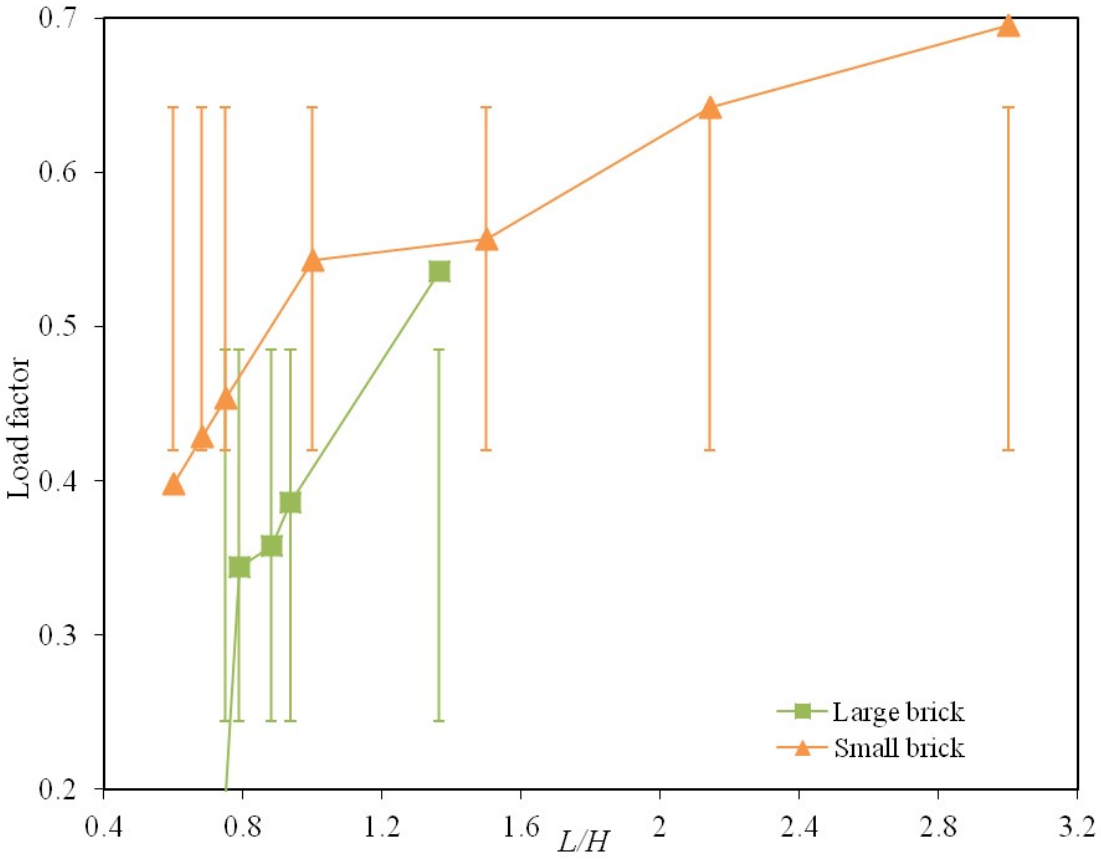

(d)

Figure 3.11 Correlation of in-plane load factor with geometric characteristics with error bars ((a) Large brick; (b) Small brick, *s/h*=1.5; (c) Small brick, *L*=9; (d) *L*=5, *s/h*=1)

Figure 3.11 shows the influence of *L/H* on the in-plane load factor for a masonry wall. All curves remain approximately parallel to one another, which illustrates that the slope decreases substantially above a certain value of *L/H*. When only considering the walls with large bricks, the change in slope occurs at *L/H*=0.6 for the wall with *L*=3. When *L*=5, *s/h*=1.5, this change occurs at *L/H*=0.75 irrespective of the brick size. Similar changes occur for all curves simultaneously at *L/H*=1, with different *s/h* values in Figure 3.11(c). This confirms the assumption that the shape of the curve is particularly influenced by the geometry of the brick wall models. As the shapes of both small and large bricks are identical, as length: width: height=6: 3: 2, the slopes of the curves relating load factors with *L/H* are affected only by the geometric shapes of the models tested.

The brick layout in the wall also influences the magnitude of the in-plane load factor. The highest load factor is obtained for walls in stretcher bond with *h/t*=50/75. It decreases slightly when walls are built with English bond and decreases following a large slope at *h/t* =75/50 for

large bricks. For example, for L/H=2.5 with t/h=75/50, the load factor is 0.48 for stretcher bond, 0.45 for English bond and only 0.36 when t/h=50/75, although the friction coefficient and the shape ratio of the walls remained unchanged.

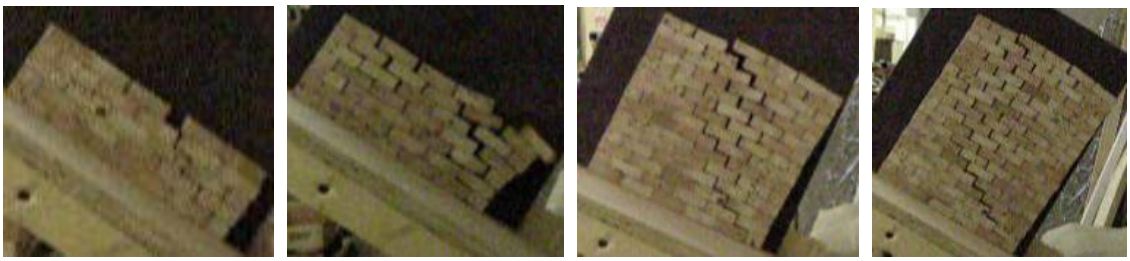

(a) (b) (c) (d)

Figure 3.12 In-plane damage in walls with different numbers of courses (L=5)
((a) H=5; (b) H=6; (c) H=15; (d) H=20)

(a) (b) (c)

Figure 3.13 In-plane damage in walls of different lengths (H=25)
((a) L=5; (b) L=7; (c) L=9)

Figure 3.12 and Figure 3.13 show the development of different in-plane wall collapse patterns with regard to variation in wall length and height. Usually the main diagonal crack line develops before collapse, from the first brick at the bottom of the leeward side along a staggered stepping line. The angle of inclination of this crack remains unchanged from the bottom to the top of the wall irrespective of its height and length. Therefore, for walls with the same number of bricks in the wall length, the larger the number of courses in the height of the wall, the larger the collapsed proportion involved. Conversely, for the same number of courses in the height of the wall but with different wall lengths, the collapsed area of longer walls is a smaller proportion of the whole wall.

For walls with L=5, 7 and 9 in Figure 3.13, the variations in the damage mechanism develop step by step in the same manner as L/H varies between 3, 2.14, 1, 0.75 and 0.6. Therefore, unlike the load factor case, which relates to the scale of the wall and the number of bricks both

in length and height, the damage mechanism case depends only on *L*/*H* and remains unaffected by variations in the number of bricks for a given *L/H*.

It is observed in tests that mixed damage mechanisms are more common for the in-plane collapses. For example in Figure 3.12, walls collapse as pure sliding only in Figure 3.12(a) when *L/H*=3. For *L/H*=2.14 in Figure 3.12(b), while sliding is still the principal damage mechanism, the first column of the wall on the leeward side has begun to overturn before sliding. With continuous decrease in *L/H*, overturning becomes more and more apparent at the first column of the bricks. For $L/H \leq 1$ in Figure 3.12(c), more obvious overturning develops for the first two columns, but is still accompanied by sliding. For values smaller than *L/H*=0.75 in Figure 3.12(d), the dominant in-plane damage mechanism changes to overturning. The portion that remains intact and overturns ahead of damage along the main crack line enlarges to the first three columns on the leeward side. From *L/H*=0.6, as shown in Figure 3.12(a), pure overturning begins to occur rather than mixed damage. The whole portion above the main crack line remains intact and overturns. In summary, with decreasing *L/H*, the damage mechanism changes gradually from sliding to overturning, with ever larger portions of the wall bonding together and overturning before the final sliding damage occurs along the main crack line. The integrity of the intact portion above the main crack line also increases with decrease in the ratio *L/H*.

3.4.2 Validation of FaMIVE for in-plane vulnerability assessment

To validate the procedure, the theoretical collapse load factors of selected walls based on earlier theoretical studies were calculated and compared with the corresponding tests results. These four walls have *s/h*=1.5, *L*=5, and *L/H* values of 3, 2.14, 1 and 0.75. In the theoretical model, the bricks are laid with half-length staggers and *s*/*h* varies with the shape of brick. However, in tests, the coefficient *s* was changed by altering the overlap lengths. This difference between the theoretical model and the practical tests means that only those test results with *s*/*h*=1.5 are directly comparable with the load factors calculated by the program.

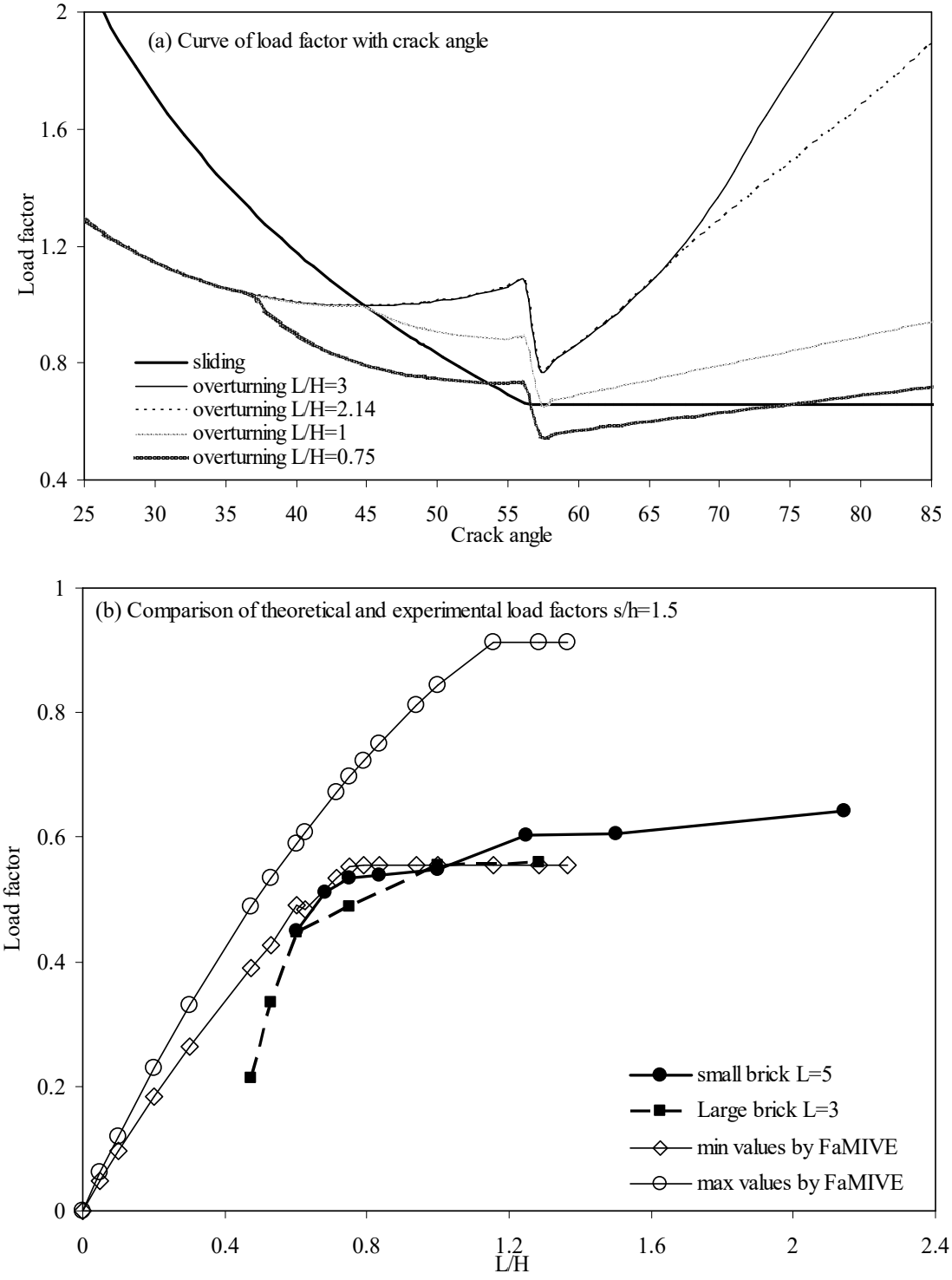

Figure 3.13 Validation of the in-plane theoretical procedure (FaMIVE)

The curves in Figure 3.13(a) show the variation in load factor in relation to possible crack angle inclinations for the wall tested experimentally. The crack angle is that between the main crack line and the bottom line of the masonry wall. As the sliding load factor in theory does not change with *L*/*H*, a single line is drawn for walls of all *L*/*H* ratios. The load factor decreases monotonically with increase of crack angle, which indicates increasing vulnerability with crack

angle but with a smaller damaged portion. The overturning load factor curves show a marked variation in slope and in minimum value for walls with different *L/H*. The curves no longer decrease monotonically but show a sudden variation around 56°. Marked differences in slope and in minimum values are shown for different *L/H* values. The ultimate theoretical load factor for each wall, therefore, is the corresponding minimum value of either the sliding or the overturning curve, whichever is the smaller. Based on these curves, the theoretical damage mechanism as well as the crack angle value can be derived.

Figure 3.13(a) shows that the minimum value of the theoretical sliding load factor coincides with a friction coefficient of 0.66 corresponding to a minimum crack angle of 56.1^{o}. The minimum overturning load factors for all walls with $L/H > 1$, $L/H = 1$ and $L/H < 1$ occur at the same crack angle of 56.3^{o}, which is a little larger than the sliding angle. This small difference in angle values relates to the resolution used in the calculations. In terms of the values of load factor, walls with $L/H=3$ and $L/H=2.14$ representing $L/H>1$ have the same minimum overturning load factor as 0.78. As the corresponding sliding load factor shown is 0.67, theoretically, sliding will occur with a crack angle of 56.1^{o} for these two walls. For wall $L/H=1$, the minimum overturning load factor is 0.65, only slightly smaller than the sliding load factor 0.67. In this case, mixed behaviour is most likely, consistent with the experimental observations related above. Finally, for the wall with $L/H=0.75$, the minimum load factor 0.56 is associated with overturning. Compared with the sliding load factor 0.67, overturning will occur along the crack angle as 56.3^{o}. This theoretical damage mechanism is also consistent with the experimental damage reported above. Therefore, the theory provides good consistent predictions of the experimental results in terms of damage mechanism and angle of cracks. Meanwhile, associated with the same collapse angle, the load factor consistently reduces when the geometric ratio of the façade decreases from $L/H>1$ to $L/H<1$.

Figure 3.13(b) compares the theoretical load factors with the corresponding experimental results. The results for walls of the same bond types and lengths but different types of bricks and numbers of courses are listed. Good agreement can be seen between the theoretical and experimental results when $L/H>0.8$. For walls using large bricks with smaller ratios of *L/H*, although the curves do not differ substantially, the theoretical values seem to overestimate the experimental values. This might be due to the poorer in-plane stability of slender walls. The surfaces of bricks are not perfectly flat and the modest wall curvature both in and out-of-plane reduces structural stability, especially of the slender walls. This feature not only reduces the contact surface between bricks but, over many courses, results in misalignments overall. These manufacturing defects, inherent in the bricks, in the case of the more slender walls, result in a

combined in-plane and out-of-plane failure, for smaller angles of tilt. Although this could be alleviated using better manufactured bricks, real walls would, in practice, suffer the same defect. Other forms of inherent error leading to inaccurate collapse load factors in experiments may relate to the sensitivity of the testing apparatus, especially the speed of tilt, consistency in the point of identification of the collapse and the corresponding precision in the measurement of the angle of tilt. This could be a subject for further investigation. Alternative procedures used so far, however, have not provided significantly different results.

3.5 Analysis on Out-of-plane Tilting Tests (Shi, D'Ayala et al. 2008)

The out-of-plane collapse of masonry walls is much more complicated than in-plane collapse and is known to be the most common type of damage after an earthquake. Parameters analysed in this series of tests are the corner connection condition, the bond type and the façade and side wall dimensions.

3.5.1 Analysis of the test results

Out-of-plane tilting tests were first used to study the influence of corner connection. The variations in incipient damage patterns due to different corner structural configurations are shown in Figure 3.14. With a poor connection in one corner being ensured, walls collapse as mechanisms A, B1 and D when the other corner possesses poor, good and strong connections respectively. When both corners have a strong connection, damage mechanism B2 or G applies, being the most commonly occurring in practice. The case with strong connections at both corners will also be studied in the following experimental study in the dynamic phase.

For the façade walls without proper constraint at both corners, as in Figure 3.14(a), the façade is more like an isolated wall without wings. Mechanism A occurs. In this situation, rocking is observed over a larger portion, while the collapse occurs in a smaller upper part. The collapsing masonry is bonded by a horizontal line, followed by a separate in-plane collapse of the side walls. The collapsed portion contains only a slight bulge acting more like one rigid body. This supports the proposed two-rigid-body mathematical model discussed in Chapter 5. In comparison, when both corners of the façade have strong connections, as shown in Figure 3.14(d), Mechanism B2 can be identified as the collapse mechanism. The rocking also exists in a larger portion and collapse occurs in the upper part. Overturning is from the first column of the side walls along a diagonal line to the edges, and contains the whole of the first several layers and then the middle of the following layers within two stepped crack lines in the façade

wall, with an arched shape. The longer the façade wall, the clearer is this arching behaviour. Mechanism B2 will develop into Mechanism G when the façade wall is too wide for the overturning arch of the façade wall to influence the side walls. The dynamic damage process of the arch effect, as in Mechanism B2 or Mechanism G, is further explored by the shaking-table experiments of Chapter 4. The rocking behaviour in Mechanism A, B2 and G are all observed to contain two parts, with rocking of a larger portion and a separate collapse in the upper part within it. This is also used in the theoretical model in Chapter 5.

(a) Mechanism A (b) Mechanism D (c) Mechanism B1 (d) Mechanism B2 & G

Figure 3.14 Experimental out-of-plane damage mechanisms
((a) Mechanism A: collapse on the façade without corner bricks along a horizontal line; (b) Mechanism D: collapse on the façade without corner bricks in a triangle portion from one edge to another; (c) Mechanism B1: collapse on the façade without corner bricks of the inner corner with bad connection but with corner bricks of the outer corner with strong connections; (d) Mechanism B2: collapse on the façade with bricks from both corners with strong connection; Mechanism G: Mechanism B2 with a dominant arch in the middle façade)

When unsymmetrical corner connections are applied, the side with the better connection tends to collapse with only a small part of the side wall, while the other poorly connected side behaves as Mechanism A. The lack of good corner constraint causes an adjacent façade collapse larger than that near the better connected side. Correspondingly, a stepped oblique crack line develops across the façade wall. In addition, the better-connected corner causes the badly connected side to resemble a roller type of collapse, with more layers than that of Mechanism B2. When one corner has a strong connection and the other a poor one, the collapse at the strong side is that of Mechanism B2, with a complete diagonal crack line to the other side. This is defined as Mechanism D, as shown in Figure 3.14(b). In contrast, when one corner has a good connection and the other remains as a poor connection, a larger part of the side wall participates in the façade collapse and the diagonal crack line changes to a horizontal line at the centre of the façade wall, and a smaller portion of the wall collapses. This behaviour is defined as Mechanism B, as shown in Figure 3.14(c).

The variations in out-of-plane load factors and damage mechanisms verified by the tests confirm that the corner connection is the most critical factor influencing the out-of-plane behaviour of the masonry wall. Structural shape and stagger ratio variations have little influence. It is the better connection which provides a stronger constraint, resulting in a smaller collapsed portion. For example, in Figure 3.14, Mechanism A occurred with 11 collapsed courses, but Mechanism B2 applied to façade walls of the same dimensions with only three collapsed courses. Compared with Mechanism B1, Mechanism D occurs with fewer collapsed courses at both better constrained and badly connected corners.

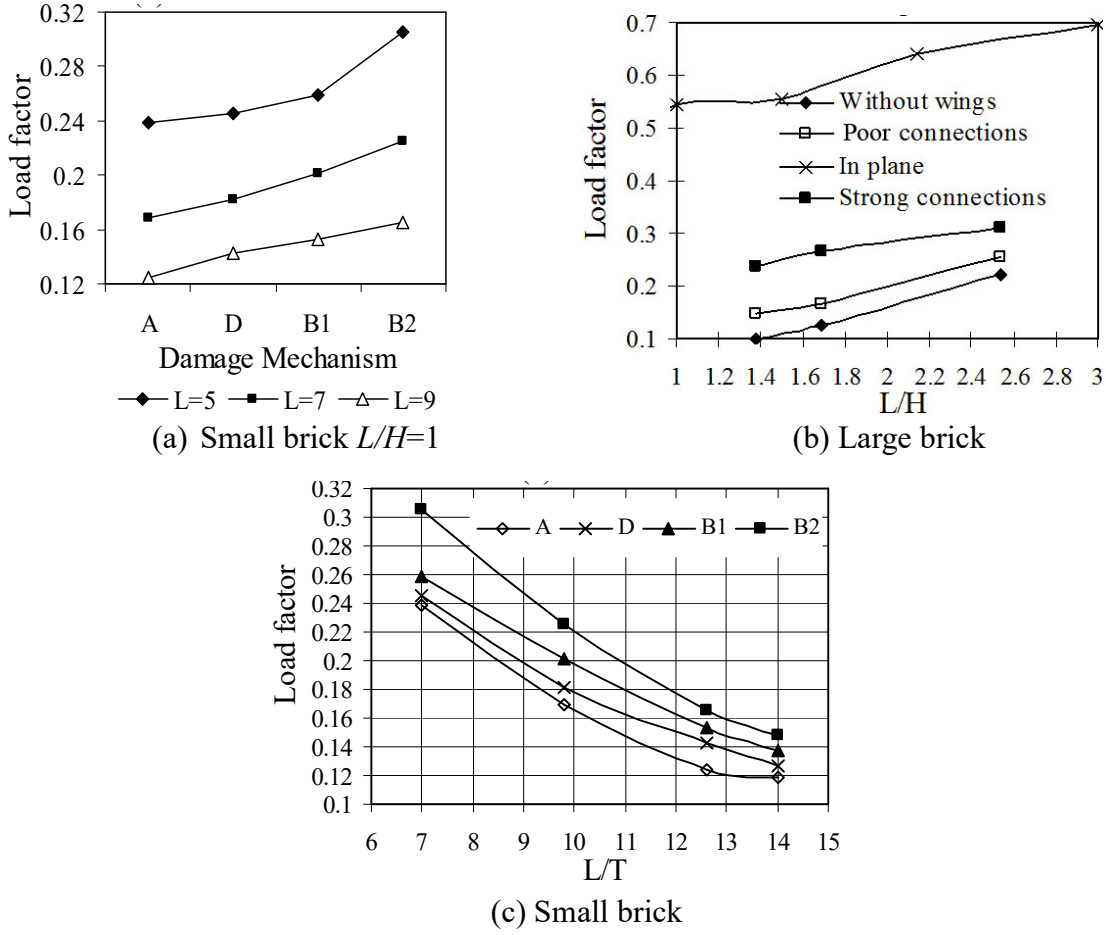

(a) Small brick *L*/*H*=1

(b) Large brick

(c) Small brick

Figure 3.15 Changes of out-of-plane load factor with geometric characteristics

In Figure 3.15(a), the magnitude of the out-of-plane load factor is seen to vary consistently with the corresponding damage mechanisms for walls with the same *L*/*H* ratio. This indicates that the corner connection is no doubt the most crucial factor dictating out-of-plane seismic behaviour. Additionally, the parallel curves in Figure 3.14(a) show constant increase of the load factor with improvement of corner connection. Better connections at corners provide larger load bearing capacities. As a better connection means more friction and better corner

constraint, this constant slope should relate to the friction coefficient of the bricks used. The only exception is the smaller load factor for Mechanism B1 compared to that for Mechanism D even with one stronger corner connection. This inconsistency demonstrates the extra high seismic vulnerability of the masonry façade with connections at the two corners which are largely unsymmetrical. In addition, the effect of the length of the masonry wall is illustrated again by the out-of-plane load factors in Figure 3.15(a). Given a constant L/H ratio, the masonry façade possesses a lower collapse load factor, when this contains greater numbers of bricks to form a larger size. Thus, larger numbers of bricks in a masonry wall lead to a lower out-of-plane seismic resistance capability.

The out-of-plane load factor is also influenced by the slenderness of the wall. Figure 3.15(b) shows that, irrespective of the structural characteristics of the façade, the load factor consistently increases with increase of L/H. This coincides with results from the in-plane tests. The effect of side walls on the out-of-plane load factor is also presented in Figure 3.15(b). Isolated walls without side walls have the smallest out-of-plane load factors and usually collapse from the bottom layer. As long as side walls exist, even with poor connections, load factors increase significantly. However, it is also observed that the lengths of side walls have little effect on the load factor. Except for a few bricks close to the corners, most parts of the side walls, in fact, remain uninfluenced by the out-of-plane collapse. In addition, Figure 3.15(b) shows that the out-of-plane load factor, even for walls with the strongest corner connections at both edges, is much smaller than the corresponding in-plane load factor. This is consistent with, and supported by, the fact that out-of-plane collapse is more likely to occur in masonry structures subjected to horizontal forces.

In terms of the damage mechanism, curves demonstrating the changes in load factors with the scales of the walls remain parallel in Figure 3.15(c). The value of L/H for walls with 5, 9 and 7 bricks in each layer is 1 and changes to 1.4 when L=10 bricks. Accordingly, the slopes change to a smaller value at this point, which indicates that they relate to wall shape. As the damage mechanism is determined by the corner connections, the observation made above, that it is the corner connection conditions that determine the out-of-plane load factor, is reconfirmed.

3.5.2 Validation of FaMIVE for out-of-plane vulnerability assessment

In the program FaMIVE, developed for vulnerability analysis (D'Ayala, D. and Speranza 2003, D'Ayala, D. 2005), the out-of-plane damage mechanisms and the corresponding load factors for masonry walls can be estimated by inputting relevant structural information. The program

calculates the load factors applying to all defined out-of-plane damage mechanisms. The ultimate load factor is chosen as the minimum value calculated and the corresponding mechanism is predicted as the actual final damage mechanism.

The results of this series of out-of-plane tests were used to validate this theoretical procedure. Comparisons between theoretical and experimental load factors can be seen in Figure 3.16 for certain walls with large bricks and in Figure 3.17 for walls with both kinds of bricks.

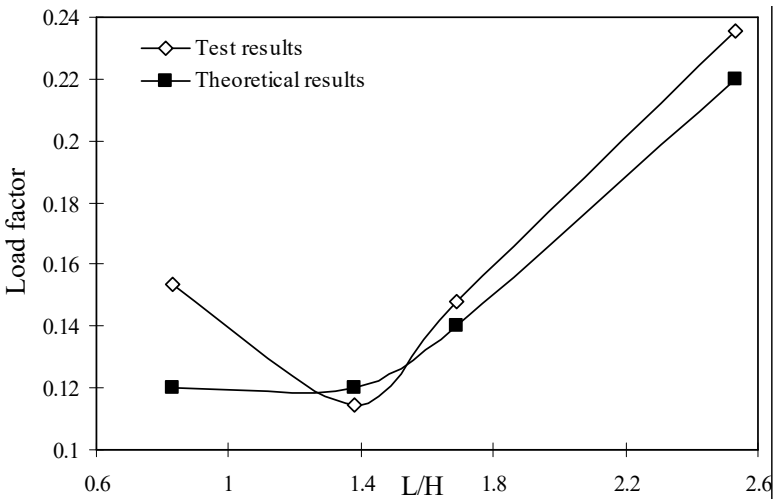

Figure 3.16 Experimental validations of walls without wings (large bricks)

The theoretical load factors obtained using this procedure and the corresponding experimental values for walls without the support of wings are both shown in Figure 3.16. All walls without wings are predicted to fail as Mechanism A under the theoretical procedure. A larger relative experimental load factor error occurs for the wall with L/H=0.8 because its larger slenderness ratio reduces stability in practice. In the other cases, the differences between experimental and theoretical results remain consistently small, irrespective of the ratio L/H. This proves the consistency and accuracy of the test programme. For walls with wings, because FaMIVE only defines corner connections as “poor” or “good”, differences between good and strong connections in tests cannot be predicted. Both wall designs would theoretical give Mechanism D results. Because in reality, actual damage differences between Mechanism B1 and Mechanism D do occur, FaMIVE is shown to be too limited in the range of parameters it covers and needs further investigation and development.

Considering the theoretical and experimental data as shown in Figure 3.17, for walls using both large bricks and small bricks, it is clear that all of the data are distributed reasonably evenly on the two sides of the line $y=x$, demonstrating correlation between the experimental

and theoretical results. However, in most cases, the out-of-plane theoretical results give larger load factors than the corresponding experimental ones, which highlight the variability inherent in experimental results (and probably in real-life construction), have not been allowed for in the theoretical predictions. On the other hand, smaller theoretical values were found in the case of in-plane damage. The larger out-of-plane theoretical results probably originate from the greater difficulty in defining the beginning of the out-of-plane collapse because of the arching effect.

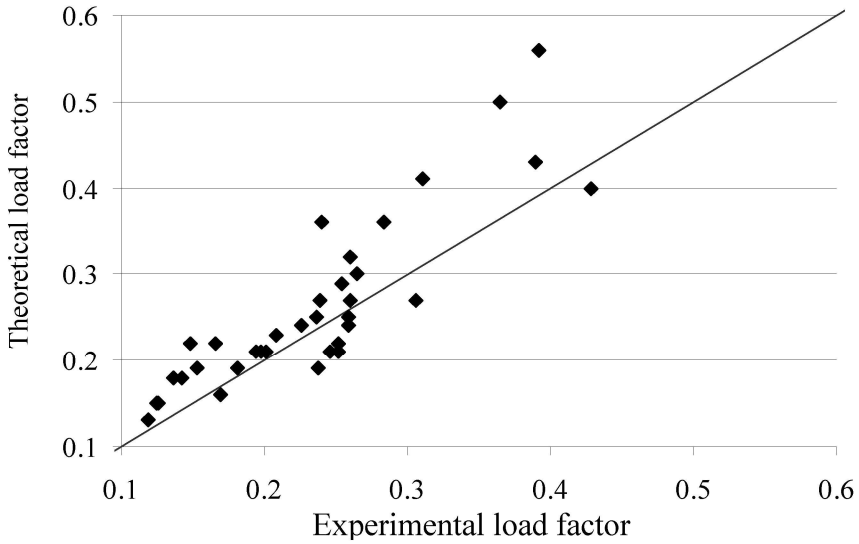

Figure 3.17 Comparison between experimental and theoretical (FaMIVE) load factors

Apart from the theoretical simplifications, errors may also arise from experimental procedure, for example the speed of tilt, the consistency in identifying the point of collapse condition and therefore the timing of the measurement of the tilting angle. However, it can be assumed that the procedure successfully predicts the potential out-of-plane damage mechanisms in masonry walls. Additionally, except for those walls damaged as Mechanism B2, the largest relative error between theoretical and experimental load factors is below 30%. The out-of-plane seismic vulnerability assessment using this procedure can still be considered to be reliable within its limitations. Equally important, the experimental procedures, which are wider in scope and therefore add new knowledge, can also be said to have been provisionally validated.

3.5.3 Conclusions

From the analysis of the results of this set of systematic pseudo-static experiments, conclusions can be summarised as:

1. The load factor for a masonry wall relates to its geometric form, its scale, the number of bricks it contains, the stagger ratio, the bond type and the shape of brick being used.
2. With regard to the in-plane damage mechanism, the main crack line leading to collapse remains constant in direction, usually as a diagonal stepped line developing from the first brick at the bottom on the leeward side. The crack angle coincides with the angle of stagger. The failure mode changes from sliding to overturning gradually with decrease of *L/H*. In most cases, the wall collapses with a mixed mechanism.
3. With more complicated corner connections and structural configurations, masonry walls present more types of out-of-plane damage mechanisms. The out-of-plane damage mechanism of a masonry wall is only affected by the corner connections. Mechanism A, B1, D and B2 succeed each other gradually as the two corner connections become ever stronger. For walls with strong connections at both corners, Mechanism G becomes increasingly dominant as the length of the façade wall increases. In addition, it should be noted that, better corner connections also offer better constraints and therefore smaller collapsed portions.
4. For the facades with symmetric corner connections, a consistent rocking characteristic can be presented. Rocking occurs in a larger portion of the wall, with a smaller upper part collapsing eventually. This forms the experimental basis of the theoretical model described in Chapter 5.
5. Out-of-plane collapse load factor is influenced by several structural parameters, such as strength of corner connection, bond type and dimensions. The corner connection is the most crucial factor affecting the magnitude of the out-of-plane load factor. Normally, better connections offer better load bearing capacities. An exception to this occurred for Mechanism D, which demonstrates the extremely high seismic vulnerability for masonry walls when corner connections are particularly unsymmetrical.
6. Size effects in masonry walls can be demonstrated in both in-plane and out-of-plane collapse tests. Larger number of bricks in masonry wall leads to lower out-of-plane seismic bearing capability. This is also influenced by the slenderness of the wall.
7. The load factor is a function of the friction coefficient of the bricks. The same load factors for various parameters are obtained for walls with the same material.
8. Comparison between experimental and theoretical results broadly indicates the validity of both the in-plane and out-of-plane seismic vulnerability assessment procedures developed previously.

This series of pseudo-static experiments on scaled masonry walls provides a foundation for the shaking-table studies of Chapter 4 and the theoretical modelling work of Chapter 5. As the out-of-plane collapse case has been identified to be more vulnerable, it will be studied further

in the dynamic experiments of Chapter 4. In practice, a separate freestanding wall rarely exists. And in a real structure, an in-plane collapse and an out-of-plane façade collapse will generally influence each other. Therefore, how the different in-plane motion of the 3D models is influenced by the dominant out-of-plane rocking will also be discussed. The consistence and differences between the two kinds of out-of-plane rocking respectively with one-direction pseudo-static loads and with reciprocating dynamic loads will be provided. Meanwhile, the behaviour in Mechanism A, B2 and G provides experimental justification for the two-rigid-body mathematical system of Chapter 5.

Chapter 4 Shaking-table Experiments on the Dynamic Behaviour of Masonry Structures

4.1 Introduction

The pseudo-static experiments on scaled masonry walls, described in Chapter 3, studied the post-crack behaviour of masonry walls under one-way horizontal forces in the static phase. It has been shown that for the masonry structure subject to horizontal forces, cracking and damage behaviour is influenced by a relatively small numbers of geometric and structural parameters (Shi and D'Ayala 2006, Shi, D'Ayala et al. 2008) and does not rely on the type of excitation and the stress status. However, their static nature means that the dynamic behaviour is not complicated, and fails to accurately quantify the "ductility" resources during the hysteretic behaviour. In comparison, shaking-table experiments can apply dynamic forces on the models. The cyclic reciprocating motion, the corresponding damage process and the hysteretic behaviour can be modelled.

Many shaking-table studies have been carried out on masonry models with various objectives, model configurations and analysis methodologies. These studies have mostly focused on specific types of buildings in a local area (Manos and Clough 1986, Benedetti, Carydis et al. 1998, Cohen, Klingner et al. 2004). The structural conditions are usually described through structural stress status (Dafnis, Kolsch et al. 2002, Juhasova, Hurak et al. 2002, Dolce, Mauro, Cardone et al. 2005, Lestuzzi and Bachmann 2007). In these cases, differences between the actual and model materials and the real and shaking-table forces usually result in a large difference between the mechanical behaviour characteristics of model structures and real structures (Lu, Zhou et al. 2007).

On the other hand, this shaking-table experimental study focuses on the post-crack behaviour of masonry structure. The mechanisms of structural response do not rely on the stress status, the material and the scale of the model. As it has been confirmed that the failures in masonry structures mostly occur at the joints, and that the mortar has little effect on damage patterns, a

dry masonry configuration was used. The damage mechanisms were studied in the 3D models in the dynamic phase. The dynamic mechanisms, such as global rocking and separate sliding and rotation, were analysed. The effects of structural parameters and the nature of the excitations were summarized. The experimental observations also provide the basis of the theoretical model in Chapter 5.

4.2 Experimental Programme

4.2.1 Aims and Assumptions

This set of tests is concerned with a study of the damage mechanisms in 3D masonry models and dynamical excitation. The dynamic behaviour is analysed based on the theory of multi-rigid-body dynamics. The intention was to clarify the influence of structural configuration and excitation parameters on the damage mechanism of masonry structures in the dynamic phase. The interactions between façade and side walls are expected to be studied. The experimental basis of the mathematical model in the subsequent theoretical study will be built up.

The model was treated as a global entity when studying damage mechanisms and the rocking. It is assumed that a predominant characteristic frequency can be identified for each model. It is argued that, notwithstanding the fact that the constituent materials of masonry (ie blocks and mortar), are not ductile, substantial dissipation of energy can take place during rocking, impact and sliding. The façade is analysed as a rigid-body system for the rocking behaviour. The bricks within the model, however, are treated as rigid bodies restricted by frictional forces along the joints when studying their separate motions. It is also assumed that there is sufficient frictional force existing between the model and the rigid ground to prevent any translational displacement of the bottom of the wall in relation to the base.

4.2.2 The Shaking-table System

The test programme was carried out on the Instron Structural Testing Multi-Axis Shaking-Table system, as shown in Figure 4.1, in the Department of Mechanical Engineering, University of Bath, UK. It includes a 1700mm×1500mm shaking table with 6 axes, the Labtronic 8800 control system with a Basic 8800 Console, control cards for each axis and SCM data acquisition boards.

Table 4.1 Parameters of Multi-Axis Shaking Table (MAST-9720)

Parameter	Magnitude	Unit
Pay Load used for Calculation	450	Kg
Table Mass	300	Kg
Table Work - Area Dimensions	1700 × 1500	Mm
Peak Acceleration - Vertical	60	m/sec^2
Peak Acceleration - Lateral	48	m/sec^2
Peak Acceleration - Longitudinal	40	m/sec^2
Peak Velocity - Vertical	1.7	m/sec
Peak Velocity - Lateral	1.5	m/sec
Peak Velocity - Longitudinal	1.1	m/sec
Stroke - Vertical	± 75	Mm
Stroke - Vertical	± 125	Mm
Stroke - Lateral	± 75	Mm
Stroke - Longitudinal	± 75	Mm
Operating Frequency Range	0 - 50	Hz
Table Resonant Frequency	250	Hz

Figure 4.1 The IST Multi-Axis Shake Table (MAST) systems

This 6-DOF shaking table is served by three vertical actuators, two lateral actuators and one longitudinal actuator. Detailed information on the shaking table is shown in Table 4.1. The

lateral axis is defined as the y-axis, and the longitudinal axis as the x-axis in the experiments. The excitations were applied using corresponding actuators.

4.2.3 Setup of Masonry Models

The 1/2-scale bricks in Chapter 3 were used, with each of average weight 0.336kg and size 105mm×50mm×35mm (Length×Width×Height). These bricks have a smooth surface with little variability in their physical properties, which means that the repeated use of the bricks in newly built models is a valid approach. The friction coefficient of 0.81 measured in the pseudo-static tests ensures good shear capacity at joints.

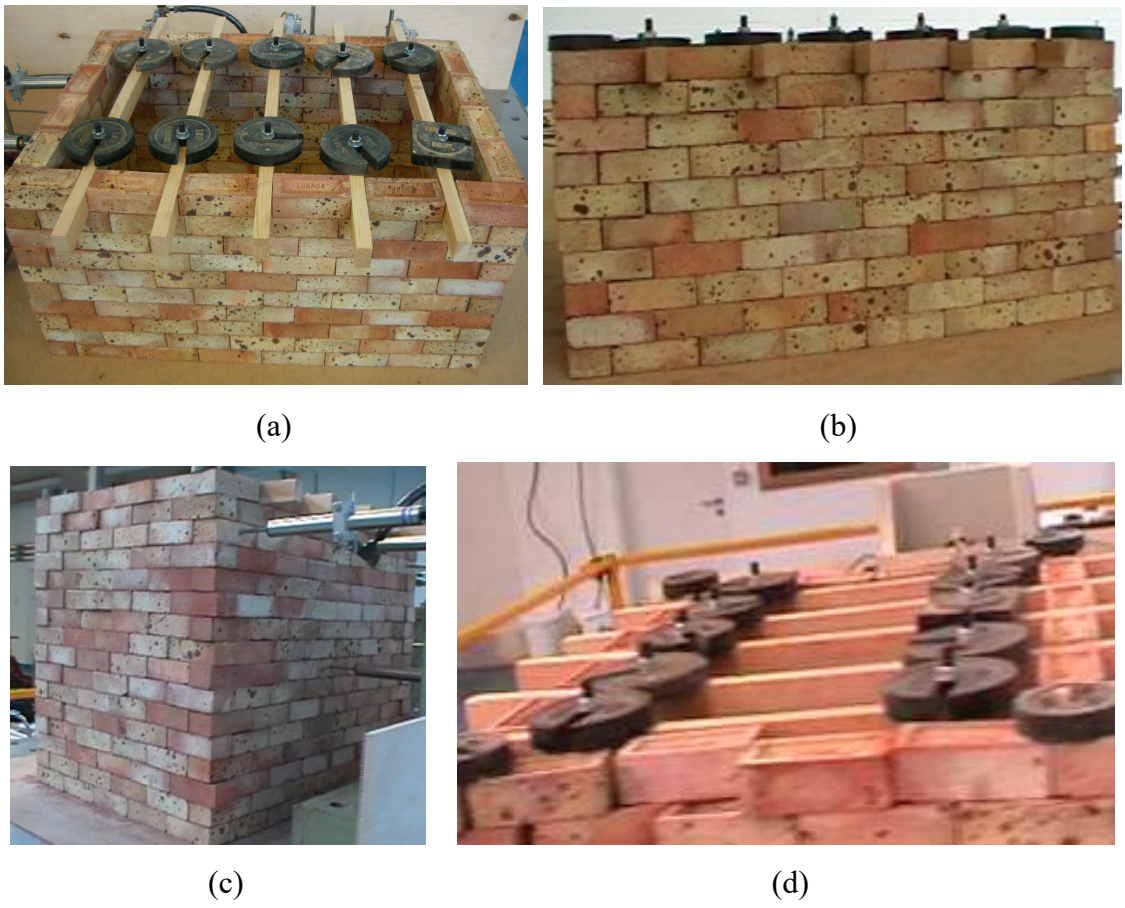

(a) (b)

(c) (d)

Figure 4.2 The three 3D models used in the shaking-table experiments
((a) Model I; (b) Model II; (c) Model III; (d) Additional corner loads)

Three models were tested in this series of shaking-table experiments, as shown in Figure 4.2, respectively marked as Model I, Model II and Model III. They varied in height and roof loading conditions to clarify the influence of these parameters on the damage pattern of masonry walls under reciprocal motions.

The models are 1/10-scale one-storey dry-brick structures. The dry-masonry configuration in the experiments allows quick reconstruction of models and more experiments to be studied within a given time. Models were designed consisting of just the most basic components of masonry structures (four masonry walls and roof loadings), to obtain the most generalized behaviour of masonry structures. They were constructed using stretcher bond with stagger ratio s/h=50/35=1.43 to maintain sufficient friction constraints at the joints. In the experimental studies in Chapter 3, such overlap has been shown to result in good equivalent shear strength of the masonry.

The three models utilised, as shown in Figure 4.2, had the same rectangular plan shape, so that information on façades with different height to length ratios could be collected. The models contained seven bricks transversely and five bricks longitudinally, as shown in Figure 4.2(a), which made a plan dimension of 730mm×525mm ($y \times x$). Use of sufficient number of bricks ensures that the fundamental interaction among parts of masonry walls connected in 3D to form buildings is replicated to reasonable accuracy. Model I and Model II contained the same vertical plane, but differed from each other in their preset loading condition at the corners. Model III varied from Model II with regard to the number of layers in the height, but maintained the same loading conditions on the top. The y-axis model elevations are shown in Figure 4.2(b). Model I and Model II were 315mm high with nine vertical brick layers. The ratios of L/H of façades in horizontal and transversal directions were thus 2.33 and 1.67. Model III was higher, with 15 layers of 525mm in height. The ratios of L/H were respectively 1.39 and 1.0.

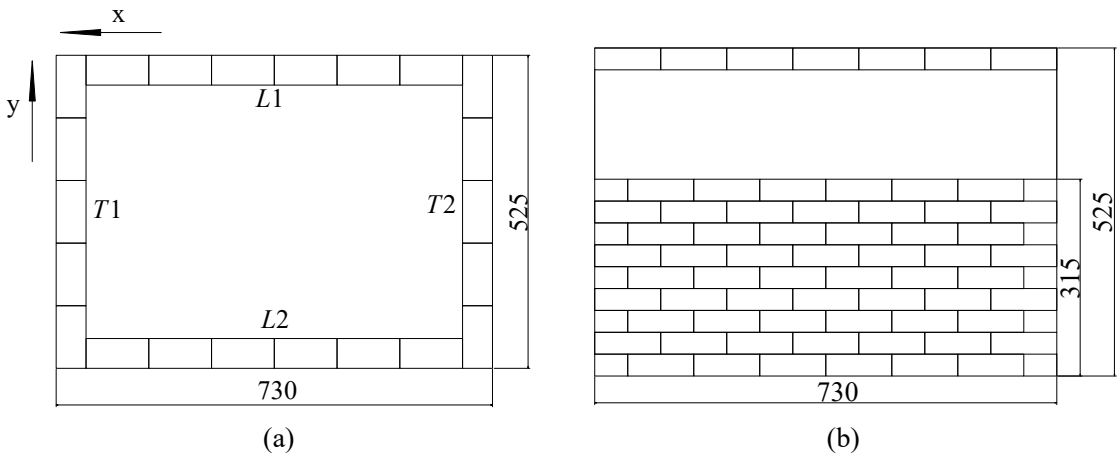

Figure 4.3 Dimensions of 3D models ((a) plan shape (b) vertical shape)

In each model, as shown in Figure 4.3(a), the two longitudinal walls subject out-of-plane

rocking with y-axis excitations were labelled as $L1$ and $L2$. The other two transversal walls were subject to out-of-plane rocking with x-axis excitations were labelled as $T1$ and $T2$.

The simulated vertical roof load applied at the top was 10kg, which was assumed to be uniformly distributed. Five beams were placed evenly on top of the façades and held down by a 1kg steel lumped mass at each end. For Model I, no constraint was applied at corners, as shown in Figure 4.2(a). For Model II and Model III, each corner was loaded with an extra 0.5kg lumped mass at its top to provide some constraint, as shown in Figure 4.2(d). This means that 20% extra roof weight was added. The uniformly distributed loads also ensure that the models can respond as a whole and that the main crack is likely to be clearly evident.

In order to protect the shaking table from damage and dust, models were constructed on a thin timber board bolted to the top of the table. As this board was only approximate 5mm thick and the anchorage is very firm, the models can still be assumed to rest on a rigid base. In addition, as the surface of the board is much rougher than the steel of the shaking table, the extra friction helps to prevent sliding of the bottom layer.

Meanwhile, damage from falling bricks is possible during testing. Due to the fact that the hydraulic control system of the shaking table is exposed, removable vertical boards were bolted at the edge of all sides of the shaking table with sufficient height to contain falling bricks. The two front boards respectively along the two perpendicular axes were made of transparent acrylic to enable video recording in both directions.

4.2.4 The Input Excitations

Sinusoidal signal was selected as the input excitation, which is a simple but commonly applied dynamic excitation. As structural response under the forced vibration is also sinusoidal, the simple form and parameters of the input and output data make them convenient to analyse. Furthermore, as most earthquake signals can be decomposed into a series of sinusoidal signals, the sinusoidal input can generate typical dynamic reciprocal behaviour of the masonry structure from the models.

The sinusoidal inputs were designed with low amplitudes (maximum 12mm) in order to avoid quick collapse, and to obtain a stable response during the whole process. A 50-cycle excitation was applied in each test to maintain a complete respond process. One of the objectives of the tests was to clarify whether the level and mechanism of damage are sensitive to the

acceleration of the input or to its frequency. Therefore, the input frequency varied following two principles in different groups of tests on each model: 1) under constant amplitude, and 2) under constant peak acceleration. The series of tests is outlined in Appendix I. On Model I, two series of sinusoidal signals were applied, varying in frequency but at constant amplitude and constant peak acceleration respectively. As it was found that structural response is actually frequency-sensitive, the excitations were applied at constant peak acceleration to Model II and Model III.

4.2.5 Measuring Equipment and Data Interpretation

Two video cameras were set up in front of walls *L*2 and *T*2 to record structural behaviour. To guarantee that the in-plane sliding, out-of-plane rocking and corner rotation could be recorded clearly, all the instruments used were placed on walls *L*1 and *T*1 at the back, as shown in Figure 4.4.

Six transducers and five accelerometers were utilised. Model I was first tested with only transducers. Tests on Model II and Model III utilised both transducers and accelerometers. The instruments were placed at penultimate layer of each model, that is, at the eighth layer on Model I and Model II and at the 14th layer on Model III. This was because the top layer bricks are more vulnerable to the possibility of falling down and to moving individually. The transducers were bolted to the shaking table, measuring the displacements between table and model in millimetres. The accelerometers were attached directly to the bricks along the directions of motions being measured. Accelerometer measurements are in units of *g*.

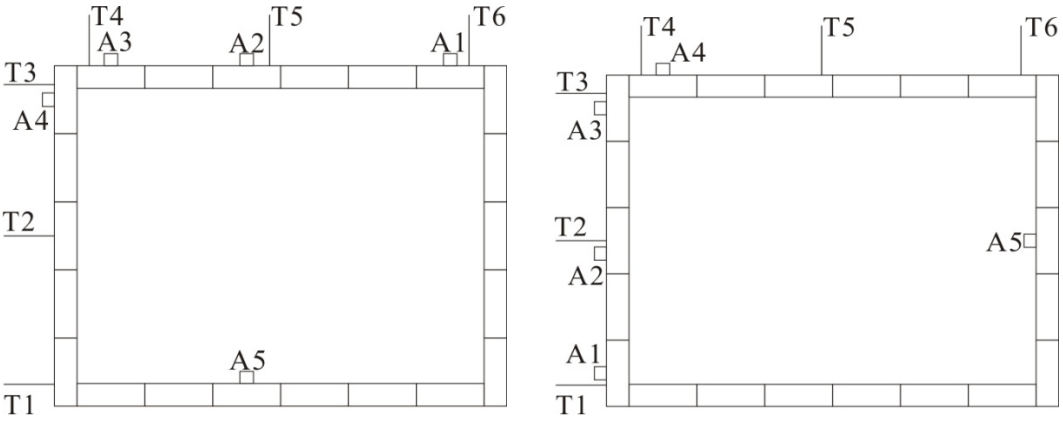

(a) Case of y-axis excitations (b) Case of x-axis excitations

Figure 4.4 Plane view of the arrangements of transducers and accelerometers on models (A1-A5 represent the accelerations and *T*1-*T*6 represent the transducers)

The shaking-table system itself contained three transducers to give input displacements in the x, y and z directions. One accelerometer was attached to the shaking table along the directions of excitation to collect input accelerations. For all models, the out-of-plane and in-plane horizontal motions at different locations were measured. In Figure 4.4, the six transducers were respectively set up at the centres and two corners of the façade and side wall. Three accelerometers were attached to the centre and corner bricks of the façade. The fourth was applied orthogonally on the corner brick to assess its in-plane motion. The last was used on the centre brick of the front façade to facilitate collection of clearer information on the out-of-plane rocking. Data collected from the instruments located in the centre and two edges can together allow the deformed shape on the top of the model under each direction of excitation being drawn.

On the basis of the accelerations *a* and displacements *ds* directly measured by accelerometers and transducers, the following quantities have been derived to analyse the out-of-plane behaviour of the façade:

1) The relative displacement and relative acceleration of the middle brick to the corner bricks: *dsr* and *ar*;
2) The accelerometer-derived displacement calculated by integrating twice the acceleration in the middle of the top layer: *da*;
3) The relative accelerometer-derived displacement between *da* in the middle and at the corners of the top layer: *dar*;
4) The velocity and relative velocity obtained by respectively differentiating *ds* and *ds*: *vs* and *vsr*;
5) The velocity and relative velocity derived from the accelerometer by integrating *a* and *ar*: *va var*
6) The amplifications of the above quantities relative to the corresponding quantities of input;
7) The kinetic energy *E* of the out-of-plane rocking calculated by integrating the mass of the excited portion with the acceleration and displacement of response;
8) The unit drift, a measure of façade deformation: the drift in the middle of the top layer caused by excitation of unit amplitude.

The amplifications above are defined as the ratio of the model response amplitude when it has settled into a steady state to the excitation amplitude as:

$$Amplification = \frac{(Positive\ amplitude - Negative\ amplitude)in\ the\ middle\ of\ top\ layer}{(Positive\ amplitude - Negative\ amplitude)\ of\ the\ excitation}$$

The unit drift is then described as:

$$Unit\ drift = \frac{Amplification\ of\ dar}{Height\ of\ the\ facade}$$

These quantities describe the dynamic behaviour from different perspectives. Quantities derived from readings of transducers include all information on the movements of bricks. Quantities derived from the accelerometer readings only contain information on the out-of-plane rocking of the façade. The relative parameters of the middle façade to the corners relate to the arching effect at top of the façade. The amplifications quantify the levels of model response to the excitations imposed. The kinetic energy is a measure of the magnitude of the global out-of-plane rocking.

For Model I, as only transducers were used, quantities relevant to the acceleration and the kinetic energy are derived theoretically from transducer displacements as follows.

For the sinusoidal excitation as $y_{in} = A_{in}\sin(\omega_{in}t + \varphi_{in})$, the output displacement can be expressed as a Fourier series:

$$y_{out} = \frac{a_0}{2} + \sum_{k=1}^{i}(a_k \cos kx + b_k \sin kx) = \frac{a_0}{2} + \sum_{k=1}^{i}\sin(kx + \varphi)$$

As the positions of both shaking table and model are reset to zero before each test, a_0 is equal to zero. Selecting only the first order term of this Fourier series, the displacement of response can be also considered as a sinusoidal signal:

$$y_{out} = A_{out}\sin(\omega_{out}t + \varphi_{out}) \tag{4-1}$$

As an initial applied motion, it can be assumed that the applied movement has the same frequency as the forcing sinusoidal input ($\omega_{out} = \omega_{in} = \omega$). Then the response acceleration becomes:

$$a_{out} = y''_{out}(t) = A_{out}\omega^2 \sin(\omega_{out}t + \varphi_{out}) = \omega^2 y_{out}(t) = (2\pi f)^2 y_{out}(t) \tag{4-2}$$

In this way, the forcing wave to excite the out-of-plane rocking on the model is:

$$F(t) = m_g a_t = m_e(2\pi f_{out})^2 y_{out}(t) \tag{4-3}$$

where m_e is the mass of the portion being excited participating in the out-of-plane rocking.

On this basis, the kinetic energy in the whole rocking process can be represented by the displacement data as:

$$E = \frac{1}{2} m_e (2\pi f_{out}(t_i))^2 \sum_{i=1}^{n} [y_{out}(t_i) + y_{out}(t_{i-1})] \times [y_{out}(t_i) - y_{out}(t_{i-1})] \quad (4\text{-}4)$$

4.2.6 Testing Programme and Procedure

For the series of tests outlined in Appendix I, each test has been replicated three times to ensure consistency. The test with the most stable global response process and the least random separate motions on bricks was selected for analysis. For each new run, the model was rebuilt in order to avoid the risk of the presence of any weakness induced by previous testing.

Tests were conducted respectively along the x and y axes with groups of excitations. On Model I, a group of excitations with the constant amplitude of 12mm was applied along each axis, in order to establish whether the dynamic behaviour relies on increasing input energy as the frequency of excitation increases. The groups of excitation, based on a constant peak acceleration as 1.71mm/s^2 along the x axis and 1.53mm/s^2 along the y axis varying in the frequency, were then applied separately.

On Model II and Model III, based on the frequency-sensitive characteristics of the dry masonry model verified from Model I, the groups of excitations varying in frequency based on the constant peak acceleration were used along x and y axes respectively. The peak accelerations for the groups of excitations on Model II correspond to the peak accelerations applied to Model I (ie 1.71mm/s^2 for x axis excitations and 1.53mm/s^2 for the y axis cases). Tests were also conducted for a direction of excitation along the diagonal of the model plan and for the x = y case on Model II, by applying the group of y-axis excitations in both axes simultaneously. For Model III, to allow for safety in case of bricks falling from the higher façade, lower input amplitude of 5mm was used for the set of tests with excitations along the y axis.

In each test, displacements and accelerations were collected. The response and damage processes on the façade and the side wall were recorded by two cameras. Analysis was carried out as will be described in the next section.

4.3 Analysis on the Experimental Results

This section presents an analysis of the observations and data derived from the shaking-table experiments. For each model, the observed dynamic behaviour, damage pattern, its development and its variation were first studied. Further analysis of the test data is then provided. The differences in dynamic behaviour of the three models are discussed in terms of the influence of the constraints and of the model geometry. The characteristics of the rocking behaviour presented in the dynamic tests that can be used as the basis of the theoretical model are discussed.

Both the pseudo-static tests (D'Ayala, Dina, Shi et al. 2008, Shi, D'Ayala et al. 2008) in Chapter 3 and extensive on-site post-earthquake observation (D'Ayala, D. and Speranza 2003, D'Ayala, D. and Paganoni. 2011) have shown that under lateral action, masonry walls are more vulnerable to out-of-plane failure than in-plane failure. This was again confirmed by the shaking-table tests. The discussion here therefore focuses on the out-of-plane rocking of the façade in each model. Differences between the monotonic static tests carried out on single walls with wings and the reciprocal dynamic tests on 3D models are discussed. The experimental basis for the theoretical model in the following work also focuses on out-of-plane rocking.

4.3.1 Analysis of Model I

Two groups of excitations were applied in each direction. One used a constant amplitude of 12mm with variable frequency and acceleration. The other varied in frequency and amplitude with constant the peak acceleration which is respectively 1.71mm/s^2 along the x axis and 1.53mm/s^2 along the y axis. The input frequency varied between 1.7Hz and 3.6Hz. The model was repeatedly rebuilt between tests.

4.3.1.1 Observations

Generally, Model I was found to respond consistently to excitations along different axes. The dominant behaviour was the out-of-plane rocking, accompanied by in-plane sliding of the side walls along stepped lines and rotation of the corner bricks. The rocking portion of the façade was seen to be similar in different experiments. Without external constraint at the top, bricks at corners separate from the model due to rotation and sliding.

For experiments involving excitation along the y axis, observations at an excitation of constant

12mm amplitude are as follows. Similar observations are shown consistently at an excitation with constant peak acceleration. The rocking portion was shown by the black line in Figure 4.5-4.9(a) on the façade and in Figure 4.5-4.9(b) on the side wall. On the façade, eight layers from the top are included in the excited rocking portion, which can be divided into two parts. The upper part completely includes the top five layers. The lower part starts from the upper part from the sixth layer. The bricks being contained in this part reduce from the two edges to the middle in each layer along two stepped joint lines. On the side wall, the portion being included in the rocking also develops from the middle of the top layer, along the stepped joint line to the edge of the fifth layer. In addition to the rocking, rotation can also be observed in the adjacent portion at corners, as marked by the red lines in Figure 4.5-4.9(b). The upper and lower parts of the excited portion rocks as a rigid panel during the response, rocking out of plane. Meanwhile, the upper rocking part contains part of the side wall and the lower part is constrained separately in the middle within the façade. Due to difference in their structural configuration, slight relative rocking between the lower part and the upper part can be observed. This separate extra rocking causes a greater response of the bricks in the upper part and the larger rocking arch in the middle.

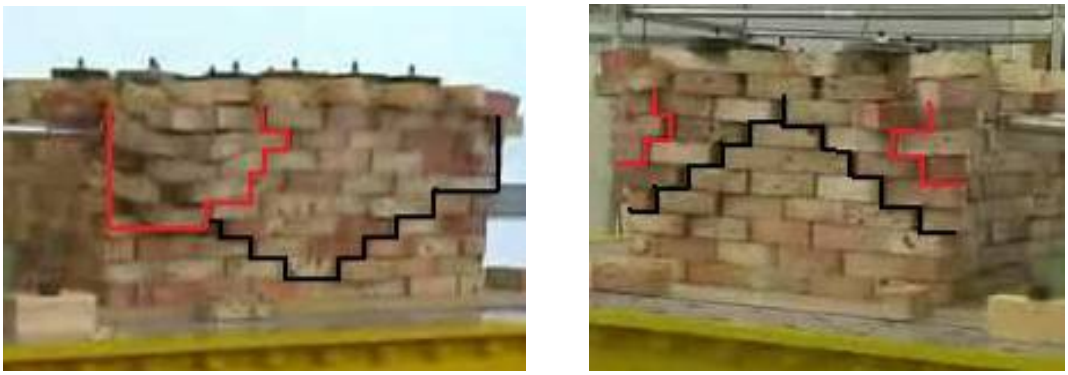

(a) (b)

Figure 4.5 The response of Model I on y-axis 1.8Hz 12mm excitation
((a) the façade; (b) the side wall)

At 1.8Hz, the integral rocking on the excited portion becomes observable in Figure 4.5(a, b). A little higher extent of rocking can be observed from the upper part, which generates the arching shape in the middle in Figure 4.5(a). The corners are only slightly involved in rocking but show clear separate rotations on the portion marked by the red line in Figure 4.59(a). Sliding occurring in the side walls is also observed along the symmetric stepped cracks shown by the black line in Figure 4.5(b). The final collapse is caused by rapid rotation of the top bricks at both corners.

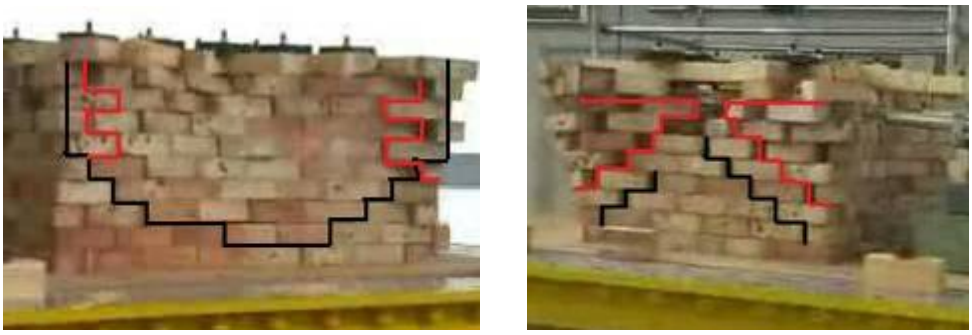

(a) (b)

Figure 4.6 The response of Model I on y-axis 2.0Hz 12mm excitation

((a) the façade; (b) the side wall)

At 2.0 Hz in Figure 4.6, the excited portion shows more substantial involvement of the corners. The rocking gradually becomes Mechanism B2 as the dominant structural response, with the corner rotation becoming smaller. The main crack is caused between the excited portion and the rest of the structure due to the out-of-plane rocking along the black line in Figure 4.6(a, b). The arching shape is formed in the upper part of the excited portion, with a litter larger rocking behaviour being observed. Some slight cracks are observed due to in-plane sliding. Initial collapse occurs at the corner as a combination of rocking and rotation.

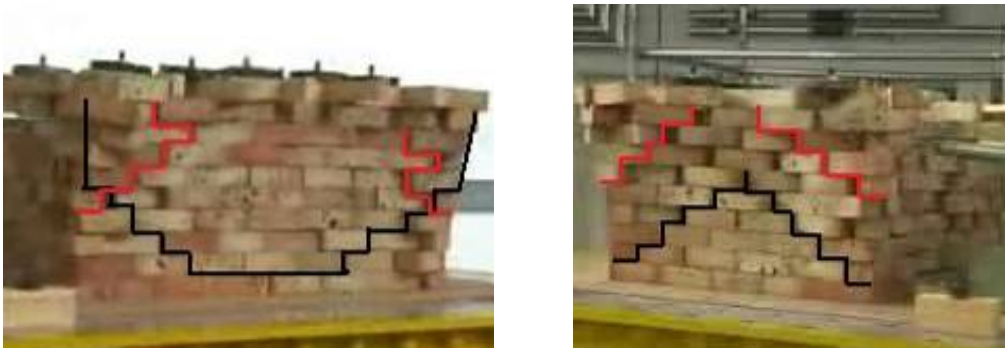

(a) (b)

Figure 4.7 The response of Model I on y-axis 2.2Hz 12mm excitation

((a) the façade; (b) the side wall)

The dominance of the out-of-plane rocking is reduced at 2.2Hz. In Figure 4.7, corner bricks at all layers slide and rotate separately so that the façade and side walls are isolated. The integrity of the rocking portion is reduced with more and clearer cracks within it. The main cracks are clearly generated by sliding in the side walls. Collapse also starts from the corners and occurs later on the whole façade.

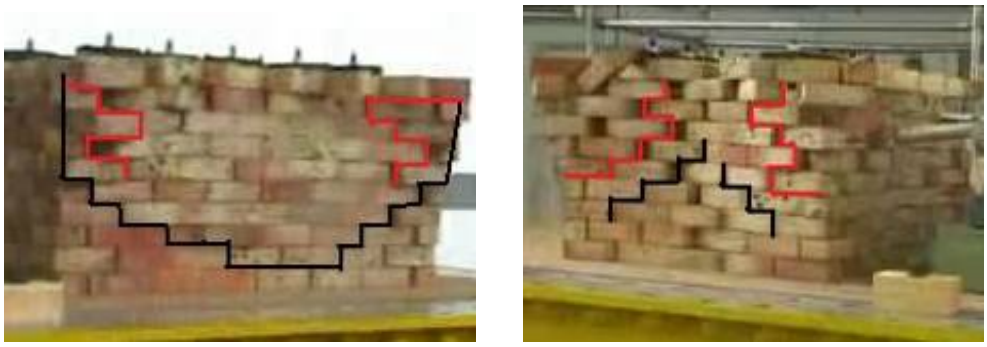

(a) (b)

Figure 4.8 The response of Model I on y-axis 2.5Hz 12mm excitation

((a) the façade; (b) the side wall)

The structural behaviour at 2.5Hz continues to vary consistently with the behaviour at 2.2Hz. As shown in Figure 4.8, the out-of-plane rocking becomes even less influential on the global structural response. More active rotation occurs at corners of all layers. The corner collapses from the top, while the façades do not collapse at the ends because of the reduced extent of rocking.

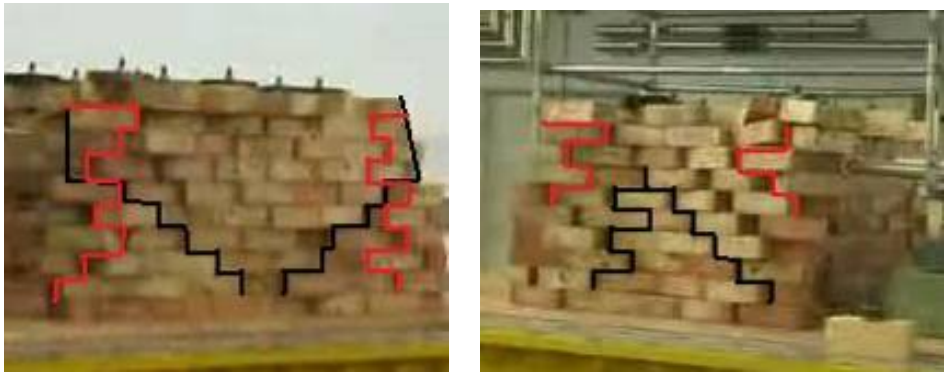

(a) (b)

Figure 4.9 The response of Model I on y-axis 3.6Hz 12mm excitation

((a) the façade; (b) the side wall)

In Figure 4.9, the out-of-plane rocking continues to attenuate at 3.6Hz. Separate rotation occurs in larger portions at corners and dominates the whole structural response. As shown in Figure 4.9(b), the whole side wall is divided into two parts from the middle along the joints and rotates separately in opposite directions. Hence, the final failure occurs quickly on the side wall.

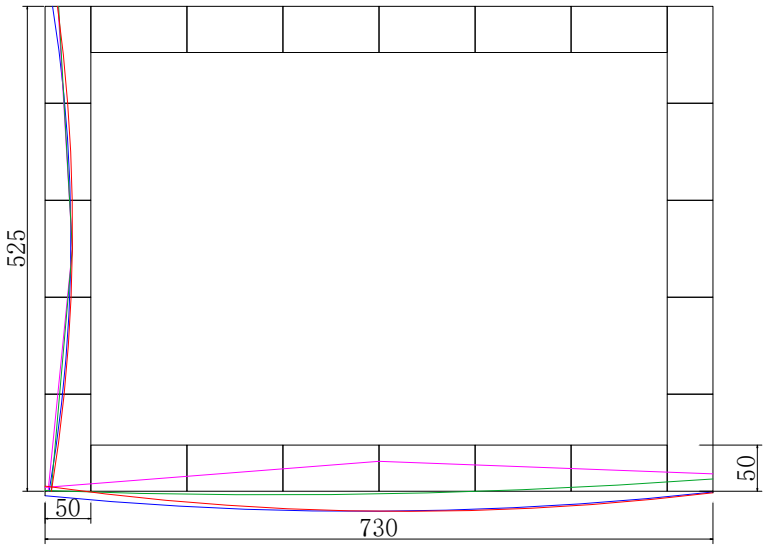

(a)

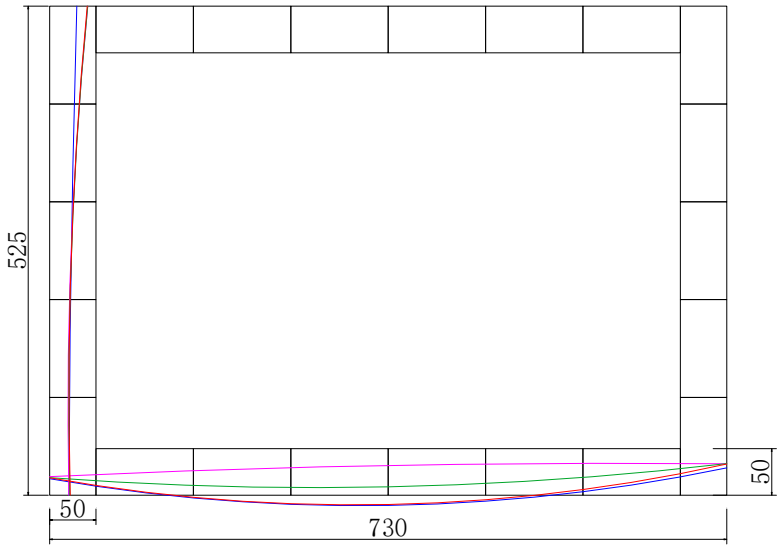

(b)

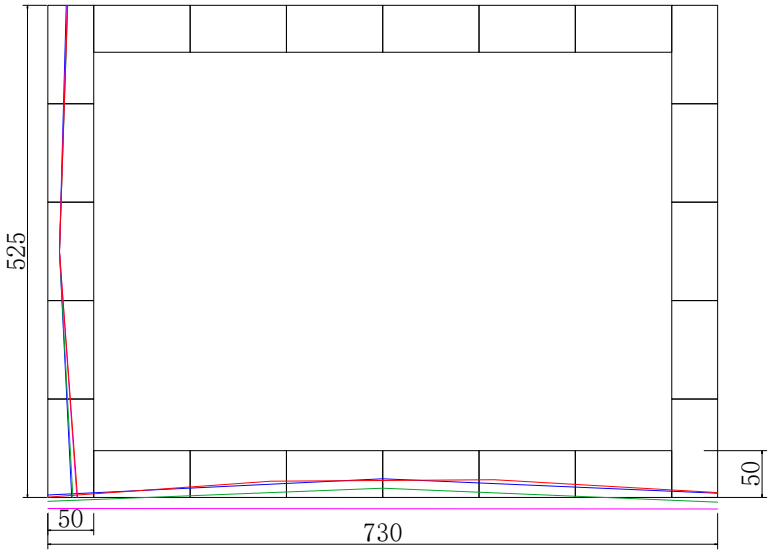

(c)

Figure 4.10 Deformed shapes by excitations with constant amplitude in y
((a) 1.8Hz 19th cycle; (b) 2.0Hz 12th cycle; (c) 3.6Hz 4th cycle)
(positive peak zero point negative peak positive peak2)

To present deformed process of the model more clearly, the deformed shape of the top layer is drawn using the data of *ds* collect from the middle and corners of *L*2 and *T*2. One typical rocking cycle is selected to be presented in each graph, which is defined to start from the point that the central façade is in its maximum positive deformed position, and end when the central façade returns to another maximum positive position. Within the selected cycle, four critical points relevant to the following moments are chosen: the central façade reaches its maximum positive displacement at the beginning and the end of one rocking cycle, the central façade reaches its maximum negative displacement and the central façade presents no deformation.

In Figure 4.10, the deformed shapes of Model I under y-axis excitations are drawn. Figure 4.10 (a-c) show the deformed shapes at excitations with different frequencies and constant amplitude. Consistent and clear deformation is observed on both façade and side wall in all three graphs. Besides, in all examples, the deformed curve on the façade returns to its original place at the end of each cycle. The shape of the side walls remains constant during the whole rocking cycle. Therefore, in spite of the separate motions on bricks, Model I still shows global response and consistent structural response in the stable stage. However, due to the active separate motions of discrete bricks, the curves are only representative of the response in the short stable stage.

Figure 4.10(a, b) show the structural deformations within the effective range of excitations. The smallest corner displacements are shown at 1.8Hz in Figure 4.10(a), also with the larger out-of-plane arch in the middle of the façade. These consistently demonstrate the dominant global rocking as the response close to the resonance. The middle arch on the side wall is generated by the rotation of bricks during the rocking. At 2.0Hz excitation in Figure 4.10(b), the arching shape in the middle of the façade is similar to the shape at 1.8Hz. However, the corner displacements are shown clearly and cause translational movement of the side wall. The more active separate motions of corner bricks also causes the undeformed shape of the façade becomes an arch shape in the negative direction. Conversely, Figure 4.10(c) at 3.6Hz presents the deformation shape within the ineffective range of excitation. Clearly smaller arches occur in both middle of the side wall and façade. The displacements at corners due to separate motions on bricks are relatively larger than the arching deformation, which supports the former observation that corner rotation dominates the structural response.

With x-axis excitations, *T*1 and *T*2 with lower *L/H* ratios display out-of-plane rocking. Taking the group with constant input amplitude of 12mm, the basic dynamic behaviour and variations are consistent with those under y-axis excitations. The constant excited portion in the narrower façade *T*1 and *T*2 becomes smaller, marked by the black lines in Figure 4.11-4.14. The upper part contains the three complete layers from the top. The lower part contains bricks in the following three layers within the stepped lines. Consistently with the observations of the y-axis rocking, the excited portion presents integral rocking behaviour. The clearer arching shape and a little larger rocking are observed in the upper part. The separate sliding and rotation are observed at corners within the red lines.

(a) (b)

Figure 4.11 The response of Model I on x-axis 1.8Hz 12mm excitation
((a) the façade; (b) the side wall)

The excited portion rocks with the best integrity and the least cracks within it at 1.8Hz. As

shown in Figure 4.11(a), the out-of-plane rocking dominates the structural response. Corner bricks only rotate slightly along the red line in Figure 4.11(b), with sliding hardly observed on the side walls. The final collapse is caused by out-of-plane rocking on the upper part at the corner of *L*2 and *T*1.

(a) (b)

Figure 4.12 The response of Model I on x-axis 2.0Hz 12mm excitation
((a) the façade; (b) the side wall)

At 2.0Hz, the rocking becomes less dominant and changes to a Mechanism A along the black lines in Figure 4.12(a). The corners are hardly included in the rocking of the excited portion. More cracks occur within the excited portion. The separate sliding of bricks in the façade is mostly presented in the upper part. The bricks in the lower part, with better constraints from the adjacent bricks, show limited separate motions during rocking. Clear rotation is presented within the red lines. Only the bricks of the top layer fall off the wall towards the end of the excitation. Similar structural behaviour also occurs at 2.2Hz and 2.5Hz.

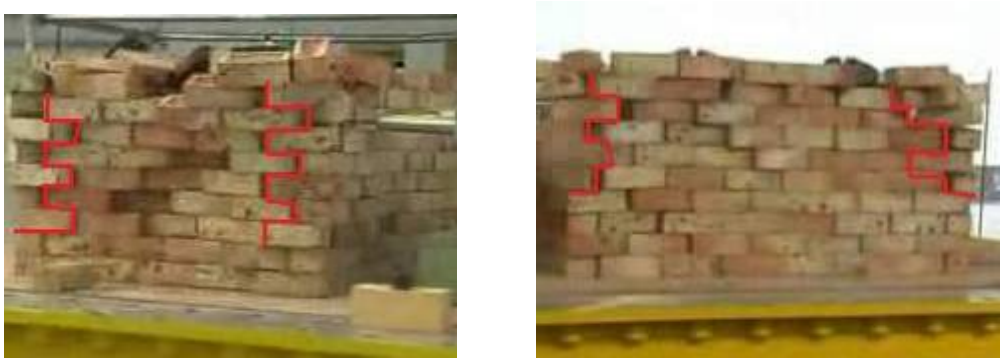

(a) (b)

Figure 4.13 The response of Model I on x-axis 3.6Hz 12mm excitation
((a) the façade; (b) the side wall)

When the frequency increases to 3.6Hz, rocking is hardly evident. The slight sliding is only shown in the middle of the upper part. Only strong corner rotation is observed. In Figure 4.13(a), the rotations from corners force the façade to separate into two parts at the centre and rotate in opposite directions. The rotation and sliding destroy the integrity of the façade and cause its final collapse.

Therefore, similarities are shown in the structural behaviour and the variations with excitations along the x and y axes. A constant excited portion is shown to rock at different excitations in each axis. This portion is consistently divided into two parts by the different structural configurations. The upper part contains the bricks in the whole layer and the bricks in the corresponding side walls. The lower part only contains the bricks in the middle of the following layers within the two stepped joint lines. The upper and lower parts integrally present the out-of-plane rocking. Meanwhile, the upper part shows extra rocking, clearer arching shape and more separate sliding on bricks.

The extent and dominance of the out-of-plane rocking do not increase monotonically with the increasing input peak acceleration but are sensitive to the frequency of excitation. The rocking portion which presents higher dominance in the global response also more effectively includes two corners and shows less tiny cracks within it. In these cases, the separate motions of bricks and rotation at corners become much smaller in contrast. However, the different geometrical forms between façades rocking respectively along y and x axes cause some differences in detail. For the x-axis response, the dominant rocking exists at fewer frequencies. The corners are more effectively included into the excited portion and the mechanism is more typical of Mechanism B2. Correspondingly, their separate rotations decrease. The corner rotation develops more quickly and has a greater degree of influence. The global structural response and the ultimate failure are more easily dominated by corner rotation.

Figure 4.14(a-c) gives the deformed shapes of the top layer in Model I under x-axis excitations. Figure 4.14(a) and (b) present the deformed shapes at effective excitations, while Figure 4.14(c) offers the deformed shape at ineffective excitation. The variations of the deformed shape in these three cases are consistent with the experimental observation in Figure 4.11 to Figure 4.14. As for the shapes in Figure 4.10 under y-axis excitations, arching shapes are generated in both the façade through rocking and the side walls by the rotation of bricks, but both with much smaller deformations.

For the effective range in Figure 4.14(a) and (b), the side wall stays in a constant shape within

the selected cycle, with little deformation at corners in both cases. The façade also returns to the original deformed position when it reaches the second positive peak. Therefore, the corners shake with the façade more synchronously in the excited portion in x axis. Figure 4.14(b) at 1.9Hz gives relatively smaller translational displacement on the façade, as well as a clearer arching shape. The deformed shape at ineffective excitation in Figure 4.14(c) presents a different graph. The larger displacements at corners and the larger variations on shape of the façade between the beginning and the end of the cycle both show the reduced stability of structural response. The more separate motions generate a clearer arch shape in the middle of the side wall. The deformation of the façade is influenced to a large extent by the separate motions of bricks.

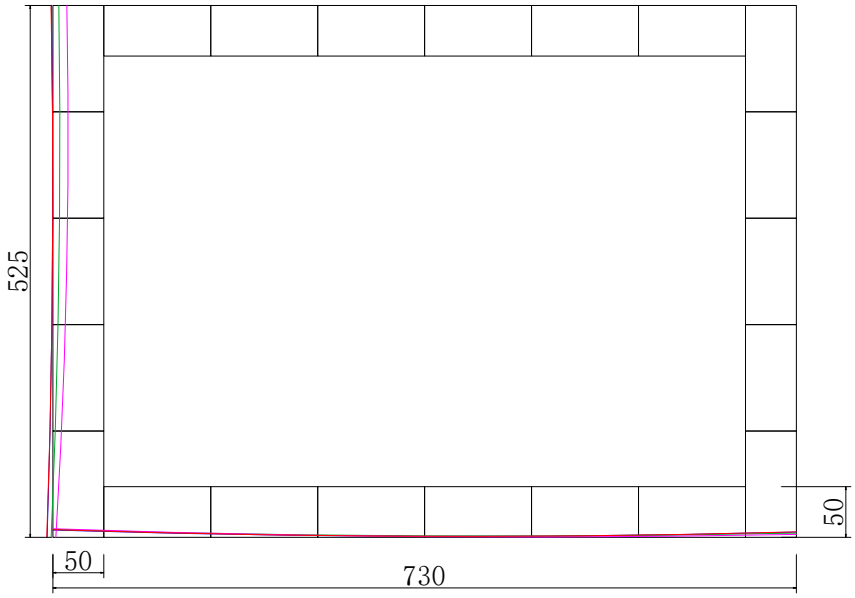

(a)

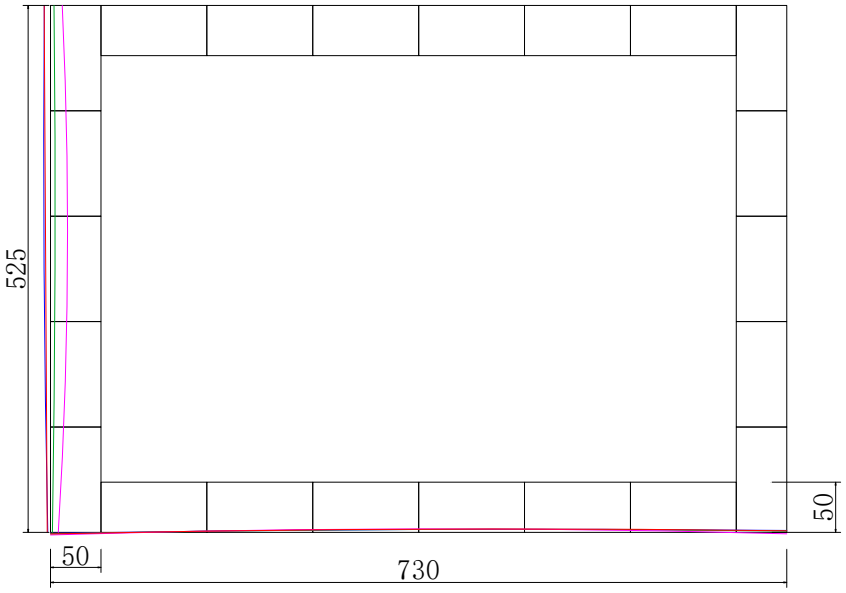

(b)

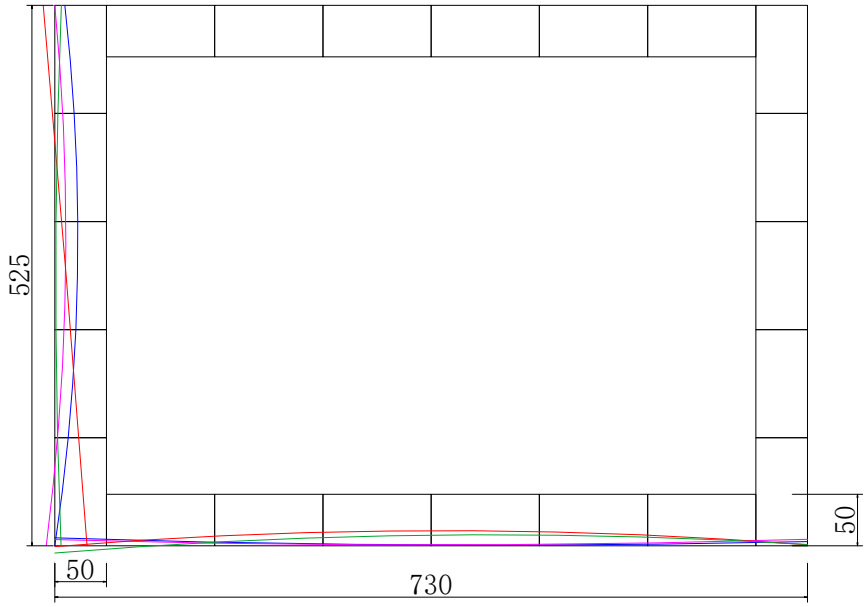

(c)

Figure 4.14 Deformed shapes by excitations with constant amplitude in x
((a) 1.8Hz 12th cycle; (b) 1.9Hz 7th cycle; (c) 2.5Hz 3rd cycle)
(positive peak zero point negative peak positive peak2)

The analysis on the observations and deformed shapes above shows that the extent of rocking does not increase linearly with the intensity of excitation. The constant rocking portion and the consistent behaviour of the two parts in the rocking portion are illustrated. However, the lack of constraint at corners on Model I is also observed. The active separate motions of the corners reduce the constraint within the structure, influence rocking of the façade and initiate the final collapse. The necessity of modifying the corner constraints is clear.

4.3.1.2 Analysis of Experimental Data

This section provides the analysis of the experimental data on Model I. Based on the direct observations above, this analysis is more reliable, elaborate and thorough. Because it has been observed that the dynamic behaviour is frequency-sensitive, the analyses focus on how dynamic responses are affected by variations in frequency.

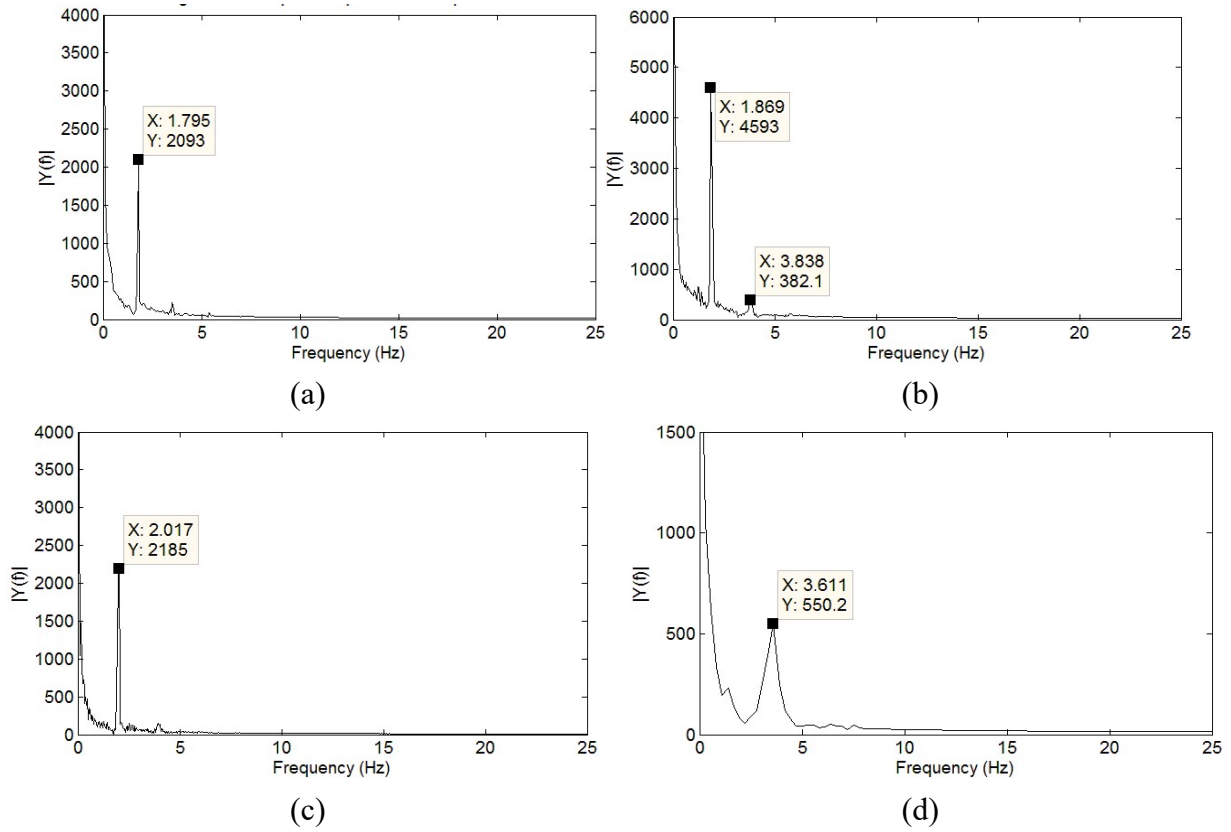

Figure 4.15 The single-sided amplitude spectrums on the output *ds* in x axis of Model I ((a) at 1.8Hz; (b) at 1.9Hz; (c) at 2.0Hz; (d) at 3.6Hz)

A Fourier transfer was applied to the output *ds*. Results in Figure 4.15 for the x-axis tests and Figure 4.16 for the y-axis tests confirm that the response of Model I is sinusoidal. The response displays identical frequency, consistent with the frequency of excitation. This also emphasises the fact that the separate brick motions do not interrupt the global structural response. The assumption that the Model I acts globally is validated. The only exception occurs in the case of y-axis rocking at 3.6Hz, which presents three peaks in total. This is generated by the considerable separate motion of bricks in the small amplitude of rocking with ineffective excitation. In addition, the magnitudes of FFT results in each case also illustrate the extent of structural response to each case of excitation.

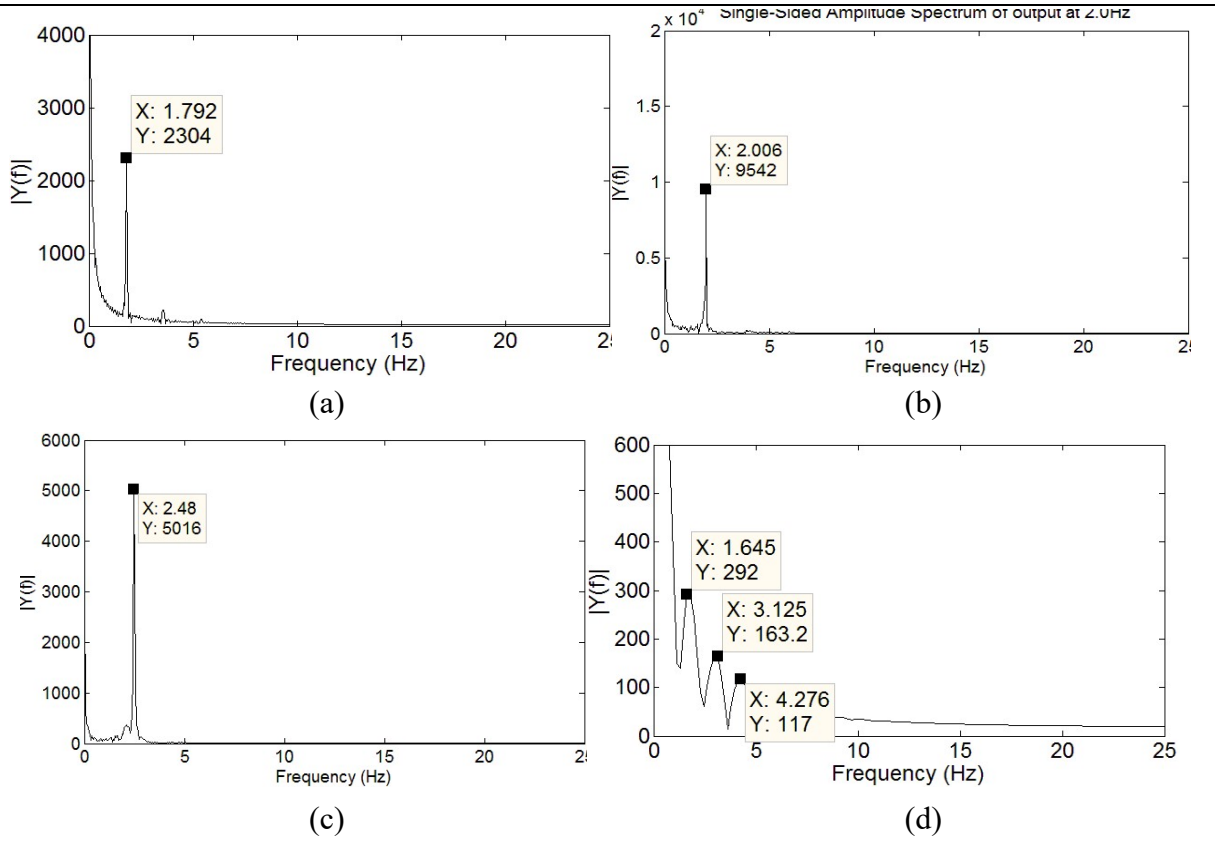

Figure 4.16 The single-sided amplitude spectrums on the output *ds* in y axis of Model I ((a) at 1.8Hz; (b) at 2.0Hz; (c) at 2.5Hz; (d) at 3.6Hz)

Firstly, the hysteresis loops are drawn. This can provide the force-displacement relationships at the centre of the top layer during the rocking of Model I. The force used by the hysteresis loops is calculated by $F = ma$ where m is the total mass of the excited portion shown in the former section and a is the acceleration measured in the centre top layer of the façade. Recognising the errors arising from the separate motions of bricks and the structural damage, only the period of stable responses was considered. As only transducers were used on Model I, accelerations here were derived from the measured displacements. With the displacement as:

$$y_{out} = A_{out} \sin\left(\omega_{out} t + \varphi_{out}\right), \tag{4-1}$$

the acceleration is derived as:

$$a_{out} = A_{out}\omega^2 \sin\left(\omega_{out} t + \varphi_{out}\right) = \omega^2 y_{out}(t) = (2\pi f)^2 y_{out}(t) \tag{4-2}$$

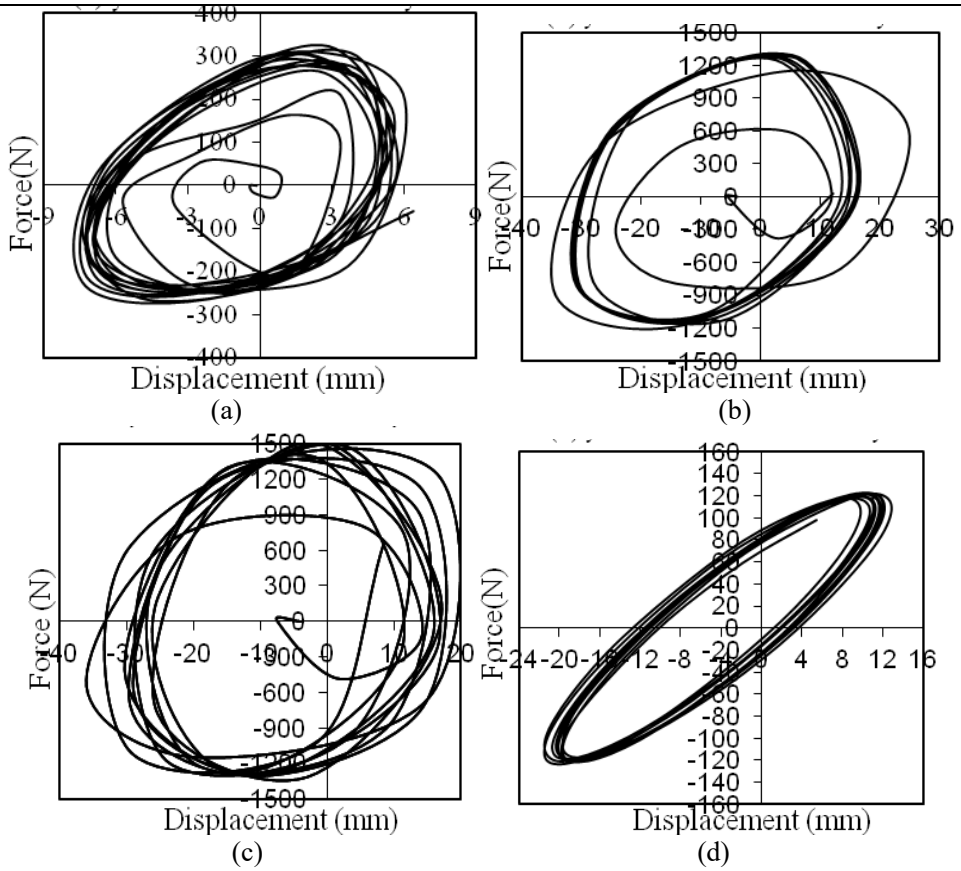

Figure 4.17 Hysteresis loops of Model I in y-axis rocking

((a) y-1.8Hz 12mm 1st-13th cycles; (b) y-2.0Hz 12mm 1st-8th cycles; (c) y-2.2Hz 12mm 1st-9th cycles; (d) y-3.6Hz 12mm 1st-10th cycles)

No loss of stiffness is shown in the loops of the four cases of y-axis rocking in Figure 4.17. This confirms the consistency and integrity of the model in the stable stage of rocking. Slight nonlinearities exist at 1.8Hz and 2.0Hz, demonstrating the greater response in these two tests. The open hysteresis loops indicate the existence of energy dissipation during the reciprocal rocking of this discrete rigid-body model. This may be caused by the friction at the joints, the impulsive effect or the plastic characteristics of the out-of-plane rocking.

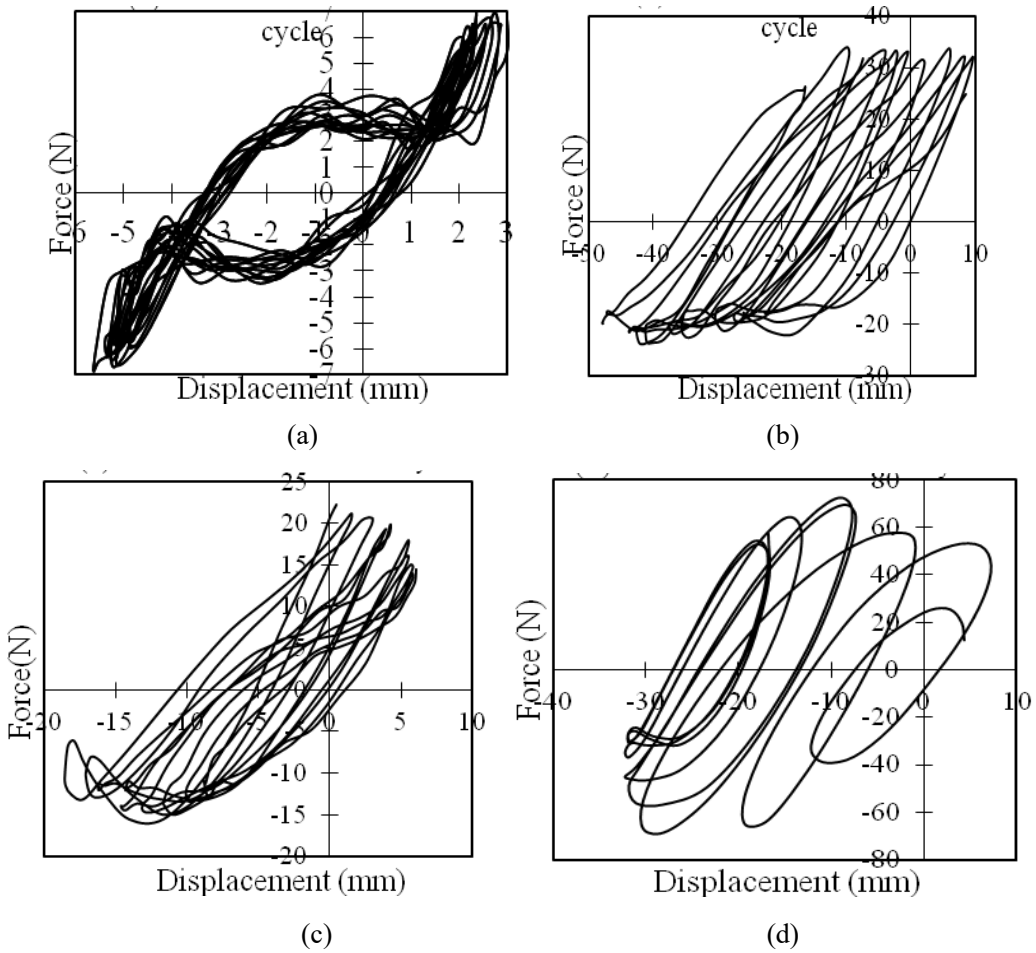

Figure 4.18 Hysteresis loops of Model I in x-axis rocking
((a) x-1.7Hz 12mm 5th-22nd; (b) x-1.9Hz 12mm 18th-29th cycles; (c) x-2.0Hz 12mm 5th-15th cycles; (d) x-3.6Hz 12mm 3rd-10th cycles)

The hysteresis loops for the x-axis rocking of Model I in Figure 4.18 differ from the loops for the y-axis rocking in Figure 4.17. The stable stage is restricted to a relatively small number of cycles with gradually greater variation caused by the separate movements of bricks within the façade. The continuously gradual translation of the loop with time is evidence of the sliding of middle bricks during rocking. Much less energy loss is shown in all four cases by the smaller areas within the loops, which illustrates stiffer model behaviour. Degradation in the stiffness of the façade is observed at 2.0Hz and 1.9Hz as heavier damage occurs.

The amplifications of y-axis and x-axis out-of-plane rocking respectively in the groups of excitation at constant amplitude and constant peak acceleration are all plotted in Figure 4.19(a) and Figure 4.19(b). The amplification varies consistently with frequency at both cases with increased peak acceleration at constant amplitude and increased frequency at constant peak acceleration, along both axes.

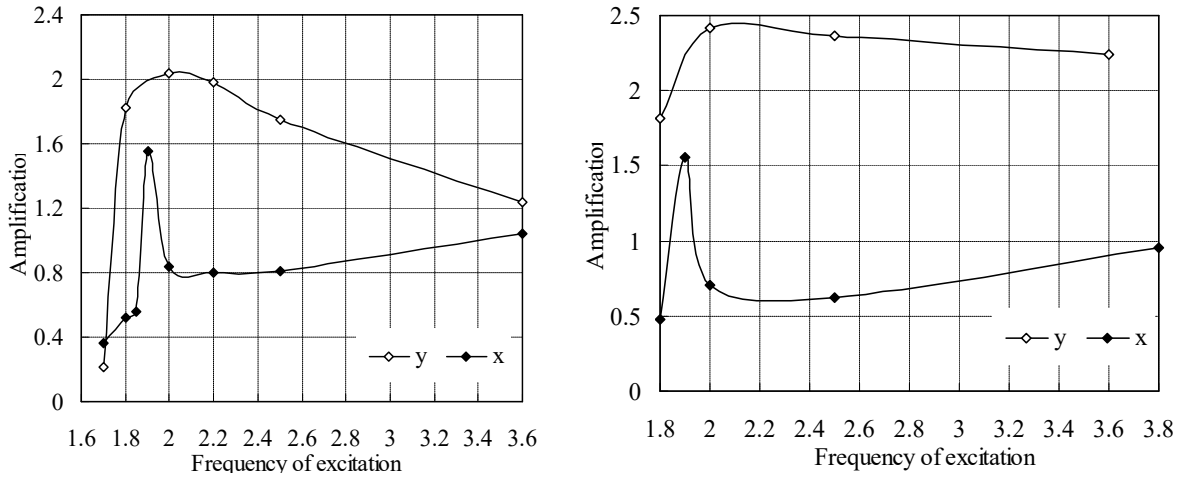

(a) (b)

Figure 4.19 Amplifications of Model I to different excitations

((a) under excitations with constant amplitude; (b) under excitations with constant peak acceleration)

First, the consistent variation proves the reliability of data collected from the repeatedly reconstructed models. Furthermore, the consistency clarifies the frequency-sensitive characteristic of the dynamic response of Model I. In Figure 4.19, the rocking is at an especially high level at a specific frequency which is, respectively, 1.9Hz in x axis and 2.0Hz in y axis. The rocking gradually drop to lower levels as the frequency deviates from that value. In this thesis, the term “characteristic frequency” is used to denote the peak amplification frequency. For the y-axis rocking, the characteristic frequency was 2.0Hz. For rocking in the x-axis direction, the characteristic frequency was 1.9Hz. Allowing for errors due to the different geometric characteristics of the two directions and the active separate brick movements, the characteristic frequencies in the x- and y-axes directions are actually of similar magnitudes. This is consistent with the theory that for a rigid body, the characteristic frequency should only depend on its height and thickness.

In addition, it can be observed in Figure 4.19 that the frequencies are clearly divided into two groups. For a range of frequencies alongside the characteristic frequency, amplifications with considerable magnitudes are generated. Within this range, the amplification value varies consistently while the frequency deviates from the characteristic frequency. The response with amplifications varying in the higher level is defined as the effective response. Correspondingly, the range within the effective responses is nominated as the effective range. The effective

range of frequencies is presented in each curve, with the characteristic frequency in the middle.

This effective frequency range is from 1.8Hz to 2.5Hz for the y-axis rocking. Along the x axis, a much narrower effective frequency range is presented. Furthermore, the x-axis amplifications in the effective range are lower than the corresponding amplifications for y-axis rocking. The inconsistently large reduction of the amplification magnitude at certain frequencies alongside the characteristic frequency is clear in all the four curves. The amplifications reduce to a clearly lower level to continue consistent variations. The response with the low-level amplification is defined as the ineffective response. The range generating the ineffective responses is nominated as the ineffective range.

The variations in amplifications can also be correlated to the corresponding observed structural behaviour described above. A narrower range of effective frequencies exists with the x-axis façade for lower values of *L/H* which presents a poorer deformation capacity and higher vulnerability to failure with little warning. By contrast, the façade with higher *L/H* responded effectively over a wider range of frequencies. The arch in the middle is more plastic to rock with a larger displacement and capacity of deformation before collapse.

Table 4.2 Phase difference of y-axis response to input displacement of Model I

Frequency (Hz)	Amplitude (mm)	Time (s)	Phase (^{o})
1.7	13.45	0.02	1.95
2.0	9.70	0.16	18.33
2.0	12.00	0.20	22.92
2.2	12.00	0.20	25.21
2.5	6.00	0.16	22.92
2.5	12.00	0.18	25.78

Table 4.3 Phase difference of x-axis response to input displacement of Model I

Frequency (Hz)	Amplitude (mm)	Time (s)	Phase (^{o})
1.7	12.00	0.06	5.84
1.8	12.00	0.08	8.25
1.85	12.00	0.08	8.48
1.9	12.00	0.06	6.53
2.2	12.00	0.08	10.08
2.5	12.00	0.10	14.32

The amplification discussed above is a measure of the extent of a response, with the lagging time between output and input given below being a measure of response efficiency. Table 4.2 and Table 4.3 give the lagging times between *ds* and the corresponding input displacements for rocking along both y and x axes.

In Table 4.2 and Table 4.3, except at resonance, the lagging time remains constant over the effective range for vibrations along both axes. It then clearly reduces in the case of ineffective excitations. For the y-axis excitations, the lagging time was around 0.18s in the effective range and 0.02s otherwise. In the case of the x-axis, the corresponding values were respectively 0.08s and 0.06s. At resonance, the rocking occurred at a still smaller lagging time in respect of both directions. As the lagging time remains constant for different frequencies, a higher input frequency then means a larger phase difference. This indicates that the structural responses obtained were more poorly synchronised at higher input frequencies. In addition, the lagging times on the narrower façade in x-axis in Table 4.2 are smaller than those on the y-axis façade in Table 4.3. This may be due to the smaller amplification and lesser deformation capacity illustrated in Figure 4.19.

4.3.1.3 Summary

Model I is the first model investigated in the shaking-table experiments. It is nine layers in height, with a 5×7 bricks plane and top roof loadings. No corner constraint is applied. The excitations were applied along the y and x axes respectively. Two groups of excitations respectively based on the constant amplitude and constant peak acceleration were applied in each axis. The dynamic rocking behaviour of the masonry structure was studied, with the discussion on the accompanied separate motions of individual bricks especially at corners.

The out-of-plane rocking is observed to be the global and dominant behaviour for the masonry model. The rocking is identified to occur in a constant excited portion in each axis of the façade, at different excitations. This constant portion is divided into two parts based on the difference in their structural configurations. The upper part contains all bricks, as well as part of the side wall, in the several top layers. The lower part only contains the bricks in the following layers along the two stepped joint lines from the edges to the middle. The upper and lower parts rock integrally, to form the global response of the masonry model. Differences can also be observed. The upper part presents a little extra rocking, with clearer arching shape in the middle. The separate sliding during rocking is also clearer on bricks. The lower part is

better constrained by the adjacent bricks and presents smaller extent of response.

The hypothesis that the masonry model is frequency-sensitive is supported by analysis of both experimental observations and experimental data. The frequency of excitation that produces the peak amplification response is denoted as the characteristic frequency. For Model I, the characteristic frequency was found to be 1.9Hz for y-axis excitations and 2.0Hz for the x-axis. At the characteristic frequency, the out-of-plane rocking in the most integral excited portion of the wall presents the highest dominance. The steadily increasing separate brick motions occur as the frequency of excitation departs from the characteristic frequency, while the dominance and integrity of rocking reduce. A range of effective frequencies is identified alongside the characteristic frequency. Dynamic behaviour within this range does not change significantly. Clear difference can be observed between the amplifications within and beyond this range. Excitation outside the effective-frequency interval produces little structural response.

A linear force-displacement relationship in respect of out-of-plane rocking is illustrated by the hysteretic loops for both x- and y-axis excitations. The behaviour is consistent with the rocking behaviour of the rigid body, in theory. The hysteretic loops also indicate the energy dissipation in the processes of responses. This originates from the frictional forces involved in the separate motions of individual bricks, the arching effect in the middle façade and the impulsive effect at impact. This identified plastic property distinguishes the masonry model from the typical rocking of a rigid body, theoretically.

On the other hand, the integrity of Model I is largely degraded by the active rotation at corners due to lack of constraint. The out-of-plane rocking is interrupted by the separate motions of the corner bricks. Correspondingly, these errors, ignored in the analysis, indicate that the assumptions, and hence the conclusions, need further validation. The need for tests on an improved model is evident.

4.3.2 Analysis of Model II

Both the pseudo-static experiments in Chapter 3 and the shaking-table tests on Model I have illustrated that the out-of-plane rocking is the principal reason for the failure of masonry structures. However, the rocking behaviour of the façade in Model I was interrupted by the separate motion of corner bricks. To collect more complete and reliable behaviour, Model II is modified from Model I by applying 0.5kg additional load on top of each corner to constrain individual brick movements, to some extent.

As the frequency-sensitive characteristic of the masonry model has been consistently identified on Model I, only that group of excitations varying in frequency with constant peak acceleration was respectively applied in the y- and x-axes. The peak accelerations were set at 1.71mm/s^2 for x-axis excitations and 1.53mm/s^2 for the y-axis cases. These correspond to the peak accelerations applied to Model I. The frequency of excitation varies between 1.7Hz and 3.6Hz. Fifty sinusoidal cycles were applied on each test.

4.3.2.1 Observations

Maintaining the same geometric characteristics, the dynamic behaviour of Model II was consistent with that of Model I. The constant rocking portion is observed once more, being composed by two parts. The response is also effective over a range of frequencies. The out-of-plane rocking predominates more when the frequency is closer to the characteristic frequency. Meanwhile, variations generated by the extra constraints on top of corners are observed clearly. The structural integrity in the response process is improved. Integral and stable rocking is guaranteed in the whole process. All tests illustrate the reduced separate motions of corner bricks and more stable rocking on the façade. The complete response process involves no heavy failure in most tests and behaviour variations with input frequency are clearer. The behaviour presented below becomes representative of structural behaviour in the whole process.

Under y-axis excitations, the excited portion of the façade is marked by the black lines in Figures 4.24-4.27. The upper part consists of the four top layers and the adjacent bricks in the side wall. The lower part includes bricks stepping from the two edges into the fifth to eighth layers. Compared with the excited portion of Model I, smaller part of the side wall is included in the out-of-plane rocking, due to the top constraints at the corners. A more typical Mechanism B2 in the response has been generated, as shown in Figures 4.24-27(b). Smaller deformation occurs in the middle of the side wall than in Model I, which remains unchanged during the process. On the façade, only slight separate motions of the bricks occur. Its undeformed shape in the rocking deviates little from the original shape in the beginning of the response. The positions and shapes at the peak points of the façade also remain constant during the response.

With the y-axis excitation at 1.8Hz, Model II shows no effective response. The out-of-plane rocking in Figure 4.20(b) more resembles Mechanism A. No obvious damage was caused by

rocking but only slight cracks were generated at the end of the test in the side walls by in-plane sliding. The bricks in the upper part of the excited portion within the façade present slight separate sliding. A similar response was obtained with 2.0Hz excitation.

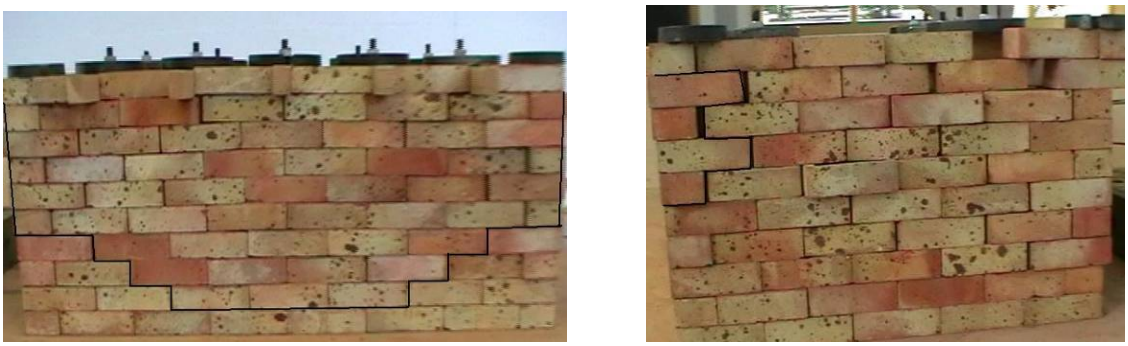

(a) (b)

Figure 4.20 The response of Model II on y-axis 1.8Hz 12mm excitation
((a) the façade; (b) the side wall)

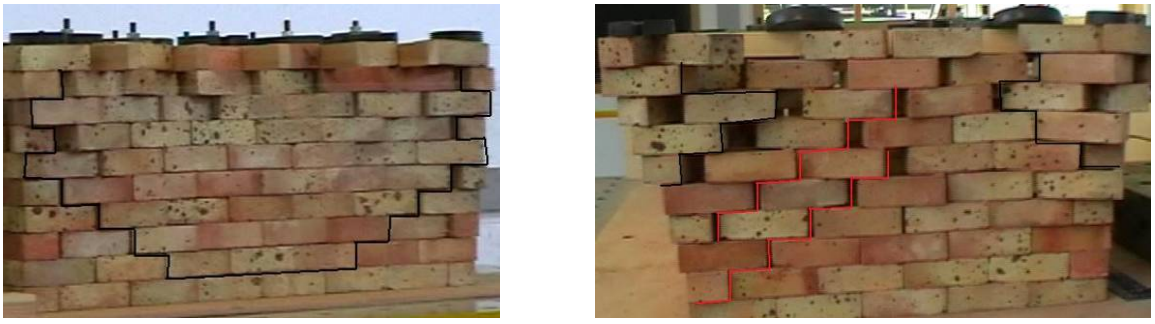

(a) (b)

Figure 4.21 The response of Model II on y-axis 2.5Hz 6.0mm excitation
((a) the façade; (b) the side wall)

At 2.5Hz, the excitation had entered the range of effective excitations. In Figure 4.21(a, b), clear rocking is shown on the part within the black line on the façade. This releases the constraint on the bricks within the side walls and induces in-plane sliding along the red lines in Figure 4.21(b). The upper part presents a little larger separate rocking than the lower part, accompanied by the separate rotation in the excited corners, as shown along the black line in Figure 4.21(b). However, larger cracks occur on the side walls due to corner rotation and sliding, while the rocking causes less damage on the façade.

3.6Hz lies beyond the effective range for Model II and the out-of-plane rocking in Figure 4.22 is greatly reduced. Only the slight sliding of bricks in the upper part is observed. Conversely, rotation at the corners completely dominates the structural response, as in Figure 4.22(a, b).

However, as the input amplitude at 3.6Hz is quite small, the limited deformation caused by the corner motion does not result in heavy damage.

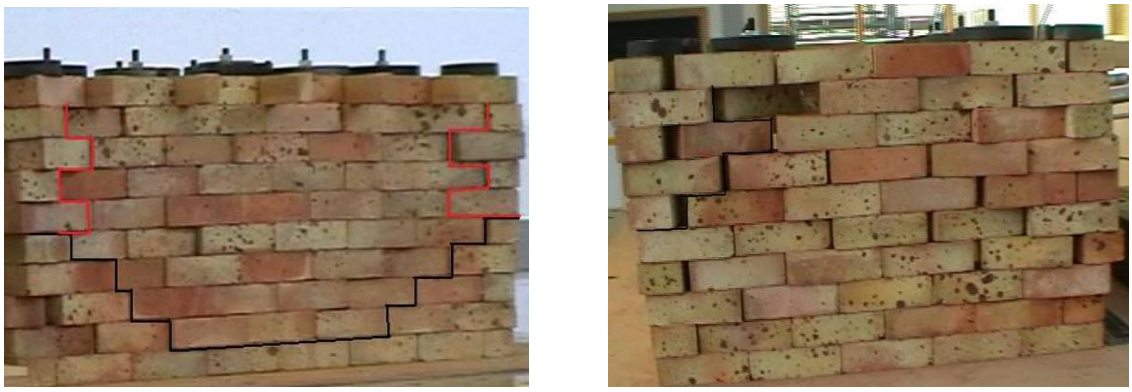

(a) (b)

Figure 4.22 The response of Model II on y-axis 3.6Hz 3.0mm excitation
((a) the façade; (b) the side wall)

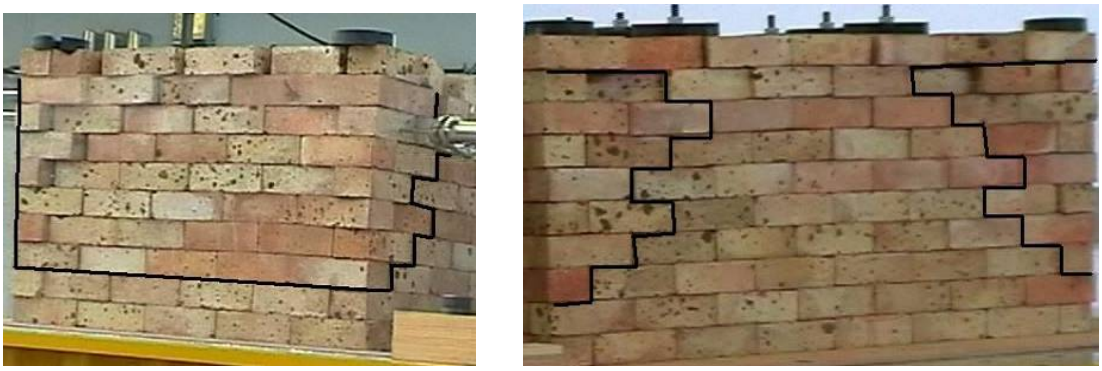

(a) (b)

Figure 4.23 The response of Model II on x-axis 1.8Hz13.37mm excitation
((a) the façade; (b) the side wall)

With the x-axis excitation, the deformation of Model II is controlled by rocking of the façade to a greater extent. The excited portion includes the whole seven layers from the top, with part of the side wall marked by the black line in Figure 4.24(b) and Figure 4.25(b). The top five layers present a little larger rocking and clearer rotation and sliding at corners, which forms the upper part. The lower part, correspondingly, contains the sixth and seventh layers, presenting smaller rocking and little rocking arch. The separate motions of bricks in the side walls have been reduced. Much smaller deformation on the side wall is shown consistently, compared with the corresponding displacements in the y-axis responses. However, the corner motions also present larger influence on the structural response of the narrower façade.

At 1.8Hz, no out-of-plane rocking is shown on the façade in Figure 4.23. Neither the in-plane sliding nor the separate motions of bricks is evident. The structural integrity is maintained well, without visible cracks, demonstrating that 1.8Hz is outside the effective range.

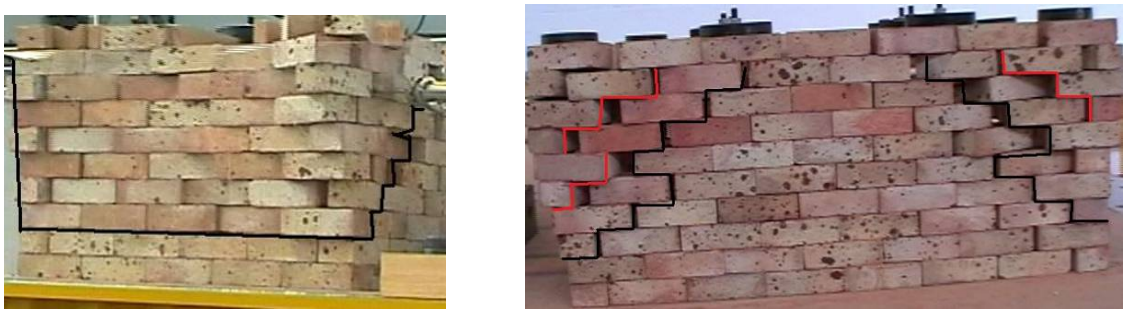

(a) (b)

Figure 4.24 The response of Model II on x-axis 2.0Hz10.83mm excitation
((a) the façade; (b) the side wall)

At 2.0Hz, the response becomes a little more evident. In Figure 4.24(a), the out-of-plane rocking becomes observable. On the excited portion within the black lines, the narrower façade rocks with the side walls synchronously. Slight separate sliding can be observed on bricks of the upper part of the excited portion. The side walls of the excited portion along the black lines in Figure 4.24(b) also presents sliding and rotation. More active rotation and sliding occur at corners along the red lines, which causes the main cracks at the end. Integrity of the façade is lost by removal of the corner constraints by rotation.

(a) the façade (b) the side wall

Figure 4.25 The response of Model II on x-axis 2.5Hz6.93mm excitation

At 2.5Hz, the more effective response is illustrated by a more pronounced rocking of the façade in Figure 4.25(a). In Figure 4.25(b), corners within the excited portion also exhibit greater out-of-plane rocking, with modest rotation. Clear displacements caused by rocking are

shown at corners of the upper part in Figure 4.25(b). The damage and final collapse are principally caused by the rocking within the excited portion. The initial separation of bricks from the model occurs on the 10th cycle. The collapse started from the top of the façade on the 16th cycle.

The differences between the dynamic behaviour for y-axis and x-axis excitations due to the different façade *L/H* ratios are shown more clearly on Model II. For the rocking in the y-axis façade with higher *L/H*, the excited rocking portions contain fewer bricks in the side walls. In addition, the façade and corners vibrate with less synchronicity, similar to Mechanism A. More separate motions and larger cracks are caused in the side walls and at corners, which also releases the integrity of the façade and activates its collapse. With x-axis excitations, bricks at the corners and side walls are better included in the out-of-plane rocking. The rocking portion maintains its integrity in most cases and the response mechanism becomes typical of Mechanism B2. Corner rotation reduces, and rocking predominates. The corner bricks display rocking, sliding and rotations, implying a high degree of vulnerability.

The consistency between the y-axis and x-axis rocking is also illustrated. The constant excited portion, composed by the upper part and the lower part, is presented. The integral rocking is presented in the excited portion. The upper part consistently shows a little extra rocking relative to the lower part, with clearer arching shape in the middle and rotation at corners.

4.3.2.2 Analysis of Experimental Data

Based on the above observations on Model II, experimental data are analysed in this section. Because of the better structural integrity in the responses compared to Model I, errors due to the separate motions of individual bricks are reduced. Conclusions can validate and improve the conclusions derived from the experiments on Model I.

The Fourier transfer was carried out as the first step for each test. The fact of a sinusoidal response was again certified. The spectrum of Model II responses shows clearly that the response frequency keeps the same with the excitation frequency. In all the tests in Figure 4.26-27, even at the excitation with high frequency such as 3.2Hz, only one peak is shown in the spectrum. This difference from the three peaks at 3.6Hz on Model I demonstrates the fewer separate brick motions on the response of Model II. Furthermore, as the excitations are based on a constant peak acceleration, the magnitude of spectrum in Figure 4.26 and Figure 4.27 also reflects the rocking magnitude. Along the y-axis, the response is relatively more effective at

2.5Hz in these four cases. Along the x-axis, the relatively effective response in these four cases occurs at 3.2Hz. These magnitudes can be compared with the rocking amplification given in the following analysis.

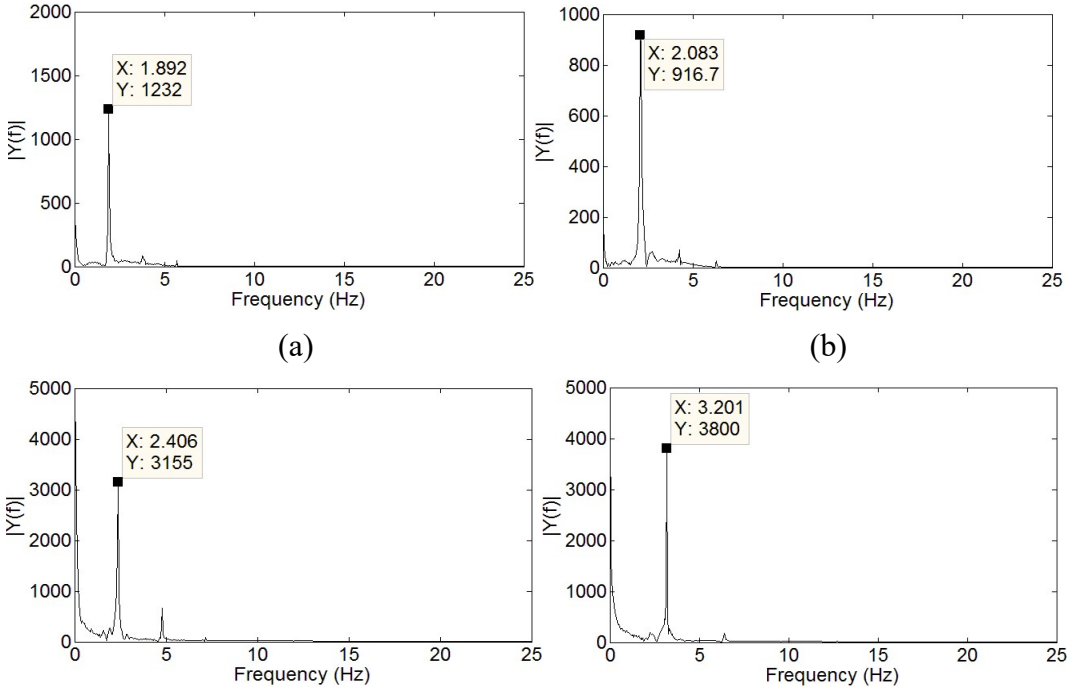

Figure 4.26 The response spectrum of the output *ds* in y-axis of Model II ((a) at 1.9Hz; (b) at 2.1Hz; (c) at 2.4Hz; (d) at 3.2Hz)

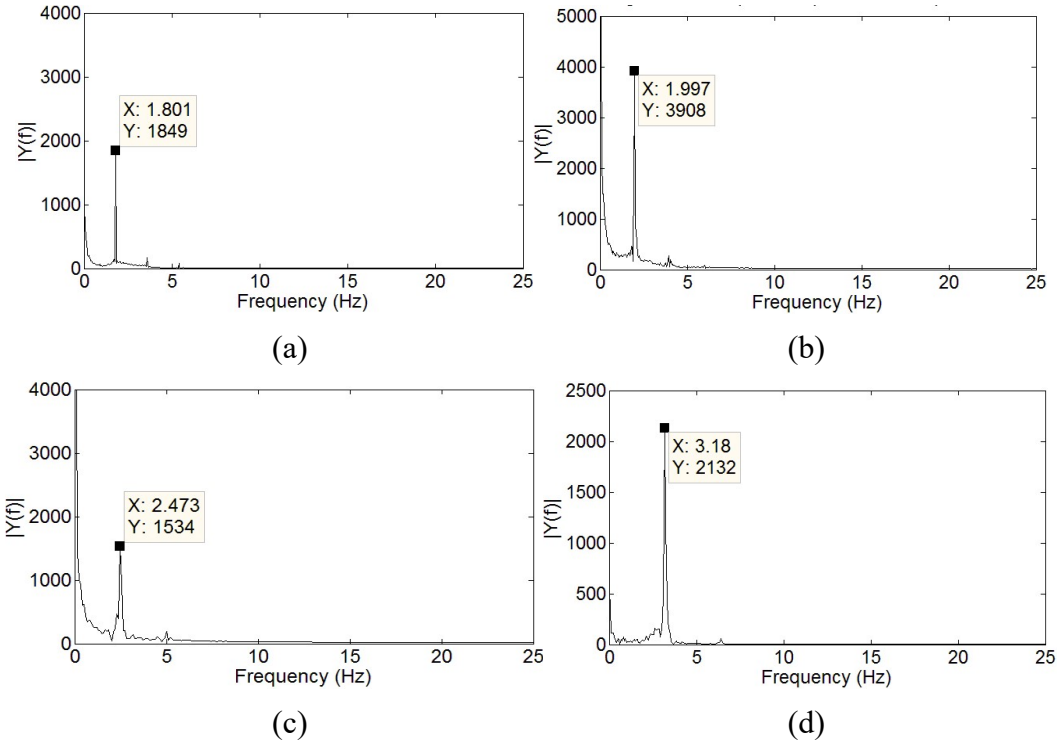

Figure 4.27 The response spectrum of the output *ds* in x-axis of Model II ((a) at 1.8Hz; (b) at 2.0Hz; (c) at 2.5Hz; (d) at 3.2Hz)

Figure 4.28 and Figure 4.29 present the hysteretic loops for the y-axis and x-axis responses of Models. Because the response remains stable throughout the whole process in each test, the hysteretic loops given include all 50 cycles of response on Model II. The y-axis hysteretic loops remain stable in the whole process consistently in Figure 4.28, indicating no reduction in structural stiffness at all response levels. These also both confirm the better structural stability and integrity due to the extra loads on the tops of corners. The responses at 1.9Hz, 2.1Hz and 3.2Hz present little energy dissipation within the loops, consistent with the little rocking observed above. The hysteretic loops at 2.8Hz in Figure 4.28(c) then show the obvious energy dissipation, indicating the effective response. The loop area for y-axis rocking of Model II at the effective response is obviously larger than the corresponding area in the loops of Model I. This illustrates the enhanced plastic property of the façade because of the additional constraints at corners.

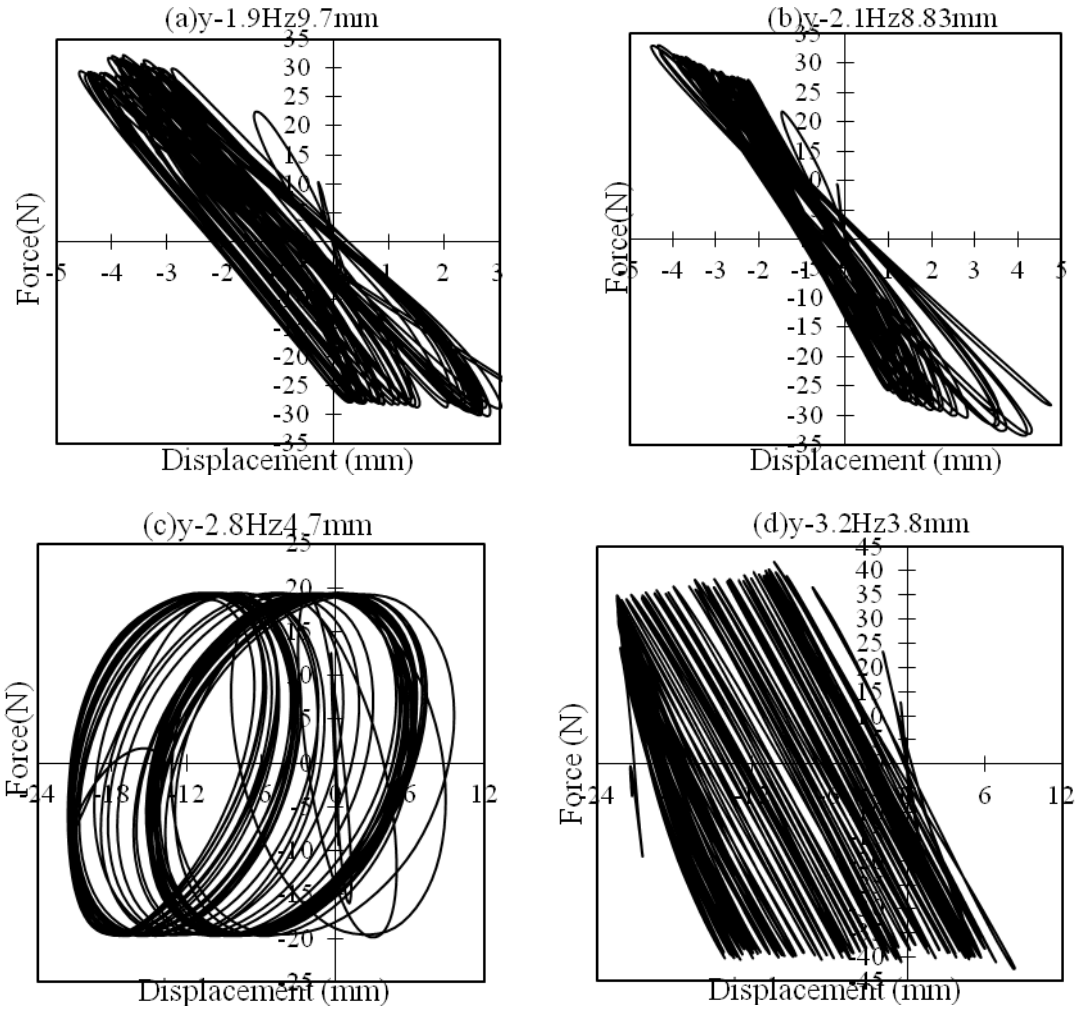

Figure 4.28 Hysteretic loops in y-axis rocking

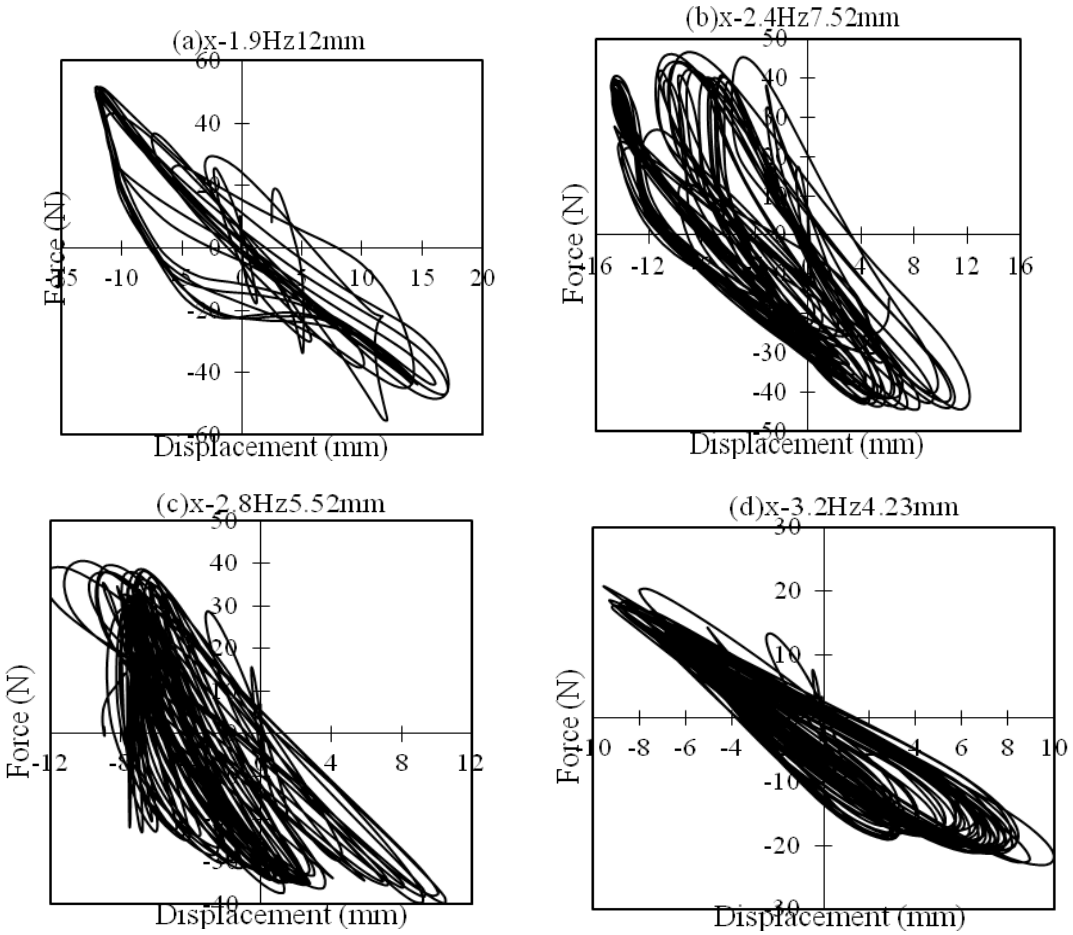

Figure 4.29 Hysteresis loops in x-axis rocking

Different hysteretic loops are shown in Figure 4.29 for the x-axis rocking of Model II. More variations on the loops are observed with the development of rocking in all four cases. Substantial variation occurs quickly in the ineffective response at 1.9Hz in Figure 4.29(a). Based on the observations, this is due to the large amount of brick separation. The gradual variations in the loops at 2.4Hz and 2.8Hz in Figure 4.31(b, c) then originate from the damage in the façade caused by the rocking. The variation of stiffness observed is caused by the continuous damage on the narrower façade observed above. Furthermore, the areas formed by the hysteretic loops for effective rocking in the x axis are unclear. This smaller energy dissipation is indicative of poorer plastic properties of façades with lower *L/H* ratios.

The out-of-plane rocking amplifications are plotted in Figure 4.30 for y-axis and in Figure 4.31 for x-axis. The quantities of *ds*, *dsr*, *a*, *ar*, *vs*, *vsr* and *va*, *var* are used. In the same test, the amplifications of these quantities consistently present similar values. The variations on amplifications of each quantity with input frequency also remain coherent. These consistencies both prove the reliability of the experimental data when using repeatedly reconstructed discrete

models. In addition, the frequency-sensitive characteristic and the existence of a characteristic frequency and an effective range of frequencies for a masonry structure are again confirmed.

In Figure 4.30, the amplification curve identifies the y-axis characteristic frequency as 2.8Hz. The clear increase in the characteristic frequency from the 1.9Hz of Model I to the 2.8Hz of Model II indicates that the extra loads on corner tops not only constrain the separate motions of bricks but also enhance the structural stiffness. All the curves for different quantities present consistently effective and ineffective ranges, with a clear gap in values of amplifications between them. Within the effective range, the amplifications vary slightly, with magnitudes around 2.0 for the directly measured *d*, *a* and *vs* and around 2.5 for the derived *va*. In the tests, 2.4Hz and 3.2Hz are included. Their relatively higher amplifications are also consistent with their higher magnitudes in the response spectrum in Figure 4.26. A clear reduction can be observed in the ineffective range when the applied frequency goes below 2.4Hz or beyond 3.2Hz, which occurs in the tests at 1.8Hz and 2.0Hz. All amplifications decrease to a level below 0.5 and vary slightly, which is also consistent with the magnitude of spectrum in Figure 4.26. Correlating with observations in the former section, the higher amplifications coincide with more dominant rocking, and the low amplifications with slight and unclear responses.

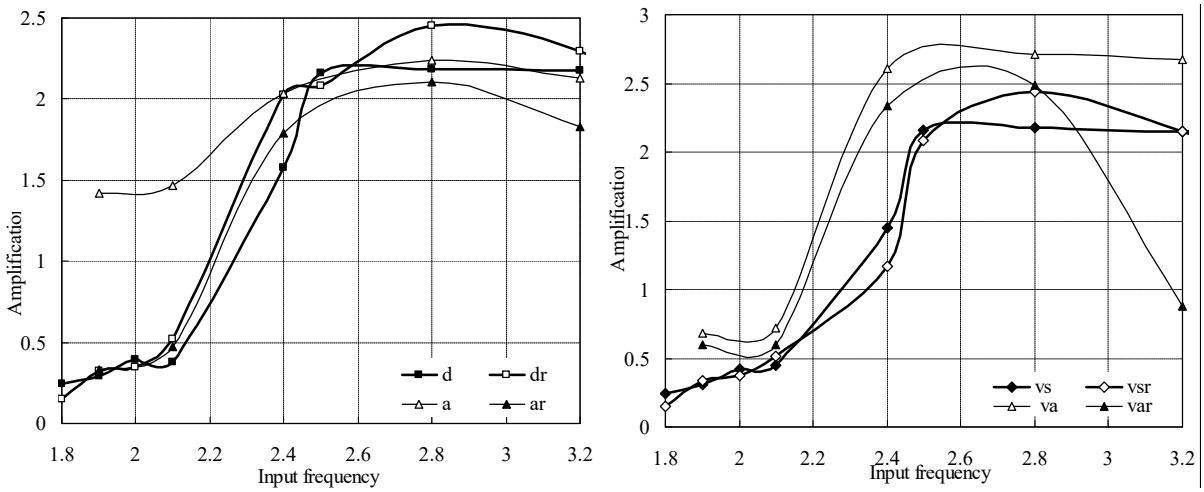

Figure 4.30 Rocking amplifications for y-axis response of Model II

Figure 4.31 gives the amplifications of these quantities for the x-axis rocking of Model II. All curves identify its x-axis characteristic frequency as 2.8Hz. The same characteristic frequency for the x-axis and y-axis façades on Model II further confirms the conclusion from Model I that the characteristic frequency is determined by the height and thickness of the façade. This is also the characteristic of a theoretical rigid body. Furthermore, a narrower effective range is presented in the x-axis response. Excitations at 2.4Hz and 2.8Hz in the series of tests generate

effective responses. In addition, the differences between the amplifications in the effective frequencies range and those outside the range are shown to be larger than in the case of y-axis excitations. Both of these illustrate the influence of *L/H* façade ratios on the dynamic characteristics. However, an inconsistency is observed at 3.2Hz. At 3.2Hz, Figure 4.27 gives a high magnitude of spectrum, but in Figure 4.31 the amplification stays at a low level as the ineffective response. Taking the clear variations of the hysteretic loops in Figure 4.29 at 3.2Hz into account, this inconsistency is, to some extent, generated by the separate motions of bricks.

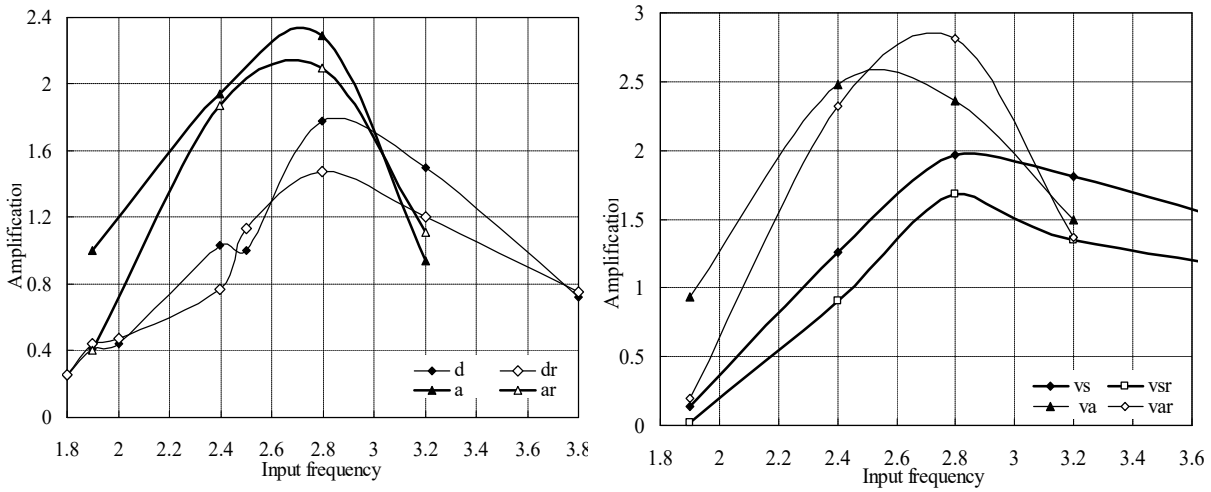

Figure 4.31 Variation of x-axis amplifications for Model II

Additionally, comparing the amplification curves from different quantities, quantities derived from accelerations such as a*, da, va, ar, dar* and *var* show higher amplifications than the others derived from displacements. This is consistent with the conclusion that dynamic parameters are more sensitive than static parameters to structural damage (Zhu and Wu. 2002). This consistency also again proves the hypothesis that the discrete masonry model presents global response as a whole. The more reliable experimental data derived from Model II are further confirmed.

The lag times between input and output of *d* and *dsr* in Model II are shown in Figure 4.32 and Figure 4.33. Similar to the behaviour of Model I, the lagging time is also divided into two groups clearly between the effective range and the ineffective range. However, compared with Model I, Model II has smaller lag times in both effective and ineffective ranges. This indicates a better synchronism between the excitation and response, which again demonstrates worse plastic rocking because of the improved corner constraint.

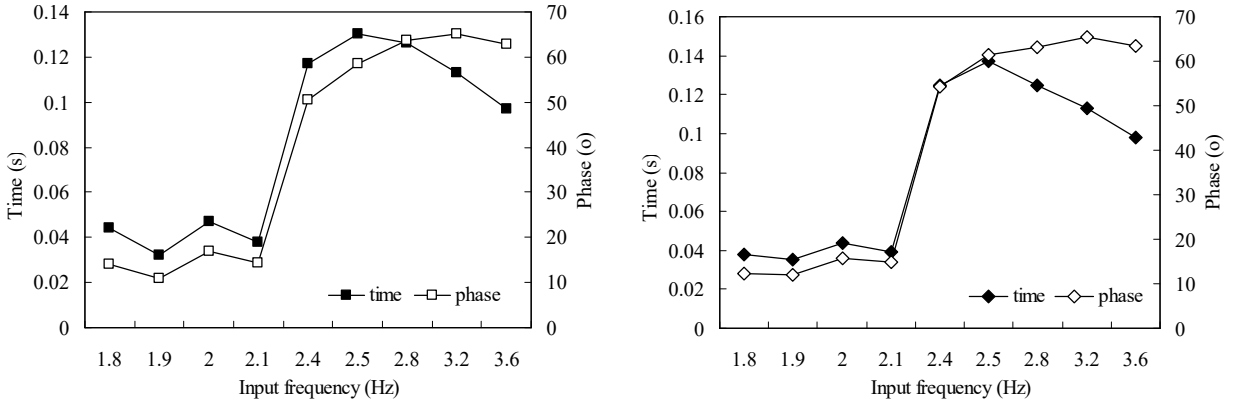

(a) (b)

Figure 4.32 Time difference of y-axis response of Model II to input displacement ((a) *d*; (b) *dsr*)

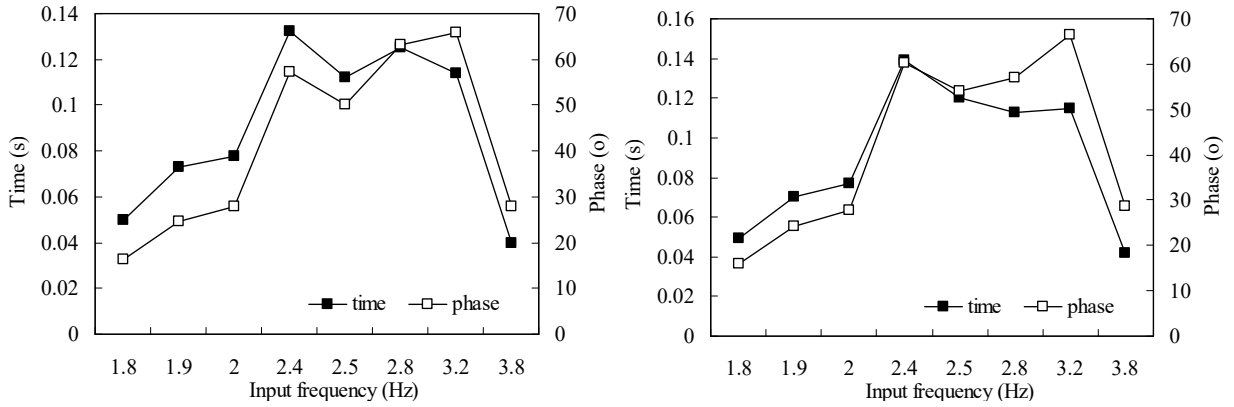

(a) (b)

Figure 4.33 Time difference of x-axis response of Model II to input displacement ((a) *d*; (b) *dsr*)

In detail, for the lagging time of Model II within each group, a constant lagging time is given, with a much higher value in the effective range. For ineffective responses, the constant lag time is 0.03s in y axis and 0.06s in x axis. It remains constant at 0.13s in both x and y axes in the effective range. This consistency indicates that the difference in excitation intensity and geometric form of the façade in x and y axes presents little influence on the lag time. It also stresses again that the dynamic characteristic of the façade depends only on its height and thickness, as a rigid body.

In essence, the above general analysis of experimental data confirms the conclusions obtained from Model I. The effect of the corner constraint in maintaining structural integrity and enhancing structural stiffness is demonstrated. Model II gives more consistent and

representative results than Model I.

As structural responses over the full 50 cycles are stable on Model II, it becomes possible to discuss in detail the structural variations during the response process. In the following, representative tests are selected. Three displacement quantities, *ds*, *dsr* and *da,* are studied, respectively, being the displacements read from transducers, relative displacements between the middle of the façade to the corner read from transducers and displacements derived from accelerations. The data of *ds* indicate the total displacement of the central brick at the top layer. The data of *dsr* represent the total relative displacement of the central brick to the corner. The data of *da* then show mostly the reciprocal motion of this brick by ignoring the initial displacement in each rocking cycle. Correspondingly, these three quantities describe different parts of the dynamic motions in the central façade at the top. Their comparison can give a clearer description of the rocking of the façade.

In the following tests being discussed, first, all quantities developed steadily with time, which guarantees the proper analysis. In addition, the variations of different quantities are also consistent with one another in all cases. The integral nature of the response of the discrete model and derivation of these quantities is validated once more. During the process of response, the amplitude of each quantity gradually continues climbing from the beginning until reaching a peak value, illustrating the impulsive effect of dynamic excitation. After that, the amplification drops to a slightly lower but more stable level. In practice, the impulsive effect causes initial cracks which enlarge in the stable stage to cause final damage.

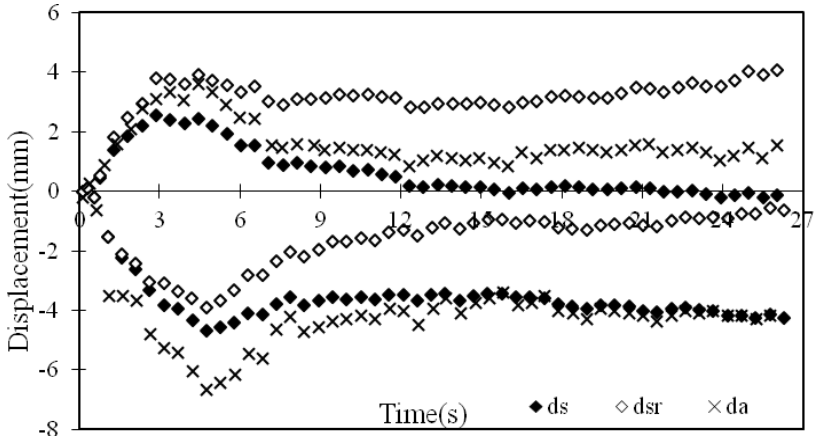

Figure 4.34 Displacements in the middle top layer at 1.9Hz10.77mm in y-axis

For y-axis responses, the test at 1.9Hz is selected to represent the ineffective response in Figure 4.34. Amplitudes of all quantities peak in the ninth cycle. The differences between the values

of the peaks and of the stable stages present the small impulsive effect for the ineffective range of response at 1.9Hz. The largest difference between amplitudes of *ds* and *da* is shown as about 1mm at the end of the response in the positive direction, while in the negative direction, the amplitudes of *ds* and *da* develop with the same value in the stable stage consistently. This indicates the small separate displacement of the central brick within the façade in the rocking process, which is also consistent with the experimental observations in the former section. Meanwhile, the deviation between the amplitudes of *dsr* and *ds* quantifies the dominantly continuous rotation of the corner bricks in the ineffective response. With about 4mm at the end, the clear separate motion at corners is even larger than the rocking in amplitude.

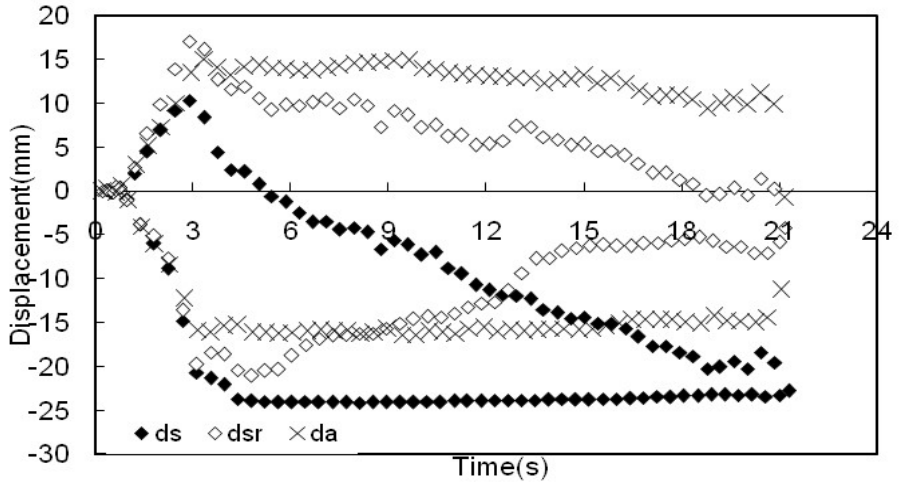

Figure 4.35 Displacements in the middle top layer at 2.4Hz6.75mm in y direction

The effective response of Model II is represented by the test at 2.4Hz. The impulsive effects occur on *ds*, *dsr* and *da* consistently earlier in the sixth cycle. Furthermore, with the decreased amplitude of excitation, larger amplitudes of *da* are shown averaged as 14.75mm in Figure 4.37. Both of these magnify the effectiveness of the response. The development of *ds* states that the continuous sliding of the central brick during rocking has caused the limited transducer range of 24mm to be exceeded in the negative direction. The development of *da* shows the rocking is less stable than in the ineffective response at 1.9Hz, which presents the more active separate motions of the central brick with this effective response. In the positive direction, the *dsr* remains parallel with *ds* consistently, presenting the constant relative positions between the central and the corner. Hence, the reduced separate corner motion and the integral rocking are demonstrated by the experimental data. The difference between the *ds* and *dsr* remains around 20mm, presenting the magnitude of the arching shape in the middle façade.

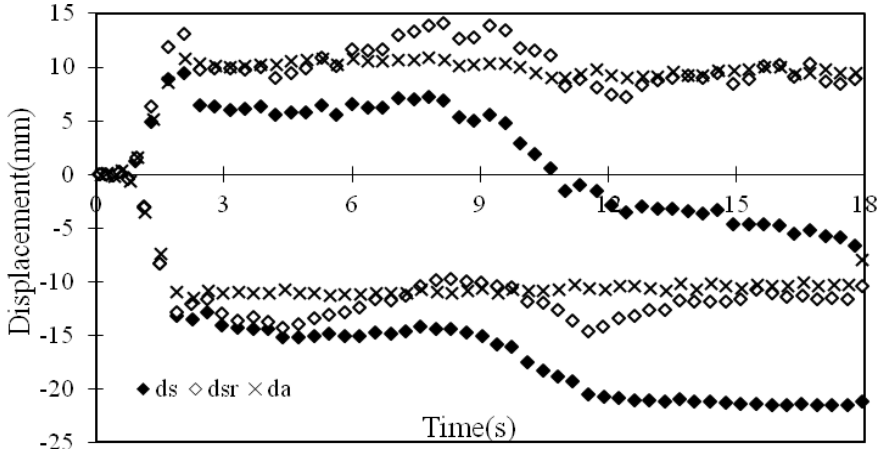

Figure 4.36 Displacements in the middle top layer at 2.8Hz 4.69mm in y direction

Figure 4.36 shows the developments of experimental data of Model II at resonance. The impulsive effect finishes in the fourth cycle, faster than the both two cases above. The amplitude then stays at the peaks as the stable stage, presenting the effective rocking response at resonance. The amplitudes of *dsr* and *da* are both more constant than in the effective response at 2.4Hz in Figure 4.35. The more stable rocking during the whole process is illustrated by these experimental data. Furthermore, *dsr* and *da* remain similar throughout the process, illustrating the small amount of sliding at corners with the stable rocking during the whole process. Meanwhile, the amplitude of *ds* presents the response process within the façade. It stays constant in the beginning and decreases moderately after 9s. Therefore, besides its stability, the effective and dominant rocking has released the constraints among bricks in the façade and activates the separate sliding of bricks in the middle. About 10mm sliding has occurred on the central brick of the façade, which is equivalent to the magnitude of global rocking.

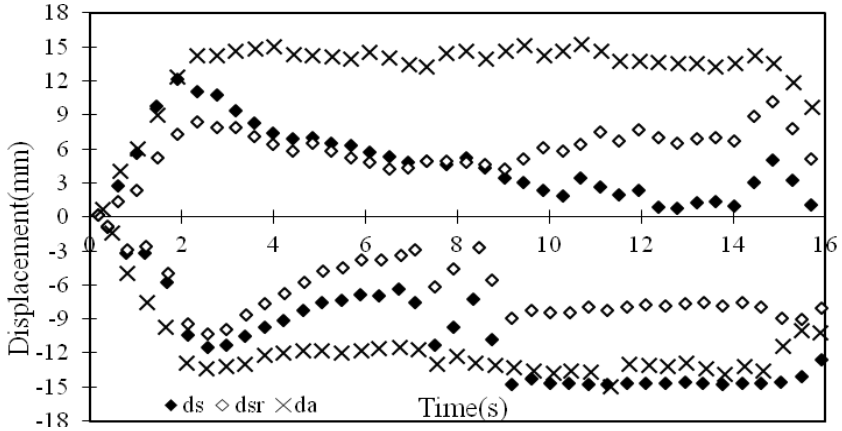

Figure 4.37 Displacements in the middle top layer at 2.4Hz 7.52mm in x-axis

The following exemplifies the tests with x-axis excitations. The effective response is represented by the test at 2.4Hz in Figure 4.39. The constant value of *da* presents the stable and integral rocking in the whole process. The effective rocking is magnified by the 15mm amplitude of *da*. The amplitudes of *da* peak in the fourth cycle and then remain constant as a stable response, clarifying the influence of the *L/H* form of the façade on its rocking characteristics. The impulsive effect can finish in a shorter time and the reduced ductility has made the rocking amplitude stay in the peak value in the stable stage. The drop in amplitude of *ds* is smaller than the case for the y-axis reduction and stops at 9s, indicating a lesser degree of sliding of bricks within the narrower façade during rocking. The *ds* and *dsr* values also achieve much smaller difference over the whole response process than in the corresponding y-axis response at 2.4Hz. This similarity between the absolute and relative displacements clarifies the integral rocking in the excited portion and the small separate motions at the corners in the narrower x-axis façade.

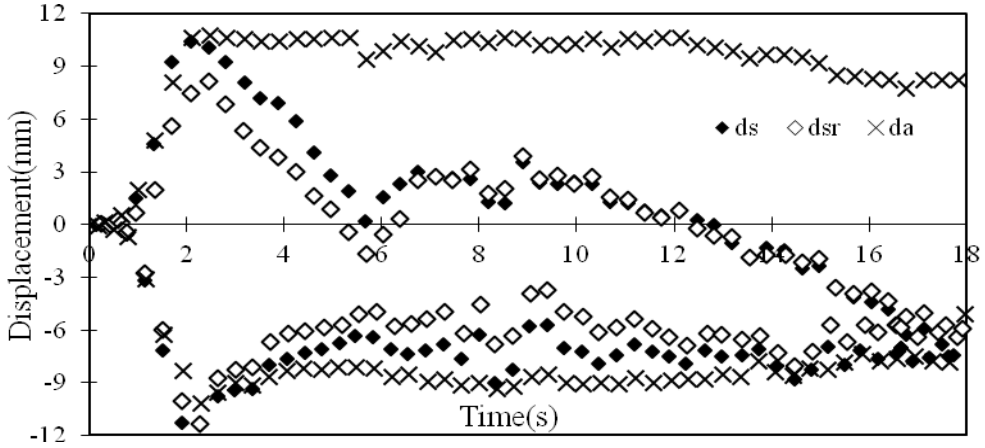

Figure 4.38 Displacements in the middle top layer at 2.8Hz5.52mm in x-axis

The development of the x-axis resonant response at 2.8Hz is shown in Figure 4.38. The peak value of *da* is reached in the fourth cycle and is maintained throughout the stable stage, to confirm the smaller impulsive effect on x-axis rocking once more. Its constancy also demonstrates the stable rocking and slight motions on individual bricks within the façade. Similar values between *ds* and *dsr* during the whole process are presented. This indicates the better integral motions in the excited portion and smaller separate motions on corner bricks at resonance. Their decrease in the positive direction then shows the continuous sliding of the central brick caused by the effective rocking response. All these characteristics are in keeping with the experimental observation that out-of-plane rocking is the predominant response of the model to a greater extent as the response gets close to resonance. Furthermore, they also offer a description of the whole process of this characteristic.

The above analysis of the whole experimental process verifies and supplements the conclusions drawn above from direct observations on the dynamic behaviour of Model II. The characteristics of the structural response are confirmed. Their developing processes during the 50 cycles are also presented. The variations of different quantities and their relationships describe the developments and characteristics of different kinds of motions with Model II during the process of response.

4.3.2.3 Experiments with Diagonal Excitations

As in practice earthquakes are unlikely to excite a structure exactly along one of the building's principal axes, a group of diagonal excitations was also applied on Model II. For that purpose, the group of excitations applied along y axis was applied along both x and y axes simultaneously of the shaking table. The inputs along each axis vary in frequency from 1.7Hz to 3.6Hz under a constant peak acceleration of 1.08mm/s^2. Since when the frequency reached 3.6Hz, the amplitude of input decreased to a very low magnitude of 3mm, no excitation with frequency higher than 3.6Hz has been applied. Formed by the sinusoidal inputs in orthogonal directions, the resultant diagonal excitation was also sinusoidal with identical frequency, but larger amplitude. Because the plan of Model II is rectangular, the direction of ultimate excitation formed by the two identical inputs along x and y axes deviates from the diagonal axis of Model II. It is actually applied on $L1$ and $L2$ eccentrically. The range of effective excitations is composed by higher frequencies. No observable response existed until the frequency had increased to 2.0Hz. The effective response range went as far as 2.5Hz.

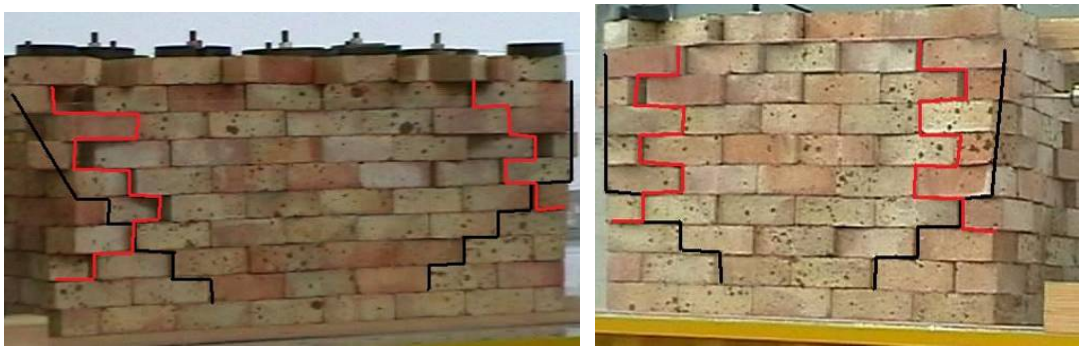

Figure 4.39 Excited portions in Model II with diagonal excitation

As the characteristic frequency was not attained in this group of tests, the response at 3.6Hz is selected to represent the typical dynamic behaviour of Model II under diagonal excitation.

Figure 4.39 shows the excited portion of Model II and its response behaviour under diagonal excitation. The influence of the interactions between the rocking of the orthogonal façades is observed. The same excited portion is observed in each axis of the façade as that which applies with single-axis excitations. Therefore, the out-of-plane rocking predominates in a larger extent on Model II. The corners rock along the diagonal direction, with large displacements being shown. Rotation and sliding, along with the rocking, are evident at corners along the red lines. The x-axis rocking on the façade with *L/H*=2.22 is smaller than the y-axis rocking on the façade with *L/H*=1.59. The x-axis rocking also gradually reduces with continuous sliding on the wall, while the y-axis rocking is more stable.

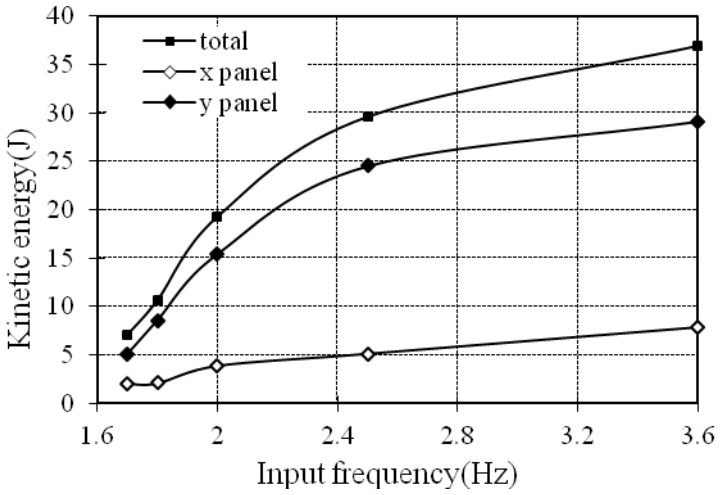

Figure 4.40 Kinetic energies of different components at compounded excitation

As the resultant excitation is not orthogonal to any of the Model II walls, the amplification of single-axis rocking is difficult to quantify and compare with the former amplifications given by the single-axis rocking. Therefore, the kinetic energy is used to quantify the magnitude of rocking. The kinetic energies for separate x- and y-axis, as well as the energy for the whole rocking of the structure, are given in Figure 4.40. The consistent variations in different components indicate all responses with the dynamic characteristics in the direction of resultant excitation. The y-axis rocking component possesses a much larger kinetic energy than the x-axis rocking. As the excited portions of the walls in the y and x directions contain 46 and 50 bricks respectively, they actually have a similar mass. Hence, this obvious difference in kinetic energies is due to the respective *L/H* ratios of 2.22 and 1.59. The out-of-plane rocking on the façades with higher *L/H* demonstrate higher ductility. The continuous increase of all these curves indicates that the characteristic frequency in the diagonal direction is higher than 3.6Hz.

4.3.2.4 Summary

The experimental behaviour and data on Model II have been analysed above. Based on the experiments, Model II with extra vertical loading on top of corners behaves dynamically in similar fashion to Model I. The constant rocking portion is observed, consistently composed by the upper part and the lower part. The same characteristics of the rocking behaviour for these two parts are obtained. The integrally global rocking of these two parts is accompanied with the extra rocking, clearer arching shape and sliding of bricks in the upper part. The frequency-sensitive characteristic is confirmed. The amplifications are divided into two groups again, with a clear gap between their magnitudes according to the frequency of excitation. The characteristic frequency of Model II is identified as 2.8Hz in both x and y axes. The effective ranges of frequencies in both directions are also identified. Similar dynamic behaviour occurs for all frequencies in the effective range. Associated with effective responses are excited portions with fewer cracks, predominant out-of-plane rocking and less separating rotations of the corners. The greatest degree of rocking dominance, together with the least corner rotation and the fewest cracks within the excited portion, occurs at the characteristic frequency.

In contrast, the effect of corner constraint is illustrated in Model II. The extra constraints on top of corners have the effect of increasing shear capacity locally and promoting box behaviour. The separate motions of individual bricks reduce effectively. A stable response was seen throughout the full 50 cycles in most experiments. The improvement in rocking capacity and the lessening in the sliding of bricks improves the seismic capacity of the masonry structure. The increased characteristic frequency of 2.8Hz for Model II illustrates an increased structural stiffness. In addition, the same characteristic frequency was found for excitations in both x and y directions for Model II. This supports the hypothesis that a masonry structure can be theoretically simplified as a rigid body whose length makes little contribution to the characteristic frequency. The out-of-plane rocking remained linear for Model II even at resonance, which supports the assumption that the model rocking can be likened to the rocking of a rigid-body system.

Based on the more stable responses of Model II, differences in the dynamic behaviour due to geometric form are illustrated. With a narrower effective range, a plastic rocking arch is less evident and energy dissipation in the x-axis façade with lower *L/H* ratios is lower. The corners and the narrower façade rock more synchronously in the x-axis excited portion with fewer cracks. The stronger interaction among bricks for x-axis rocking also generates more active sliding of the bricks in the middle of the façade. The individual corner bricks are also active.

Finally, diagonal excitations experiments reveal interactions between the x- and y-axis rocking on the orthogonal façades. The dominance of walls with higher *L/H* ratios on the response of the whole structure is demonstrated. The different characteristics of x- and y-axis rocking indicate that the influence of the arching effect needs to be taken into account in the theoretical model.

4.3.3 Analysis of Model III

The experiments on Model I and Model II have identified the characteristics of the dynamic behaviour of the masonry structure. Model III was established to study of the variation in dynamic behaviour with height.

Model III, was 15 brick layers high, which means an *L/H* ratio of 1.33 in the narrower panel for x-axis direction rocking and of 1.06 for the longer panel parallel to y-axis rocking. The geometrical plan, loading condition, corner connections and all the other structural configurations were the same as those of Model II. To allow for safety in case of bricks falling from the higher façade, lower input amplitude of 5mm was used for the set of tests with excitations along the y axis.

4.3.3.1 Observations

In the case of Model III, the rocking became observable at 2.2Hz, but an effective response did not occur until 2.4Hz. A larger constant portion was excited within the higher façade with eleven layers, as illustrated by the black line in Figure 4.41(a, b). This implies again that the excited portion depends on the geometrical property of the masonry structure. As shown in Figure 4.41(b), the corner bricks being included keep the same with the included side walls in Model II. However, the façade and the side walls rock more integrally and Mechanism B2 occurs with a clear arch from the top.

Integral rocking is presented in this excited portion, with consistently two parts being observed. The upper part consists of the complete top 6 layers. Clearer rocking is shown in the upper part, with the arching shape and observable separate sliding on bricks. The lower part includes the bricks in the following layers lying within the two stepped cracks along joint lines. The arch is not clear in this part, with little separate motion on bricks being observed. The increased height of the façade makes the rocking arch at the top of the wall clearer, even with smaller amplitude of excitation. On the other hand, the side wall principally presents sliding and rotation along the red lines in Figure 4.41(a, b). Final damage is mostly caused to the side walls due to inward

rotation of the corners.

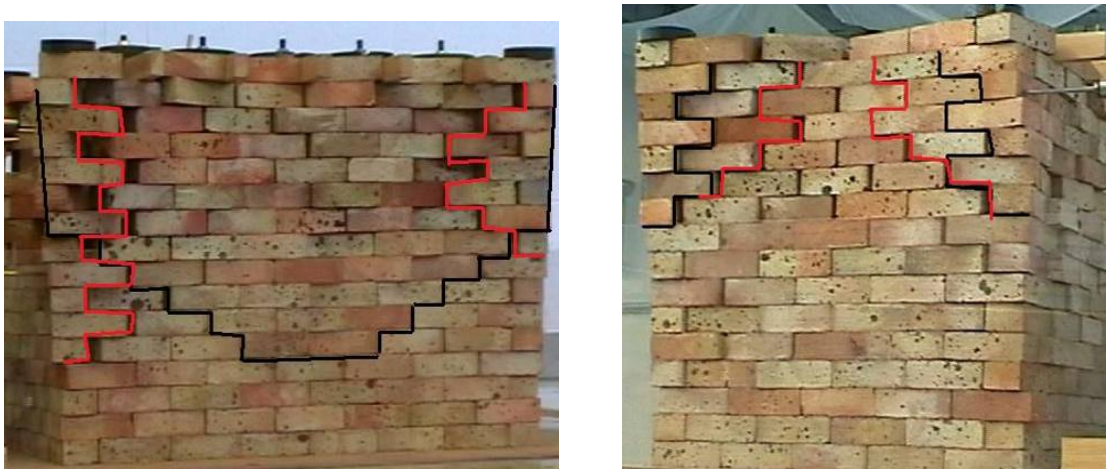

(a) (b)

Figure 4.41 Excited portions in Model III with diagonal excitation at 2.4Hz ((a) the façade; (b) the side wall)

The effective structural response of Model III at 2.4Hz is shown in Figure 4.41. Clear damage can be observed. Because of the lower *L/H* façade ratio, the y-axis dynamic behaviour of Model III is closer to the x-axis excitation behaviour of Model II. The rotation of corners remains active over a larger portion along the red lines in Figure 4.41. The interaction among bricks shows a larger influence than the case for Model II. It is the corner rotation that dominates the global behaviour of Model III, while the influence of out-of-plane rocking is reduced to a much lower level. The motions at corners generate clear deformation in the middle of the side wall in Figure 4.41(b), even larger than the out-of-plane rocking arch.

4.3.3.2 Analysis of Experimental Data

With the decrease of the amplitudes of excitations to prevent the falling of bricks on Model III, the reduced intensity of excitation offers smaller and stable responses. In Figure 4.42(a-d), similar hysteretic loops are presented at both effective and ineffective excitations. No clear energy dissipation can be observed in any of the cases, which indicates a lower plastic capacity of the higher façade. It also confirms the observations in Figure 4.41 that the dominance of rocking has reduced on Model III. No reduction in structural stiffness can be observed in any of the cases, indicating the good structural integrity of Model III during response in all cases. Hence, the active rotation at corners in the observation does not interrupt the global rocking. A linear response to the excitation is well maintained with Model III, again supporting the hypothesis that a masonry façade can be theoretically treated as a rigid-body system.

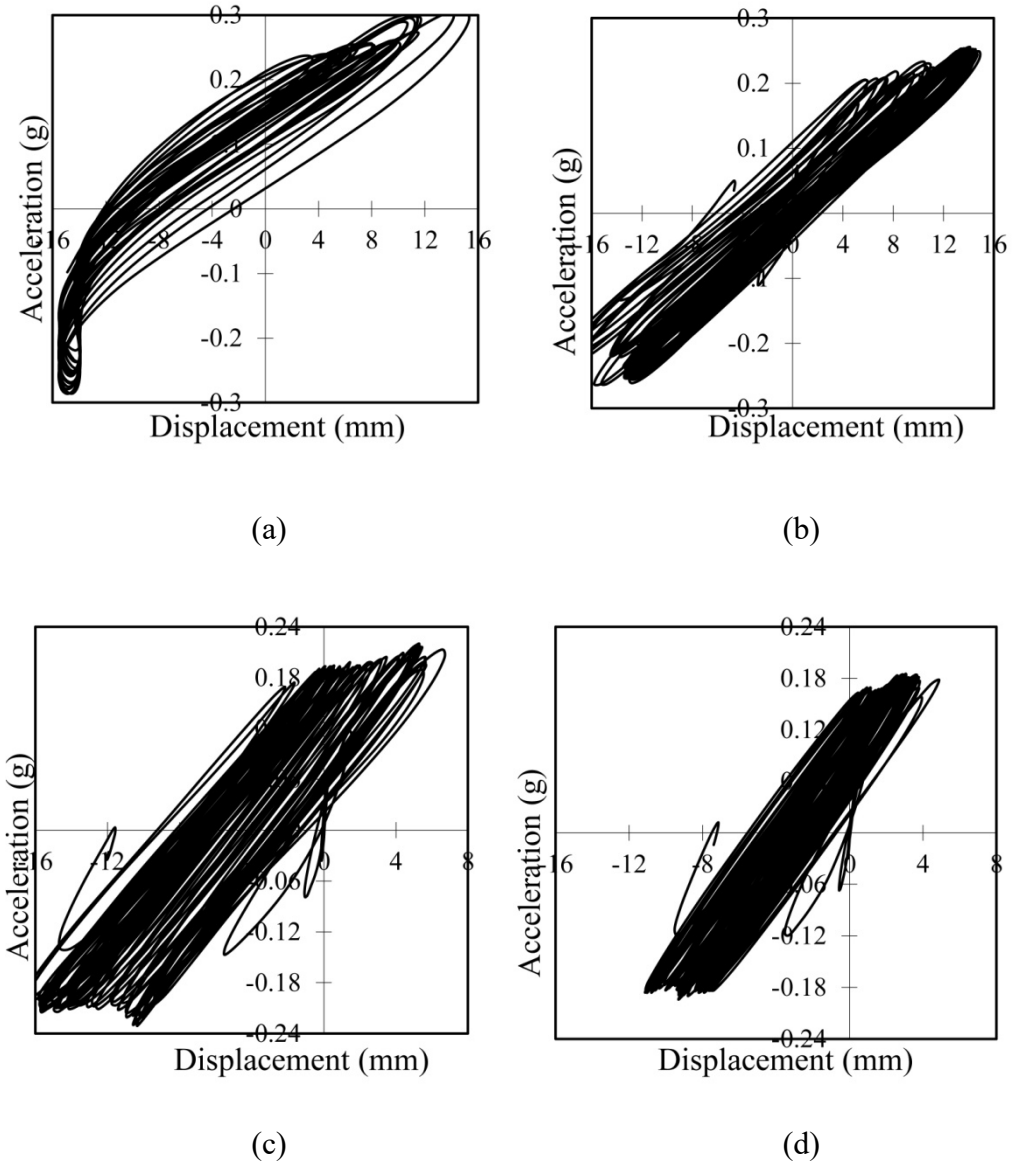

Figure 4.42 Hysteretic loops of y-axis rocking on Model III
((a) 1.7Hz; (b) 2.2Hz; (c) 2.8Hz; (d) 3.2Hz)

Correlate with increase in height of the façade on Model III, the characteristic frequency decreases to 2.4Hz, shown by the variations of amplifications of *ds* in Figure 4.43. The effective range of frequencies becomes quite narrow and includes only 2.4Hz and 2.5Hz in the tests, with the amplifications around 3.5. The amplifications mainly reduce to 2.0 when frequencies deviate from this rang to 2.0Hz, 2.2Hz, 2.8Hz and 3.2Hz. This supports the Model II conclusion that the façade with lower *L/H* is associated with a narrower effective range. Meanwhile, the amplifications for both effective range and ineffective range of Model III are

higher than the corresponding amplifications of Model II. This, together with the observed clearer rocking arch, indicates the increased vulnerability of higher façades.

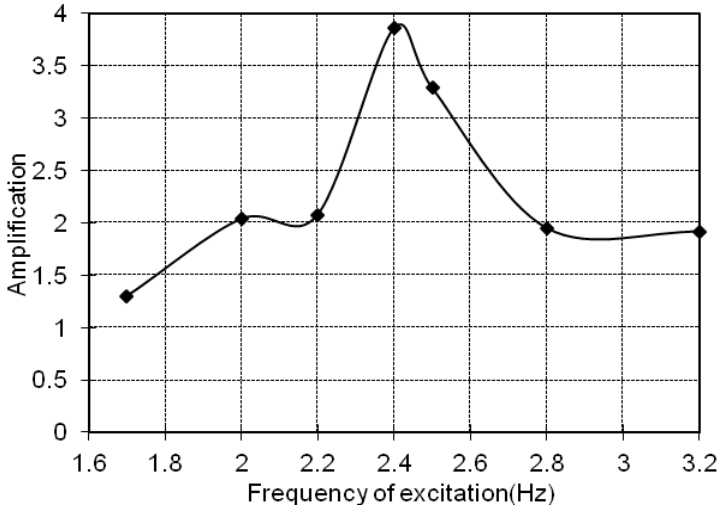

Figure 4.43 Amplifications of rocking in y direction on Model III

The out-of-plane rocking on the top layer of the façade has been discussed in relation to the different *L/H* ratios on Model I and Model II. On Model III, the vertical deformation of the façade is also discussed. For that purpose, the maximum vertical deformations at the eighth layer and 15th layer of the façade are plotted with height in Figure 4.44. The vertical shapes of the walls when the central façade reaches its maximum displacements in both the negative and positive directions are drawn. Two response cycles, with one in the ninth cycle at the start and the other at the end of the stable stage in the 33rd cycle, are shown. Taken into account the efficient and integral rocking in the stable stage of resonant response, the deformed curve of 2.4Hz is more representative of the vertical deformed shape of façade in Model III. Furthermore, the drawn vertical deformations depict the mode of the response.

On the façade, the vertical deformed shape of the façade remains basically consistent from the start to the end in Figure 4.44(b), presenting the stable rocking in the whole process. When the façade rocks to its peak point, the deformation increases with the height and the maximum displacement occurs at the top layer. Slight nonlinearity is shown by Figure 4.44(b), with a little extra displacement shown on the top. Obviously, this kind of nonlinear property is unlike that of a single-rigid-body system. This confirms the experimental observations from Model I, II and III that the excited portion is divided into two rigid parts and the upper part presents slight separate rocking to generate larger displacements and clearer arching shape. Therefore, theoretical study of the out-of-plane rocking of a masonry façade with a two-rigid-body system

is supported.

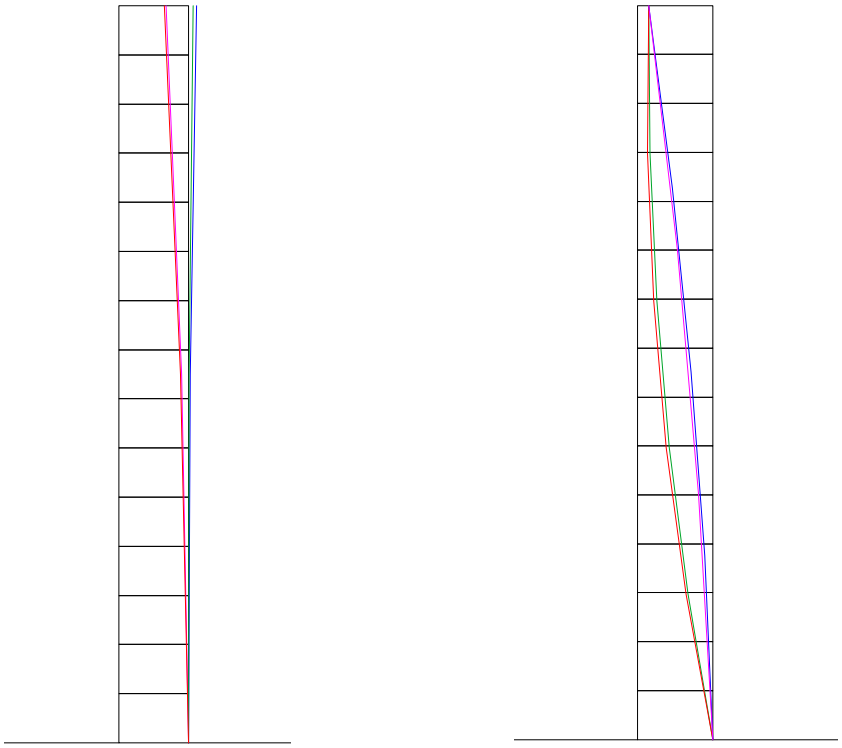

Figure 4.44 Vertical Deformation of Model III along height on Model III

(positive peak in the beginning negative peak in the beginning positive peak by the end negative peak by the end)

Within one cycle, the vertical shape of the side wall has little variation, with basically unchanged position and shape. However, by comparing the beginning with the end of the response process, continuously increased displacements are observed in the middle layer, which indicates the continuous rotation from the middle of the side wall. The lower extent of deformation at the top layer is due to the extra constraints on top of corners. The relatively clearer deformed curve on the side wall again indicates the higher dominance of corner rotation for Model III responses.

4.3.3.3 Summary

The study of Model III further supports and supplements the conclusions drawn from Model I and Model II experiments. Firstly, the predominated out-of-plane rocking and the accompanied separate corner rotations are observed consistently. Secondly, the excited portion which presents integral rocking and contains two parts is confirmed. The characteristics of the upper

and lower parts are demonstrated, which supports the theoretical modelling in Chapter 5. Thirdly, a "characteristic frequency" also exists for Model III. The characteristic frequency and the effective frequency range have been identified. Consistent variations of the structural response with the frequency of excitation have been obtained.

In contrast, some of the response characteristics illustrate the influence of model height on dynamic behaviour. First, there is a reduction of characteristic frequency from 2.8Hz to 2.4Hz with increase of model height, indicating that the model behaves as a rigid-body system. Secondly, for Model III, the out-of-plane rocking reduces and corner rotation increases its dominance. The decreased vulnerability of the corners in models with higher *L/H* ratios is stated. The façade top is also seen to be more vulnerable to failure by excessive displacement in spite of the low amplitude of excitation. The fact that discrete models in this series of tests nevertheless display the characteristics of rigid bodies is further demonstrated.

4.3.4 Analysis of Experimental Error

There could be several sources of error in this experimental program, such as the discrete nature of the models in the repeated reconstruction, the shaking-table system itself, the data acquisition system and the influence of technical personnel.

For example, the discrete nature of the three models generates errors. In all experiments, the two parallel façades rock in the out-of-plane directions with different magnitudes. Here *L*1 1 and *T*1 that were close to the actuators in the y and x directions are defined as the back wall and *L*2 and *T*2 on the other side are defined as the front wall.

It is shown in Table 4.9-Table 4.11 that back walls rock with higher amplifications than the front walls. The amplification ratio between front and back wall is constant in each table. For Model II, the average ratios are 0.359 for y-axis rocking and 0.618 for x-axis rocking. For the y-axis rocking of Model III, the ratio averages 0.587. The constant ratio within each group of experiments irrespective of input frequency indicates attenuation rate depends only on the characteristics of the model. The large decrease in the rocking of the front façades suggests that the input excitation may be reduced by the motions of the side walls, thereby lessening the impact on the front walls. The discrete property of the dry masonry model is the reason for the different responses of the front and back façades.

Table 4.9 Amplifications of back and front façade for y-axis excitation Model II

Input frequency	Front wall	Back wall	ratio
2.1 Hz	0.716	1.469	0.487
2.4 Hz	0.671	2.034	0.330
2.8 Hz	0.549	2.120	0.259

Table 4.10 Amplifications of back and front façade for x-axis excitation Model II

Input frequency	Front wall	Back wall	ratio
2.4 Hz	1.295	1.940	0.668
2.8 Hz	1.152	1.823	0.632
3.2 Hz	0.520	0.936	0.556

Table 4.11 Amplifications of back and front façade for y-axis excitation Model III

Input frequency	Front wall	Back wall	ratio
1.7 Hz	1.479	2.512	0.589
2.0 Hz	1.421	2.388	0.596
2.2 Hz	1.329	2.266	0.587
2.8 Hz	1.210	2.127	0.569
3.2 Hz	1.109	1.867	0.595

Additionally, with respect to earlier shaking-table experimental studies (Fujita, Furuya et al. 2000), errors have been mentioned. It has been observed from on-site earthquakes that the influence of excitation amplitude on dynamic characteristics becomes greater with increase of intensity of the earthquake. Of course, the shaking-table experiments cannot properly simulate the interaction between soil and structure. However, conclusions on the structural response mechanisms and the principles governing how those responses vary based on this experimental program have been shown to be valid.

4.4 Conclusions

The three 1/10-scale dry masonry models-Model I, II and III all behave in a similar manner to one another and respond similarly to excitations varying in frequencies or amplitudes. The reliability of the experimental data is proved. Conclusions on the dynamic behaviour of masonry walls can be derived as follows.

Generally, the masonry models exhibit out-of-plane rocking in the form of Mechanism B2 on the excited portions, with different degrees of separate sliding and rotations of bricks. The excited portions remain the same and constant for each model irrespective of the excitations applied. With increase of *L/H* façade ratio, predominance of the out-of-plane rocking increases and corner rotation increases in influence. It is found that the separate motions of individual bricks do not alter the global rocking nature of the model. Nevertheless, a high degree of seismic vulnerability at corners is evident and the necessity for corner constraint has been demonstrated. The out-of-plane rocking is mostly shown to be plastic in nature. Façades with higher *L/H* ratios exhibit plastic characteristics and ductility to a greater extent and are able to better sustain damage when subject to dynamic excitation.

The constant excited portions, as rigid-body systems, present integral rocking behaviour, which dominants the global response of the masonry models. Meanwhile, they are consistently divided into two parts based on the structural configurations. The upper part contains all the bricks in the several top layers, with part of the side walls. The lower part contains bricks in the following layers but within the two stepped joint lines from the edges to the middle. The upper part shows a little extra rocking with additional displacement and clearer arching shape. The lower part is better constrained by the adjacent bricks and presents smaller extent of rocking and unclear arching shape. This is illustrated by both the experimental observations and the vertical deformation of Model III, and can be the basis of the mathematical model of the theoretical study in Chapter 5.

The discrete models are proved to be frequency-sensitive. A characteristic frequency and a certain effective range of frequencies spreading around it are found to exist for all three models in each direction. Façades with lower *L/H* ratios have narrower effective ranges and larger differences between the effective and ineffective responses. As input frequency deviates from the characteristic frequency, the dominance of rocking reduces and corner rotation becomes more active. Clear responses are barely generated by frequencies outside the effective range.

The characteristic frequency is shown to depend little on the length of the façade, indicating that the façade can be mathematically modelled as a rigid-body system. The nonlinearity of the vertical deformed shapes of walls means that a wall should not be modelled as a single rigid body but rather as a multi-rigid-body system. These also provide experimental support for the theoretical study below on the dynamic behaviour of the masonry structure.

Chapter 5 A Mathematical Model of the Out-of-plane Rocking of Masonry Structure

5.1 Background

It is common practice in structural engineering to assume deformable continuum behaviour when dealing with structures under dynamic excitation. However, for masonry structures, their rigid response and poorer ability to release energy suggests that a model of rigid bodies with relative motion allowed between them might be a more suitable model.

The rigid body is defined as a solid that can translate and rotate but cannot change shape. The rigid-body model generally assumes that the body does not deform while in motion and that it makes instantaneous contact with any exterior boundary (Stewart 2000). Rocking, sticking, slipping, bouncing and rotating are all possible motions of a rigid body. Allowing for the possibility of the simultaneous existence of some of these motions, the response pattern of one single rigid body can take various forms. When studying the one-rigid-body model, most current investigations are based on restrictive assumptions. Housner's landmark study (Housner 1963) on the single slender rigid block has provided basic understanding of the rocking response in the dynamic phase.

On this basis, mathematical studies have provided many descriptions of the dynamic behaviour of the masonry façade. Most dynamic approaches to the seismic behaviour of a rigid-body model have focused on the largely simplified nonlinear equations which are suitable for describing single unanchored objects and large monuments. Patterns of rigid body motions when subjected to horizontal and vertical excitations have been classified by Shenton (1996) as sliding, rocking and the slide-rock mode. Ishiyama (1983) identified six types of motion (rest, slide, rotation, slide rotation, translation jump and rotation jump). Gilbert (2002) identified five possible mechanisms for an unreinforced masonry wall subjected to out-of-plane impact loading. Some other researches also formulated the criteria for initiation (Scalia and Sumbatyan 1996, Pompei, Scalia et al. 1998).

However, the inherent nonlinear properties of block rocking necessitated the adoption of non-linear system models. Allen and Duan (1995) found that the nonlinear model does give more robust results, even in the case of the simple slender block. Also, because of its highly nonlinear nature, the initial response pattern of a rigid body can vary even for a given excitation and is by nature a stochastic problem (Yim, C.-S., Chopra et al. 1980, Koh and Spanos 1986, Hogan 1990, Giannini and Masiani 1991, Lenci and Rega 2006). In addition, the transition from one pattern to another is a nonlinear behaviour. This, for a one-rigid-body model, includes mathematical descriptions of the transition itself, the impact that causes transition and the impulsive effect of that impact. The impact dynamics between a rigid body and the ground have been identified to be nonlinear by Hogan (1990). Impact and its nonlinearity are stated as being important influences on the patterns of response as well as on conditions initiating motion (Yim, C. S. and Lin 1991, Sinopoli 1997).

In summary, the mathematical study of dynamic rocking of the masonry walls can be based on the dynamics of rigid body. The slenderness of the wall and the corresponding nonlinearity in motion, impact and transition should be taken into account. A series of assumptions and hypotheses according to the usual practice are necessary to simplify the model. The dynamic behaviour of assemblies of blocks has not been studied sufficiently because of the complexity of the problem. Psycharis (1990) studied a model consisting of two stacked rigid blocks without sliding. Spanos et al. (2001) later developed this study to a model with two general rigid blocks.

5.2 Introduction

This thesis focuses on the post-crack dynamic behaviour of the masonry walls. As it has been identified that the mortar has little effect on the damage mechanism of the masonry structure after the crack occurs, dry masonry model can be representative. Both the global rocking and the separate motions of bricks can be on the basis of the rigid-body dynamics.

In the pseudo-static experiments described in Chapter 3, out-of-plane collapse of the façade has been demonstrated to be more vulnerable to the masonry structure. Mechanism A for the façade without wings and Mechanism B2 for the façade with wings are found to be the mechanism most likely to cause damage. The theoretical description based on rigid-body limit analysis has been validated. The out-of-plane rocking is also observed to be the dominant

response behaviour in the masonry models from the shaking-table experiments in Chapter 4. Both the experimental observation and the analysis of the experimental data support the rigid rocking in two parts in the masonry model.

Based on the observations in the shaking-table experiments in Chapter 4, a constant portion within the façade is excited to rock on each façade at different excitations. It is divided into two parts based on the structural configurations, which present some differences in responding behaviour. In the upper part, all bricks in each layer are included, with also part of the side walls. In the lower part, the portion being excited reduces from the two edges to the middle symmetrically along the joints as the layer develops to the bottom. During the response, the upper and lower parts usually rock integrally as one portion. However, the upper part presents additionally separate rocking to induce larger displacement on the top. The vertical deformation of Model III also presents the additional deformation on the top of the façade, as two rigid bodies.

Therefore, in this study, the theoretical model consisting of two stacked rigid bodies, with one on top of the other, is set up. The top load and constraints are included. The possible rocking pattern and the transitions between them are formulated. The nonlinearity is taken into account. The impact is defined to be inelastic. The behaviour of the masonry façade is simplified to a large extent. Sliding and rotation, which have considerable effects on the dynamic behaviour of masonry structures, are ignored. The assumptions and hypotheses cannot be well fulfilled. Therefore, the theoretical model is expected to describe only some characteristics of the experimental rocking. The magnitude of rocking is expected to be described with acceptable errors. The integral and separate rocking mechanisms of the excited portion within the façade in the shaking-table tests are expected to be simulated. The influences of different parameters on the rocking behaviour of the rigid-body theoretical model will be discussed.

It has been stated that even for the simplest two-block assemblies, the rocking problem becomes very complex (Spanos, Roussis et al. 2001). Simultaneous rocking and either sliding or rotating will produce many more possible patterns. The equations of motions and transitions will become quite complicated, with extremely high nonlinearities. Each motion needs considerable work for a proper mathematical description.

5.3 The Theoretical Model

A model of two stacked rigid bodies subjected to ground excitation is shown in Figure 5.1. Consistent with the input excitations in the pseudo-static and shaking-table tests in Chapter 3 and Chapter 4, only horizontal excitations are considered in this model. The basic assumptions are as follows. The only possible response when subjected to a base excitation is rocking about the block corners. The friction between the top layer and the beams remains as sliding friction. There are rigid foundations, enough friction to prevent sliding and point contact during the impact. The impact of the two parts is assumed to be inelastic. There is no loss of contact between the object and the base at any time. These two rigid bodies may rock either as one integral system or separately with either corner as the joint point. The load on top of the façade is marked as a compression force *N*, with the frictional force on the top marked as *F*.

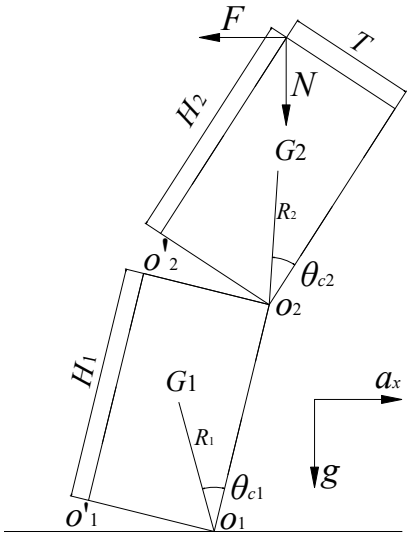

Figure 5.1 The theoretical model on out-of-plane rocking of masonry façade

The top body representing the portion above the crack is named as Part 2 and the body representing the portion below the crack is Part 1. In the equations of motion, the index i=1 denotes Part 1 and i=2 denotes Part 2. The thickness and height of each part are marked respectively as T_i and H_i. The right-hand points of the bodies are O_i and the left are O'_i , and the centre of gravity of each part is G_i. The distance from O_i to G_i is denoted by R_i. The angle between the vertical and the edge of the block is θ_{ci}. The model possesses two degrees of freedom, θ_1 denoting the rocking angle of Part 1 with respect to the ground and θ_2 denoting the rocking angle of Part 2 with respect to Part 1. Each part of this model has mass m_i and moments of inertia with respect to rocking reference points at corners I_{oi}. The model is

assumed to be homogeneous, with the total mass defined as M. Thus, the centre of mass of each part is at the centre of gravity. If I_{c1} and I_{c2} are the mass moments of inertia of the two blocks with respect to their centre of gravities, one can write:

$$I_{oi} = I_{ci} + m_i R_i^{\,2}, (i = 1,2) \tag{5-1}$$

$$I_o = I_{c1} + I_{c2} + MR^2 \tag{5-2}$$

Subjected to base excitations, the model exhibits three possible patterns of rocking in terms of the relative position between Part 1 and Part 2, each of which is subdivided into two subcases depending on the points of rocking, as shown in Figure 5.2. Pattern 1 and Pattern 2 present 2-DOF system which responds with the two parts rocking in the same or opposite directions. Pattern 3 reflects a SDOF response with Part 1 and Part 2 rocking as one rigid block.

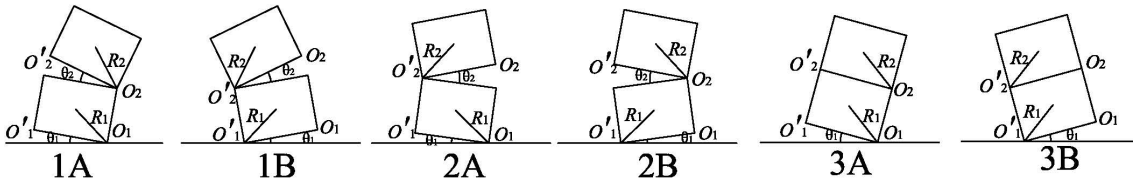

Figure 5.2 Possible patterns of rocking response of the model

5.4 Formulation

The rocking behaviour is expressed by dynamic equations in this section. The rocking behaviour of the model is discontinuous, and is interrupted by the impact behaviour of either part when its rocking angle becomes zero. Different oscillations of the discontinuous rocking in different patterns are connected by impact. The impact is defined as being inelastic and the energy dissipation by the impulsive effect is described by a restitution coefficient γ. Through formulating the impact behaviour, the post-impact velocities in the next oscillation of rocking can be determined.

The nonlinearity in the rocking behaviour is taken into account in equations of motion. The high nonlinearity in the differential equations demonstrates that the analytical solutions are impossible and only the numerical results can be obtained. It also greatly enhances the difficulties in getting reliable solutions.

The magnitude of the compression force N is the gravity of the total mass loaded on each façade in Chapter 4, which is 58.8N. Based on the experimental observation, it is assumed that the relative motion between the beams and the bricks of the top layer always exists. Therefore, F is a sliding frictional force as $F = \mu N$. As the coefficient of friction obtained from the experiments in Chapter 3 is 0.81, the magnitude of F is 47.63N. Its direction is always opposite to the direction of the velocity of Part 2. In the following equations of motions, it is represented by a function "sign" which is 1 if the velocity of Part 2 is positive, -1 if it is negative, and 0 if the velocity becomes zero.

5.4.1 Initiation of motion

Before describing the rocking by the equations of motion, the appropriate criteria for initiating the motion should be clarified. Subjected to a horizontal excitation a_x at the base, as shown in Figure 5.3, the rocking is defined as beginning from Pattern 3 when the overturning moment provided by the horizontal inertia force about one edge exceeds the corresponding vertical restoring moment generated by the gravitational force, the compression force and the frictional force. This means:

$$\left|\frac{1}{2}Ma_xH\right| > \frac{1}{2}(Mg + N)T + \mu NH \tag{5-3}$$

Therefore, the criterion for the initiating motion from rest to Pattern 3A is

$$-a_x > \frac{T}{H}\left(g + \frac{N}{M}\right) + \frac{2\mu N}{M}, \tag{5-4}$$

and the criterion for motion initiation from rest to Pattern 3B is

$$a_x > \frac{T}{H}\left(g + \frac{N}{M}\right) + \frac{2\mu N}{M} \tag{5-5}$$

where T is the thickness of the masonry wall and H is its total height.

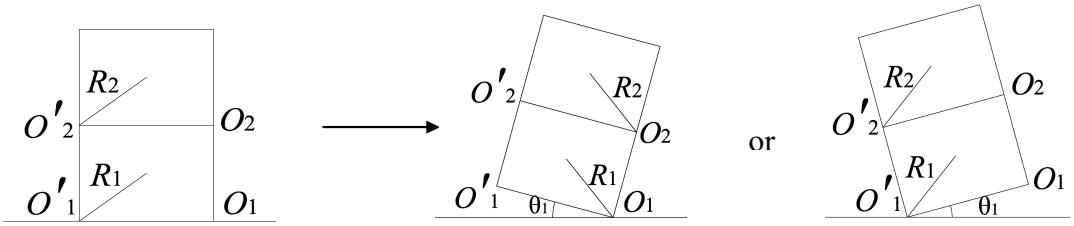

Figure 5.3 Initiation of motion

Therefore, with sliding between the ground and the model and among the rigid bodies being

ignored, the initial rocking is determined by the geometric ratio and the magnitude of acceleration of excitation.

5.4.2 Dynamic equations of motion

With two parts in the excited portion of the façade, the model contains two parts and theoretically has two degrees of freedom. Therefore, two equations are required for each pattern motion to obtain solutions. To derive the equations of motion, Newton's second law is applied on the model and on Part 2 separately. The balanced angular moments in opposite directions are given in these two equations.

In the first equation on the global motion of the model, the motion of Part 2 with respect to its local reference point (O_2 or $O_2^{'}$) needs to be transformed to absolute motion relative to the global reference point (O_1 or $O_1^{'}$). To achieve this, the angular momentum of Part 2 with reference to its local coordinates is first transformed to the global coordinate system with reference point O_1 or $O_1^{'}$. For Pattern 1, the angular momentum of Part 2 relative to O_1 or $O_1^{'}$ is:

$$\begin{aligned} L_0 &= \int \left(\vec{H}_1 + \vec{r}\right) \times \left(\dot{\vec{\theta}}_1 \times \vec{H}_1 + \dot{\vec{\theta}}_2 \times \vec{r}\right) dm \\ &= \vec{H}_1 \times \left(\dot{\vec{\theta}}_1 \times \vec{H}_1\right) + \int \vec{H}_1 \times \left(\dot{\vec{\theta}}_2 \times \vec{r}\right) dm + \vec{R}_2 \times \left(\dot{\vec{\theta}}_1 \times \vec{H}_1\right) + \int \vec{r} \times \left(\dot{\vec{\theta}}_2 \times \vec{r}\right) dm \\ &= H_1^2 \dot{\theta_1} + H_1 R_2 \dot{\theta_1} \cos(\theta_{c2} - \theta_2) + H_1 R_2 \dot{\theta_2} \cos(\theta_{c2} - \theta_2) + I_2 \dot{\theta}_2 \end{aligned} \tag{5-6}$$

For Pattern 2, it is:

$$\begin{aligned} L_0 &= \int \left(2\vec{R}_1 + \vec{r}\right) \times \left(\dot{\vec{\theta}}_1 \times 2\vec{R}_1 + \left(-\dot{\vec{\theta}}_2\right) \times \vec{r}\right) dm \\ &= 2\vec{R}_1 \times \left(\dot{\vec{\theta}}_1 \times 2\vec{R}_1\right) + 2\vec{R}_1 \times \left(-\dot{\vec{\theta}}_2 \times \vec{R}_2\right) + \vec{R}_2 \times \left(\dot{\vec{\theta}}_1 \times 2\vec{R}_1\right) + \int \vec{r} \times \left(-\dot{\vec{\theta}}_2 \times \vec{r}\right) dm \\ &= 4R_1^2 \dot{\theta_1} + 2R_1 R_2 \left(-\dot{\vec{\theta}}_2\right)(-\cos(\theta_{c1} + \theta_{c2} - \theta_2)) - 2R_1 R_2 \dot{\theta_1}(-\cos(\theta_{c1} + \theta_{c2} - \theta_2)) - I_2(-\dot{\theta}_2) \\ &= 4R_1^2 \dot{\theta_1} + 2R_1 R_2 (\dot{\theta}_1 + \dot{\theta}_2) \cos(\theta_{c1} + \theta_{c2} - \theta_2) + I_2 \dot{\theta}_2 \end{aligned} \tag{5-7}$$

The angular moment is then the first order differentiation of angular momentum to time:

$$M_o = \frac{dL_o}{dt} \tag{5-8}$$

In respect of the second equation, for Part 2, compatibility of the internal force of Part 1 acting on Part 2 should be taken into account. The equations which govern the motion of the model in each pattern are derived from Newton's second law, as follows.

For Pattern 1A:

$$\begin{cases} I_1\ddot{\theta}_1 + m_2H_1^2\ddot{\theta}_1 + m_2H_1R_1\left(\ddot{\theta}_1+\ddot{\theta}_2\right)\cos(\theta_{c2}-\theta_2) + I_1\ddot{\theta}_2 + m_1gR_1\sin(\theta_{c1}-\theta_1) \\ +m_2g(R_2\sin(\theta_{c2}-\theta_1-\theta_2) - H_1\sin\theta_1) - \mu N(H_1\cos\theta_1 + 2R_2\cos(\theta_{c2}-\theta_1-\theta_2))\cdot\mathrm{sign}\left(\dot{\theta}_2\right) \\ +N(2R_2\sin(\theta_{c2}-\theta_1-\theta_2) - H_1\sin\theta_1) + m_1a_xR_1\cos(\theta_{c2}-\theta_1) \\ +m_2a_x(R_2\cos(\theta_{c2}-\theta_1-\theta_1) + H_1\cos\theta_1) = 0 \end{cases} \quad (5\text{-}9a)$$

$$\begin{cases} I_2\ddot{\theta}_2 + m_2gR_2\sin(\theta_{c2}-\theta_1-\theta_2) - m_2H_1\dot{\theta}_1^2R_2\cos(\theta_{c1}-\theta_{c2}+\theta_2) + \\ +m_2H_1R_2\ddot{\theta}_1\sin(\theta_{c1}-\theta_{c2}+\theta_2) - 2\mu NR_2\cos(\theta_{c2}-\theta_1-\theta_2)\cdot\mathrm{sign}\left(\dot{\theta}_2\right) \\ +2R_2N\sin(\theta_{c2}-\theta_1-\theta_2) + m_2a_xR_2\sin(\theta_{c2}-\theta_1-\theta_2) = 0 \end{cases} \quad (5\text{-}9b)$$

For Pattern 1B:

$$\begin{cases} I_1\ddot{\theta}_1 + m_2H_1^2\ddot{\theta}_1 + m_2H_1R_1\left(\ddot{\theta}_1+\ddot{\theta}_2\right)\cos(\theta_{c2}-\theta_2) + I_2\ddot{\theta}_2 + m_1gR_1\sin(\theta_{c1}-\theta_1) \\ m_2g(2R_1\sin(\theta_{c1}-\theta_1) - R_2\sin(\theta_{c2}+\theta_1-\theta_2)) + 2N(R_1\sin(\theta_{c2}-\theta_1) - R_2\sin(\theta_{c2}-\theta_1+\theta_2)) \\ +N(2R_2\sin(\theta_{c2}-\theta_1-\theta_2) - H_1\sin\theta_1) - m_1a_xR_1\cos(\theta_{c2}-\theta_1) \\ -m_2a_x(R_2\cos(\theta_{c2}-\theta_1-\theta_2) + H_1\cos\theta_1) = 0 \end{cases} \quad (5\text{-}10a)$$

$$\begin{cases} I_2\ddot{\theta}_2 + m_2gR_2\sin(\theta_{c2}-\theta_1-\theta_2) - m_2H_1\dot{\theta}_1^2R_2\cos(\theta_{c1}-\theta_{c2}+\theta_2) + \\ +m_2H_1R_2\ddot{\theta}_1\sin(\theta_{c1}-\theta_{c2}+\theta_2) - 2\mu NR_2\cos(\theta_{c2}-\theta_1-\theta_2)\cdot\mathrm{sign}\left(\dot{\theta}_2\right) \\ +2R_2N\sin(\theta_{c2}-\theta_1-\theta_2) - m_2a_xR_2\sin(\theta_{c2}-\theta_1-\theta_2) = 0 \end{cases} \quad (5\text{-}10b)$$

For Pattern 2A

$$\begin{cases} I_1\ddot{\theta}_1 + 4R_1^2m_2\ddot{\theta}_1 + 2R_1R_2m_2\left(\ddot{\theta}_1+\ddot{\theta}_2\right)\cos(\theta_{c1}+\theta_{c2}-\theta_2) + I_2\ddot{\theta}_2 + m_1gR_1\sin(\theta_{c1}-\theta_1) + \\ m_2g(2R_1\sin(\theta_{c1}-\theta_1) - R_1\sin(\theta_{c2}+\theta_1-\theta_2)) + 2N(R_1\sin(\theta_{c2}-\theta_1) - R_2\sin(\theta_{c2}-\theta_1+\theta_2)) \\ -2\mu N(R_1\cos(\theta_{c1}-\theta_1) + R_2\cos(\theta_{c2}-\theta_1+\theta_2))\cdot\mathrm{sign}\left(\dot{\theta}_2\right) + m_1a_xR_1\cos(\theta_{c1}-\theta_1) \\ +m_2a_x(R_2\cos(\theta_{c2}+\theta_1-\theta_2) + 2R_1\cos(\theta_{c1}-\theta_1)) = 0 \end{cases} \quad (5\text{-}11a)$$

$$\begin{cases} I_2\ddot{\theta}_2 - m_2gR_2\sin(\theta_{c2}+\theta_1-\theta_2) + 2m_2R_1R_2\dot{\theta}_1^2\sin(\theta_{c1}+\theta_{c2}-\theta_2) - \\ +2m_2R_1R_2\ddot{\theta}_1\cos(\theta_{c1}+\theta_{c2}-\theta_2) - 2\mu NR_2\cos(\theta_{c2}+\theta_1-\theta_2)\cdot\mathrm{sign}\left(\dot{\theta}_2\right) \\ +2R_2N\sin(\theta_{c2}+\theta_1-\theta_2) + m_2a_xR_2\sin(\theta_{c2}+\theta_1-\theta_2) = 0 \end{cases} \quad (5\text{-}11b)$$

For Pattern 2B:

$$\begin{cases} I_1\ddot{\theta}_1 + 4R_1^2 m_2\ddot{\theta}_1 + 2R_1R_2m_2\left(\ddot{\theta}_1+\ddot{\theta}_2\right)\cos(\theta_{c1}+\theta_{c2}-\theta_2) + I_2\ddot{\theta}_2 + m_1gR_1\sin(\theta_{c1}-\theta_1) + \\ m_2g(2R_1\sin(\theta_{c1}-\theta_1) - R_2\sin(\theta_{c2}+\theta_1-\theta_2)) + 2N(R_1\sin(\theta_{c2}-\theta_1) - R_2\sin(\theta_{c2}+\theta_1-\theta_2)) \\ -2\mu N(R_1\cos(\theta_{c1}-\theta_1) + R_2\cos(\theta_{c2}-\theta_1+\theta_2))\cdot\mathrm{sign}\left(\dot{\theta}_2\right) - m_1a_xR_1\cos(\theta_{c1}-\theta_1) \\ -m_2a_x(R_2\cos(\theta_{c2}+\theta_1-\theta_2) + 2R_1\cos(\theta_{c1}-\theta_1)) = 0 \end{cases} \quad (5\text{-}12a)$$

$$\begin{cases} I_2\ddot{\theta}_2 - m_2gR_2\sin(\theta_{c2}+\theta_1-\theta_2) + 2m_2R_1R_2\dot{\theta}_1^2\sin(\theta_{c1}+\theta_{c2}-\theta_2) - \\ +2m_2R_1R_2\ddot{\theta}_1\cos(\theta_{c1}+\theta_{c2}-\theta_2) - 2\mu NR_2\cos(\theta_{c2}+\theta_1-\theta_2)\cdot\mathrm{sign}\left(\dot{\theta}_2\right) \\ -2R_2N\sin(\theta_{c2}+\theta_1-\theta_2) - m_2a_xR_2\sin(\theta_{c2}+\theta_1-\theta_2) = 0 \end{cases} \quad (5\text{-}12b)$$

For Pattern 3A:

$$I\ddot{\theta} + Mg\sin(\theta_c-\theta) - \mu N(H\cos\theta + T\sin\theta)\cdot\mathrm{sign}\left(\dot{\theta}\right) + N(T\cos\theta - H\sin\theta) + Ma_xR\cos(\theta_c-\theta) = 0 \quad (5\text{-}13)$$

For Pattern 3B:

$$I\ddot{\theta} + Mg\sin(\theta_c-\theta) - \mu N(H\cos\theta + T\sin\theta)\cdot\mathrm{sign}\left(\dot{\theta}\right) + N(T\cos\theta - H\sin\theta) - Ma_xR\cos(\theta_c-\theta) = 0 \quad (5\text{-}14)$$

According to the high nonlinearities of the equations of motions derived above, for each pattern of motions, the analytic solutions cannot be derived. Only the arithmetic solutions can be available at given conditions. This also makes arithmetic analysis on the sensitivities of the rocking behaviour to different structural and input parameters impossible. However, it can be observed from the equations for each pattern that the rocking behaviour of the model is inherently determined by its own *H/T* ratio (*R* and θ_c) and varies with the characteristics of the acceleration of excitation. The nonlinearity is also induced by the *H/T* ratio.

5.4.3 Transitions without impact

After the model is initiated to rock as Pattern 3, it may either stay in that same pattern or transit to another pattern with the changes in velocities. The transition between different patterns can be caused either by an impact or by a change in ground excitation without any impact. The transitions without impact are studied in this section, while the transitions caused by an impact of Part 1 with the ground or an impact between Part 2 and Part 1 will be examined in the next section.

The Pattern 3 motion can switch to Pattern 1 or Pattern 2 without impact on either part. The transition occurs when the overturning moment on Part 2 based on either of its reference point

becomes larger than the corresponding restoring moment. The criteria for transitions from Pattern 3 to Pattern 1 and Pattern 2 in the absence of impact are as follows.

Pattern 3A→Pattern 1A (Pattern 3B→Pattern 1B):

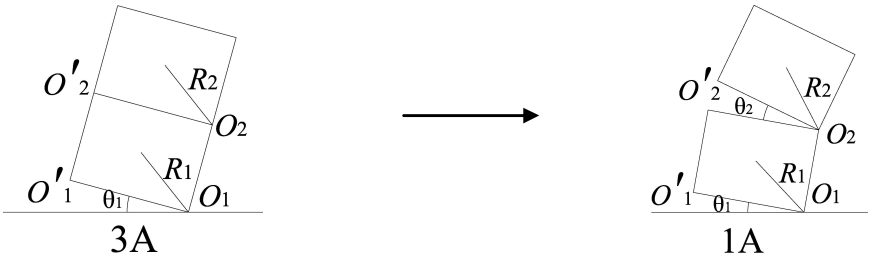

Figure 5.4 Transition from Pattern 3A to Pattern 1A

Transition from Pattern 3A to Pattern 1A occurs, based on the reference point O_2, as shown in Figure 5.4. This transition requires that

$$\mathrm{m_2 a_x \sin(\theta_{c2}-\theta) + I_2\ddot{\theta} + m_2 g \sin(\theta_{c2}-\theta) - m_2 H_1 \dot{\theta}^2 R_2 \cos(\theta_{c1}-\theta_{c2}) + m_2 H_1 R_2 \ddot{\theta} \sin(\theta_{c1}-\theta_{c2}) - 2\mu N R_2 \cos(\theta_{c2}-\theta)\cdot \mathrm{sign}(\dot{\theta}) + 2N R_2 \sin(\theta_{c2}-\theta) \le 0} \quad (5\text{-}13)$$

Hence, the critical input acceleration a_c to make this transition is

$$\mathrm{a_{c1}} = \begin{bmatrix} \frac{2\mu N}{m_2} R_2 \cos(\theta_{c2}-\theta)\cdot \mathrm{sign}(\dot{\theta}) + H_1 \dot{\theta}^2 R_2 \cos(\theta_{c2}-\theta) - \frac{I_2 \ddot{\theta}}{m_2} \\ -gR_2 \sin(\theta_{c2}-\theta) - \frac{2N}{m} R_2 \sin(\theta_{c2}-\theta) - H_1 R_2 \ddot{\theta} \sin(\theta_{c1}-\theta_{c2}) \end{bmatrix} / (R_2 \sin(\theta_{c2}-\theta)) \quad (5\text{-}14)$$

In order to make the transition from Pattern 3A to Pattern 1A, the input acceleration should satisfy the following criteria:

$$|a_x| \le |a_{c1}| \quad (5\text{-}15)$$

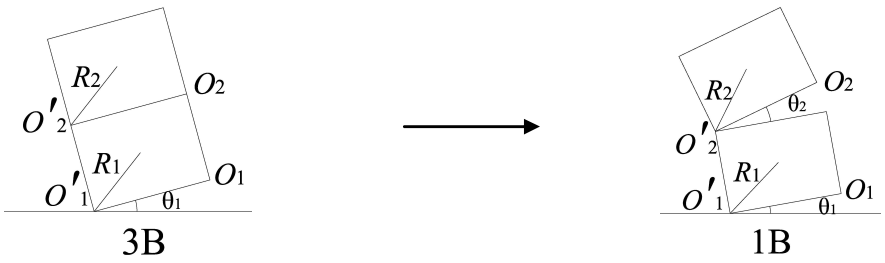

Figure 5.5 Transition from Pattern 3B to Pattern 1B

Transition from Pattern 3B to Pattern 1B is shown in Figure 5.5. Considering the symmetric

characteristics of the model and its rocking behaviour, the transition condition as Eq. 5.15 and the critical acceleration as Eq. 5.14 are also applicable to this transition.

Pattern 3A→Pattern 2A (Pattern 3B→Pattern 2B):

Transition from Pattern 3A to Pattern 2A is shown in Figure 5.6.

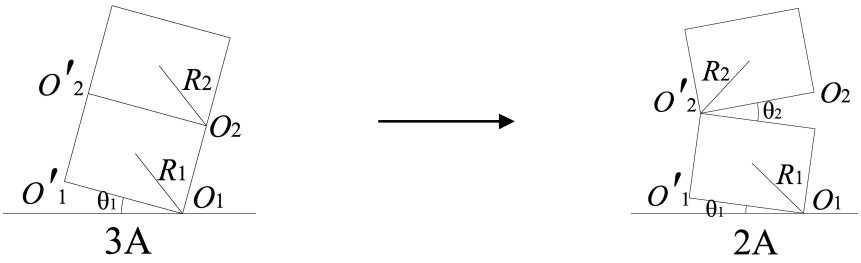

Figure 5.6 Transition from Pattern 3A to Pattern 2A

This requires that

$$|m_2 a_x R_2 \sin(\theta_{c2}+\theta)| + I_2\ddot{\theta} - m_2 g \sin(\theta_{c2}+\theta) + 2m_2 H_1 \dot{\theta}^2 R_1 R_2 \cos(\theta_{c1}+\theta_{c2}) \\ -2m_2 \ddot{\theta} R_1 R_2 \sin(\theta_{c1}+\theta_{c2}) - 2\mu N R_2 \cos(\theta_{c2}+\theta)\cdot \mathrm{sign}(\dot{\theta}) - 2N R_2 \sin(\theta_{c2}+\theta) \geq 0 \quad (5\text{-}16)$$

Hence, the critical acceleration a_c to make this transition is

$$a_{c2} = \left[\begin{array}{c} -\frac{I_{o2}\ddot{\theta}}{m_2 R_2} + \frac{2\mu N}{m_2} R_2 \cos(\theta_{c2}+\theta)\cdot \mathrm{sign}(\dot{\theta}) + \\ \frac{2N}{m_2} R_2 \sin(\theta_{c2}+\theta) - 2R_1\dot{\theta}^2 \cos(\theta_{c2}+\theta) + 2R_1\ddot{\theta}\sin(\theta_{c2}+\theta) \end{array} \right] / \cos(\theta_{c2}+\theta) \quad (5\text{-}17)$$

In order to make the transition from Pattern 3A to Pattern 1A, the input acceleration should satisfy the following criterion:

$$|a_x| \geq |a_{c2}| \quad (5\text{-}18)$$

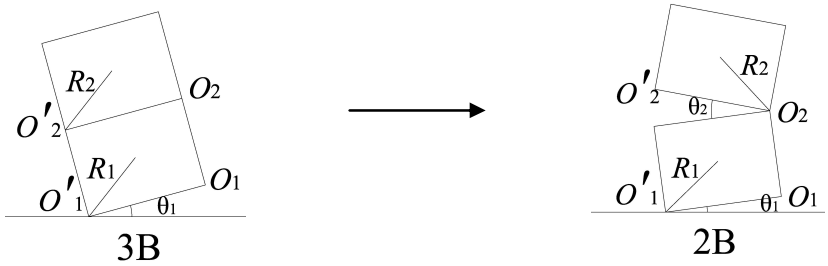

Figure 5.7 Transition from Pattern 3B to Pattern 2B

Transition from Pattern 3B to Pattern 2B is shown in Figure 5.7. Eq.(5-17) and Eq.(5-18) can also be used to justify this type of transition because of symmetry of the model.

5.4.4 Transitions with impact

Transitions due to impact can occur when the model rocks as Pattern 1 or Pattern 2. The impact that initiates the transitions of rocking patterns may occur either between Part 1 and Part 2 or between Part 1 and the rigid base.

Based on the assumptions in this model, the only possible response is pure rocking and point-impact. The assumption of impulsive impact in an infinitesimal time interval is applicable, implying negligible changes in position and orientation and instantaneous changes in angular velocity. Therefore position changes of the bodies are negligible and only their velocities change instantaneously. In this regard, only impulsive force can cause discontinuous changes of angular velocities. The impact behaviour can be described, using the theories of impulse and conservation of momentum. The impulse is assumed to be typically inelastic with no bouncing.

The corresponding energy dissipation at impact without sliding motion is constant and depends on object shape. In the literature, the energy dissipation is often characterised by the restitution coefficient. The restitution coefficient is used as(Yim, C.-S., Chopra et al. 1980):

$$\gamma = 1 - \frac{3}{2}\sin^2\theta_{ci} \tag{5-19}$$

When $\theta_1 = 0, \theta_2 \neq 0$, the impact between Part 1 and the rigid base occurs, as shown in Figure 5.8. In this case, the restitution coefficient is

$$\gamma_1 = 1 - \frac{3}{2}\sin^2\theta_{c1} \tag{5-20}$$

The post-impact angular velocity of Part 1 as $\dot{\theta}'$ is determined by γ_1 and the angular velocity before the impact $\dot{\theta}$

$$\dot{\theta}' = \gamma\dot{\theta} \tag{5-21}$$

Based on the conservation of momentum:

$$m_1\dot{\theta}_1 + m_2\dot{\theta}_2 = m_1\dot{\theta}_1{}' + m_2\dot{\theta}_2{}', \tag{5-22}$$

the post-impact angular velocity of Part 2 as $\dot{\theta}_2{}'$ then can be obtained as

$$\dot{\theta}' = \frac{m_1(\dot{\theta}_1 - \dot{\theta}') + m_2\dot{\theta}_2}{m_2} \tag{5-23}$$

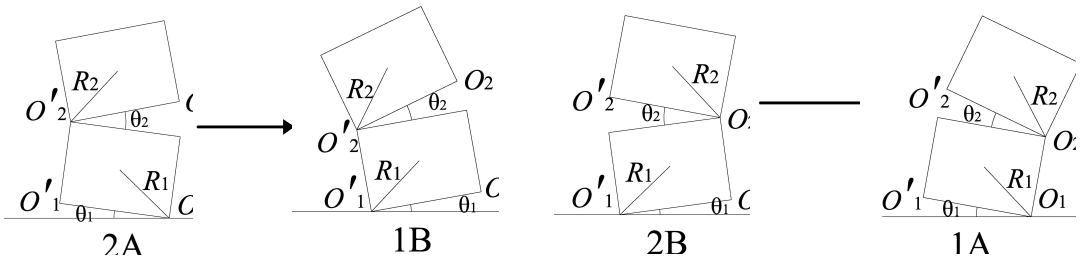

Figure 5.8 Transitions with impact after $\theta_1 = 0$

When $\theta_2 = 0, \theta_1 \neq 0$, as shown in Figure 5.9, the impact between Part 1 and Part 2 occurs. The corresponding restitution coefficient is

$$\gamma_2 = 1 - \frac{3}{2}\sin^2\theta_{c2} \tag{5-24}$$

The post-impact angular velocity of Part 1 as $\dot{\theta}_1'$ is determined by γ_1 and the angular velocity before the impact $\dot{\theta}_1$ as:

$$\dot{\theta}'_2 = -\gamma_2\dot{\theta}_2 \tag{5-25}$$

Based on the conservation of momentum:

$$m_1\dot{\theta}_1 + m_2\dot{\theta}_2 = m_1\dot{\theta}_1' + m_2\dot{\theta}_2', \tag{5-22}$$

the post-impact angular velocity of Part 2 as $\dot{\theta}_1'$ then can be obtained as

$$\dot{\theta}_1' = \frac{m_1(\dot{\theta}_2 - \dot{\theta}_2') + m_1\dot{\theta}_1}{m_1} \tag{5-26}$$

When $\theta_1 = 0, \theta_2 = 0$, the model returns to rest on the ground as one part. Two impacts, which are the impact of Part 2 with Part 1, and Part 1 with the rigid ground, occur simultaneously. After the impact, the model rocks up again still as one part, following Pattern 3A or Pattern 3B. Therefore, actually two processes exist in this case. First, the energy dissipation due to these two impacts should be considered using the restitution coefficient:

$$\dot{\theta}'_1 = -\gamma_1\dot{\theta}_1, \ \dot{\theta}'_2 = -\gamma_2\dot{\theta}_2$$

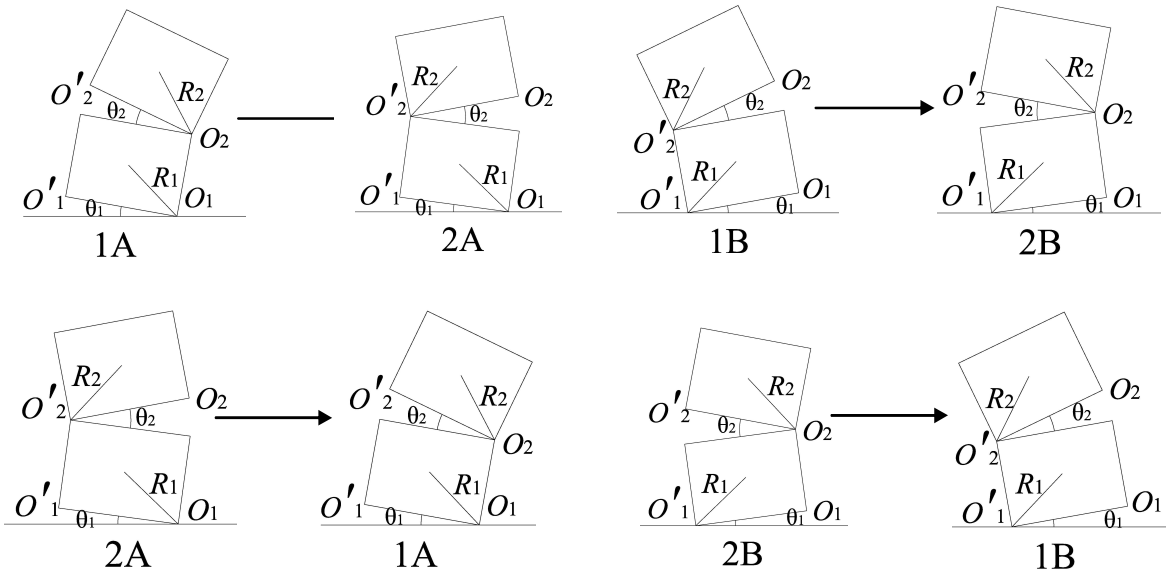

Figure 5.8 Transitions with impact after $\theta_2 = 0$

Secondly, the integral Pattern 3 rocking begins after the impact and the new velocity can be derived based on the conservation of momentum:

$$\dot{\theta}' = \frac{m_1\theta_1' + m_2\theta_2'}{m_1 + m_2}$$

Therefore, the velocity of the model after the impact as $\dot{\theta}'$ can be derived as

$$\dot{\theta}' = \frac{m_1\gamma_1\theta_1 + m_1\gamma_2\theta_2}{m_1 + m_2} \tag{5-27}$$

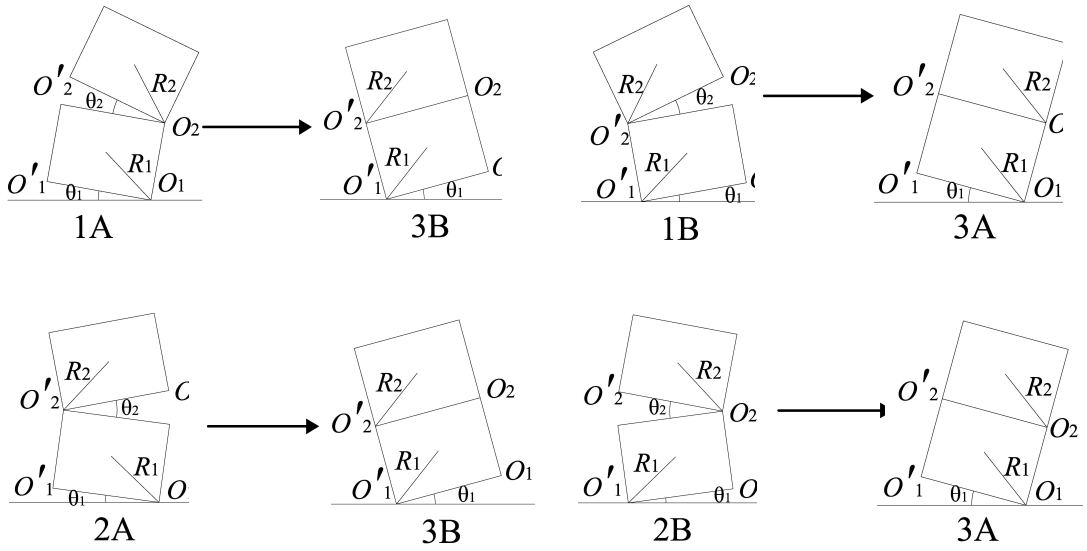

Figure 5.8 Transitions with impact after $\theta_1 = 0, \theta_2 = 0$

With the development of Pattern 3, the transitions to Pattern 1 or Pattern 2 without impact may occur once more if the conditions of Eq. (5-14) or Eq.(5-17) are satisfied.

The transitions among different patterns of motion and their corresponding conditions can be presented as follows.

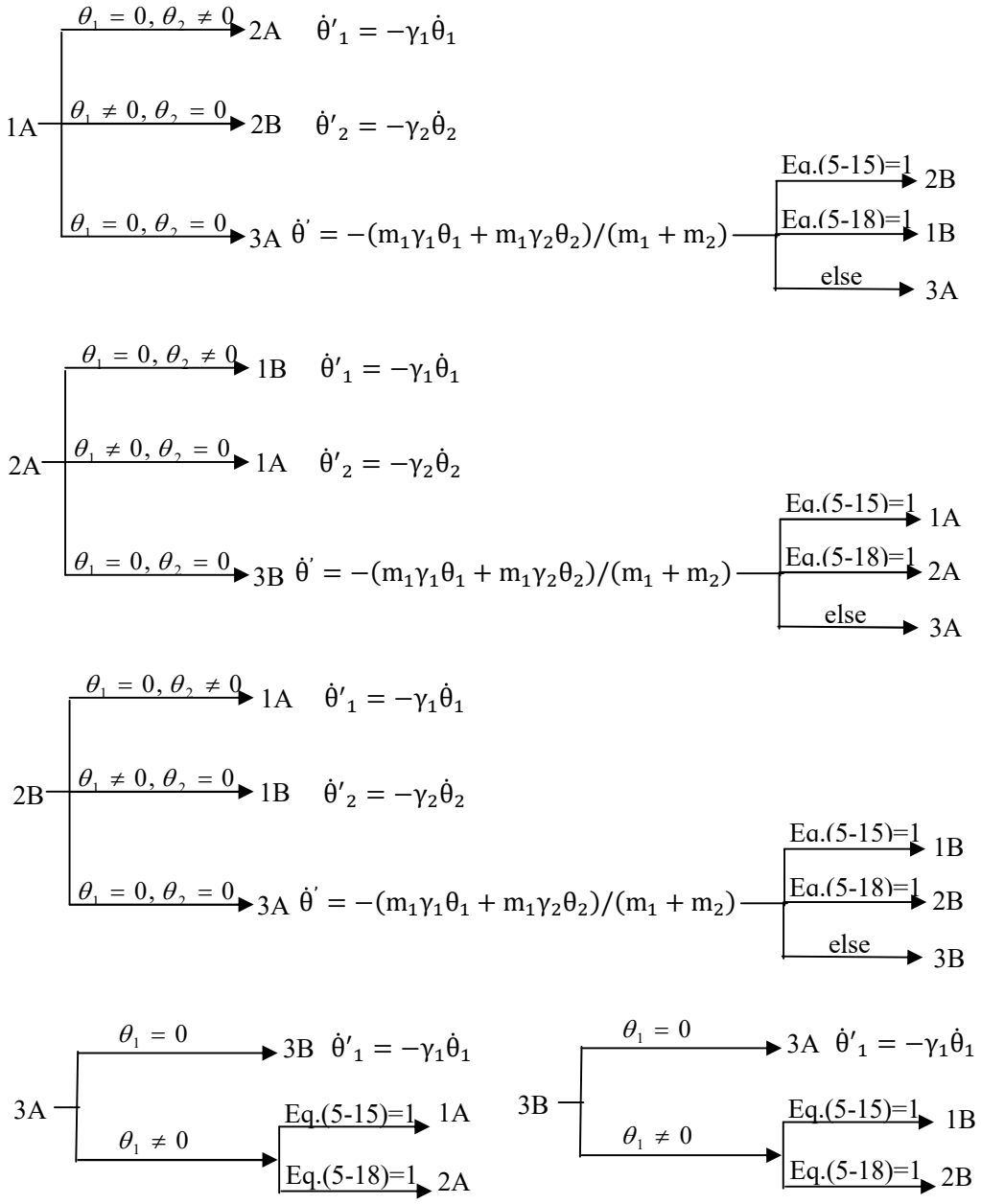

Figure 5.10 The transitions conditions between each two different pattern

5.4.5 Summary

Based on the experimental observations in Chapter 3 and Chapter 4, a two-rigid-body model standing freely on a rigid base is used as a theoretical model for the out-of-plane rocking of the façade in a masonry structure. The roof loads and corresponding frictional constraints from the beams are taken into account. It is assumed that only one crack between the two parts can be generated within the model. It is assumed that the only possible behaviour is rocking, with sliding, rotation damping and bouncing being ignored. Six possible rocking patterns are generated. The impact is defined to be inelastic. A restitution coefficient is used to describe the energy dissipation during impact.

The equations of motion for each pattern are derived. Due to the high nonlinearity of the equations, only mathematical solutions can be available. The model is assumed to start to rock integrally as Pattern 3. If the overturning moment on the model exceeds the corresponding restoring moment, rocking can commence. The initial Pattern 3 can transit to Pattern 1 or Pattern 2 without any impact, if the overturning moment on Part 2 exceeds the corresponding restoring moment. Transitions from Pattern 1 and Pattern 2 can occur with impact if any rocking angle becomes zero. Once the rocking pattern has been identified, the post-impact angular velocities of Part 1 and Part 2 are derived according to the restitution coefficient and the conservation of momentum.

Therefore, the rocking of the model is described by the rocking pattern and the angle solved from the equations of motion. These different motions are connected by transitions with and without impact. In this way, a complete process of response of the model to a horizontal excitation can be simulated. A simplified flow chart of the program which simulates the rocking behaviour of the model, the changes in crack location and the rocking patterns is given in Appendix II.

5.5 Analysis of Theoretical Results

Due to the high degree of nonlinearity of the above equations of motion, the general solution that is applicable for parametric analysis cannot be derived. Only the numerical solutions can be available for specific cases. The modelling work in this section firstly is expected to validate the theoretical model being set up in the above sections with the experimental results. On this basis, it is also expected to analyze the characteristics of the rocking behaviour being

presented by this theoretical model, as well as the influences of the parameters of structures and excitations.

5.5.1 The Runge-Kutta method

The fourth-order Runge-Kutta algorithm with ODE-45 in MATLAB was used to derive the solutions. In this algorithm, let an initial value problem be specified as follows:

$$\mathrm{y} = \mathrm{f(t,y)}, \dot{\mathrm{y}}(\mathrm{t_0}) = \mathrm{y_0} \tag{5-28}$$

For a selected step-size $h > 0$,

$$y_{n+1} = y_n + h\frac{1}{6}\left(k_1 + 2k_2 + 2k_3 + k_4\right) \quad (t_{n+1} = t_n + h), \tag{5-29}$$

For $n = 0,1,2,3\ldots$,

$k_1 = f\left(t_n, y_n\right)$,

$k_2 = f\left(t_n + \frac{1}{2}h, y_n + h\frac{1}{2}k_1\right)$,

$k_3 = f\left(t_n + \frac{1}{2}h, y_n + h\frac{1}{2}k_2\right)$,

$k_4 = f\left(t_n + h, y_n + hk_3\right)$

The fourth-order method means that the error per step is in the order of $\mathrm{O}\left(h^5\right)$, while the total accumulated error has the order $\mathrm{O}\left(h^4\right)$. In general,

$$y_{t+h} = y_t + h\sum_{i=1}^{4}\alpha_i k_i + \mathrm{O}\left(h^5\right), \tag{5-30}$$

where $k_i = f\left(y_t + h\cdot\sum_{j=1}^{4}\beta_{ij}k_j, t_n + \alpha_i h\right)$.

The Runge-Kutta method is the method that is most commonly employed by scientists to integrate ordinary differential equations, and has good accuracy and stability in solutions. As a one-step method, the global error being generated is of the same order as local error. The main advantages of Runge-Kutta method is that they are self-starting and do not require the calculation of higher order derivatives (Dutta 2006).

5.5.2 The theoretical model

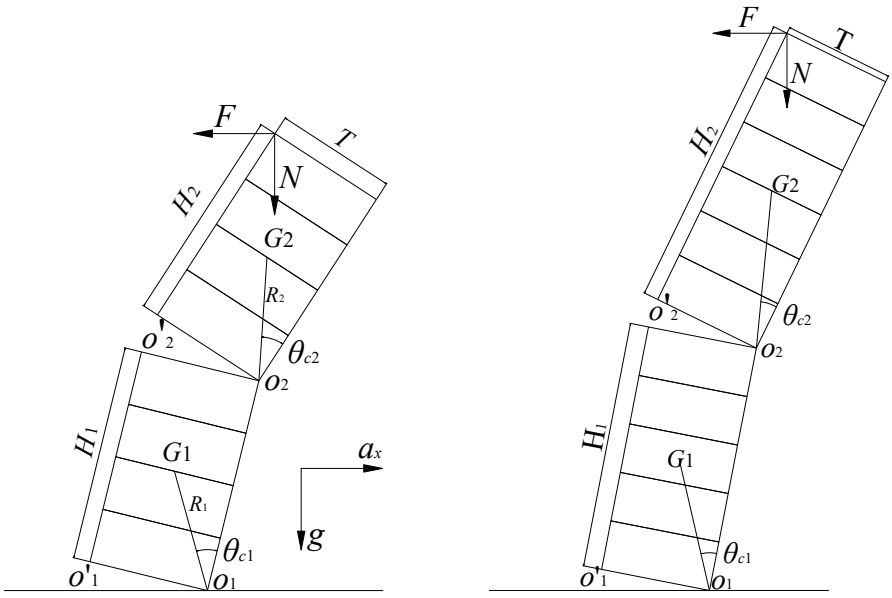

(a) Model II (b) Model III

Figure 5.11 The theoretical models of masonry façades for Model II and Model III

The y-axis rocking of Model II presents stable behaviour and experimental data in Chapter 4. The corresponding rocking of Model III can present the comparison of the differences in the rocking behaviour caused by the height of the façade. The excited portions in the y-axis rocking of Model II and Model III are modelled in this section.

The upper part and the lower part are respectively modelled by Part 2 and Part 1 in this two-rigid-body model. As both the upper part and the lower part in the shaking-table experiments in Chapter 4 contain symmetric and even distribution in both mass and shape, they are modelled as Part 2 and Part 1 in rectangular shape in the theoretical model for simplicity. The geometric forms of the theoretical models are shown respectively in Figure 5.11(a) and (b).

Table 5.1 Parameters for the theoretical models for y-axis facades in Model II and Model III

Model	T(mm)	H_1(mm)	m_1(kg)	H_2(mm)	m_2(kg)
Model II	50	140	6.05	140	9.41
Model III	50	175	6.72	210	14.11

The excited portion in Model II contains 8 layers and 46 bricks in total. There are 4 layers and

28 bricks in the upper part and 4 layers and 18 bricks in the lower part. Therefore, in the theoretical model in Figure 5.11(a), Part 1 and Part 2 have the same geometric dimensions, with less mass in Part 1. For the excited portion of Model III, the upper part contains 6 layers and 42 bricks. Five layers and 20 bricks are involved by the corresponding lower part. Therefore, in Figure 5.11(b), Part 1 has lower height and mass than Part 2. The magnitudes of the parameters for these models are given in Table 5.1.

The sets of excitations used in the experiments in Chapter 4 are applied on the corresponding theoretical models. On Model II, based on the same peak acceleration, the frequencies 1.8Hz, 2.0Hz, 2.5Hz and 2.8Hz were selected. On Model III, the frequencies 2.0Hz, 2.2Hz, 2.4Hz and 2.8Hz were selected. The geometric dimensions of each model and the group of excitations being applied are listed in Table 5.2.

Table 5.2 Dimensions and excitations of the theoretical model

Model	Dimension		Excitation		
	H(mm)	*T*(mm)	Frequency (Hz)	Amplitude (mm)	Peak acceleration (m/s^2)
Model II	280	50	1.8	12.00	1.53
			2.0	9.70	
			2.4	6.75	
			2.8	4.69	
Model III	385	50	2.0	7.81	1.23
			2.2	6.46	
			2.4	2.41	
			2.8	3.99	

The theoretical results on the modelling of Model II and Model III are compared with the corresponding experimental results. The results of Model II and Model III are also compared to illustrate whether the theoretical model can present the variations of the rocking behaviour with the height of the facade. Meanwhile, the parameters in the theoretical model, including the amplitude of excitation, the compression force on the top and the restitution coefficient at impact, are varied to demonstrate their influences on the characteristics of the rocking behaviour of the theoretical model.

Totally five cases are carried out to model under the following conditions:

Case 1 The theoretical model for the excited portion in Model II is set up, according to Figure 5.11(a). The group of excitations in Table 5.2 are applied. The theoretical results are compared with the corresponding shaking-table experimental results in Chapter 4.

Case 2 The theoretical model for the excited portion in Model III is set up, according to Figure 5.11(b). The group of excitations in Table 5.2 are applied. The theoretical results are compared with the corresponding experimental results for a further validation on the theoretical model. Comparisons are also made between the theoretical results of Model II and Model III, in order to clarify variations of the magnitude and patterns of the rocking with the height of the façade.

Case 3 The additional excitations at 2.8Hz, but with larger amplitudes, are applied on the theoretical model of the excited portion in Model II. This is to study whether the magnitude and pattern of the rocking behaviour in this theoretical model are sensitive to the peak acceleration of the excitation.

Case 4 The excited portion in Model II is modelled, with the compression force on the top being removed, that is, $N = 0, F = 0$. This is to study the influence of the top loads on the dynamic rocking of the theoretical model.

Case 5 The restitution coefficient is set as $\gamma = 1$ on the theoretical model of Model II, to study the effect of the magnitude of impact on the dynamic rocking behaviour.

5.5.3 Analysis of the theoretical results on Model II

For Case 1, the spectrum diagrams of response of the theoretical model of Model II at different excitations are given by FFT in Figure 5.12. The spectrums at different excitations consistently illustrate that the model oscillates in random frequency during the process. No characteristic frequency can be shown in either case. The random frequency of rocking after each impact is the typical characteristic of rigid-body system. This deviates from the experimental conclusion that Model II responds globally as a forced vibration following the frequency of excitation, with a characteristic frequency in each axis. Therefore, this theoretical model cannot present the forced-vibration characteristic and the characteristic frequency of a continuum, but present the rigid-body characteristics in the response behaviour.

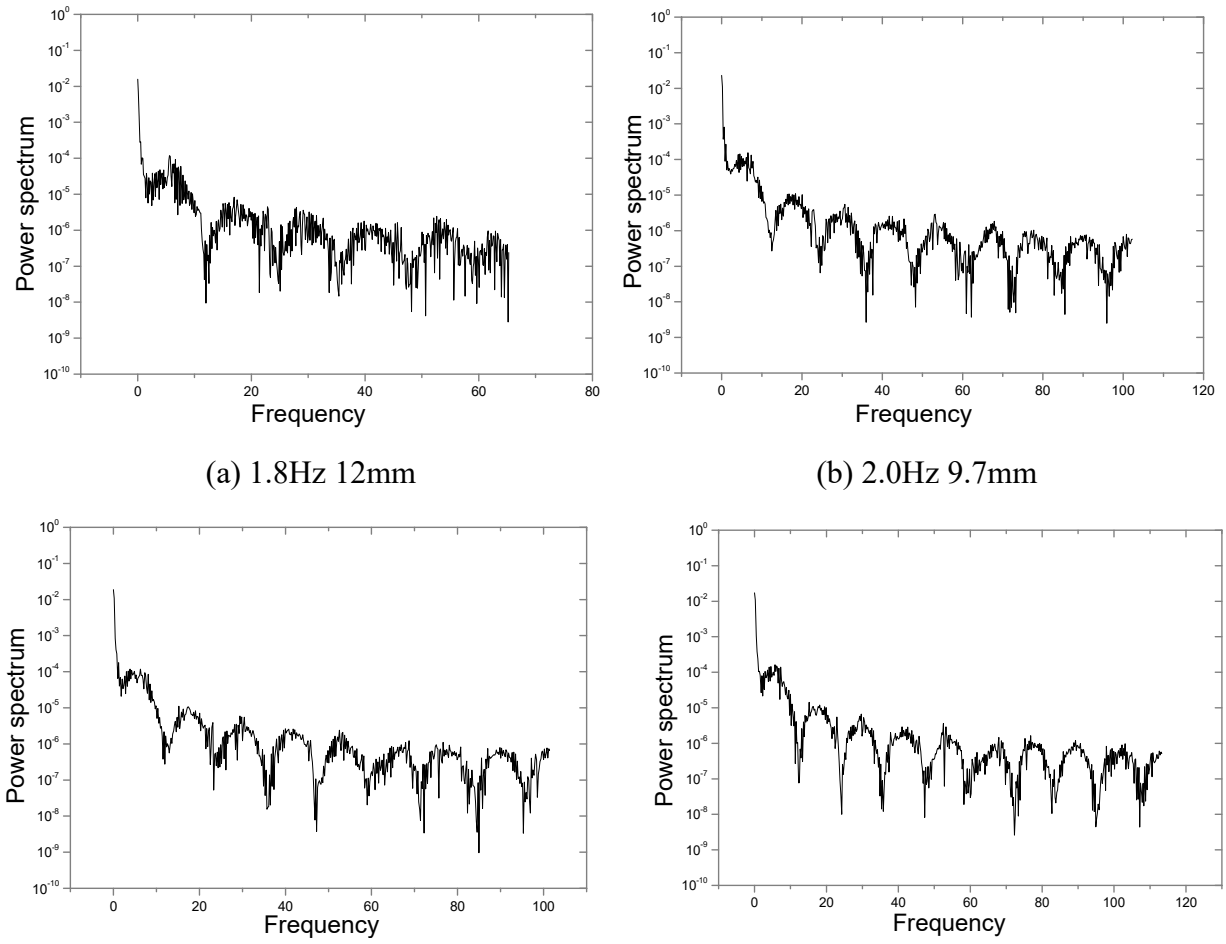

(a) 1.8Hz 12mm (b) 2.0Hz 9.7mm

(c) 2.4Hz 6.75mm (d) 2.8Hz 4.69mm

Figure 5.12 The spectrum diagrams of the theoretical model of Model II

On the other hand, this theoretical model presents stable and consistent rocking magnitude in the whole process. The responses are observed to present similar behaviour, including the magnitude and the rocking pattern, in the group of excitations with the constant peak acceleration. Therefore, the results at 2.8Hz sometimes are selected as the example of the theoretical model of Model II in the following studies. The processes and magnitudes are presented as being similar at different excitations.

The stable rocking can be observed from the time-history graphs of the rocking angles θ_1 and θ_2 in Figure 5.13(a) and (b). The four excitations consistently give stable magnitudes for both θ_1 and θ_2. The stable rocking magnitude shown by the theoretical model is different from the random magnitude of oscillation shown by the rigid body in the literature. This indicates that the two-rigid-body model here may present better descriptions on the out-of-plane rocking of

the masonry structure. Certain characteristics of the experimental rocking can be contained in this two-rigid-body model.

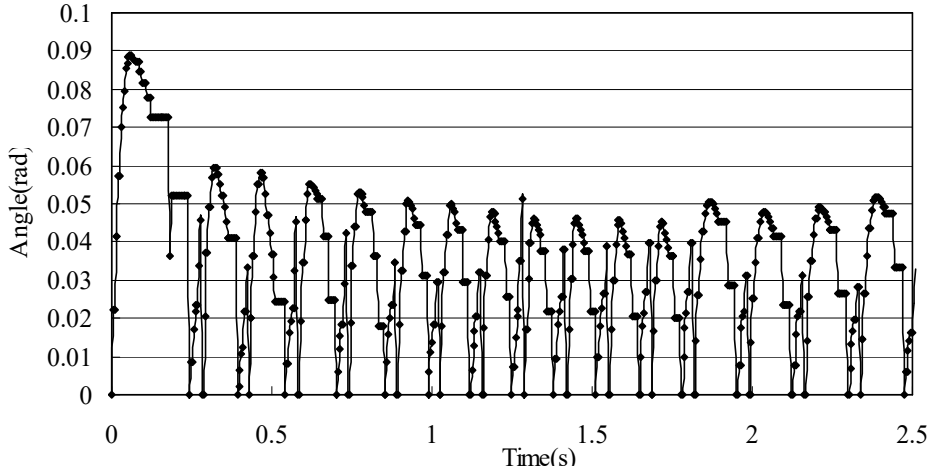

(a)

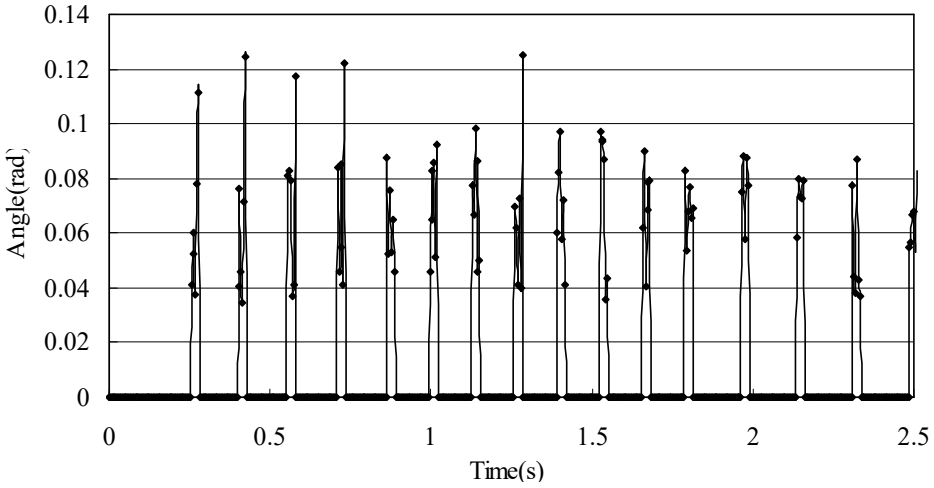

(b)

Figure 5.13 The rocking angles of the theoretical model of Model II in the process of response at 2.8Hz ((a) θ_1 ; (b) θ_2)

θ_1 is the predominant rocking angle with much larger magnitude than θ_2 in most of the time, which averagely stays around 0.05rad. θ_2 keeps to be zero usually and only reaches the equivalent magnitude some of the times. Larger magnitude shows in these points on θ_2 than the stable magnitude of θ_1, which is around 0.1rad. This is consistent with the experimental results that the predominant rocking is the integral response of the upper and lower parts, while

the upper part only present clear separate rocking occasionally.

Meanwhile, the development of θ_1 is consistent with the development of rocking of the façade in the shaking-table experiments. Higher amplitudes are given in the beginning and smaller magnitudes are shown in the following constant level. The amplitudes increase a little level again by the end of the rocking.

As the experimental data being measured in the shaking-table experiments are the displacements at the top façade, for the comparison with the experimental results, the displacement at the top of the model is derived from the geometric dimension and the rocking angle of each part, as:

$$d = h_1 \sin\theta_1 + h_2 \sin\theta_2 \tag{5-31}$$

As the responding frequency in each oscillation still present to be random in the theoretical model, the time-history behaviour of the top displacements cannot be comparable, both between the theoretical results at different excitation and between the experimental and theoretical results. Therefore, the amplitudes in each oscillation of rocking are selected to compare. In Figure 5.14, the theoretical amplitudes of Model II at different excitations are compared. In Figure 5.15, the comparison between the theoretical and the corresponding experimental amplitudes of Model II at each excitation are shown in Figure 5.15.

In Figure 5.14, the stable magnitude of rocking of this theoretical model is illustrated once more. A constant level of amplitudes is shown in the whole process of response at each excitation. Meanwhile, the excitations with different frequencies under the constant peak acceleration have offered similar magnitudes of rocking on the theoretical model in Figure 5.14. The largest amplitudes are around 15mm, being presented at 2.4Hz. The smallest level of amplitude is around 10mm, which is shown at 1.8Hz. As the amplitude of excitation decreases with the increase of frequency based on the constant peak acceleration, the amplitude of response does not show the displacement-sensitive characteristic which is also the typical characteristics for the discrete rigid body, like the random rocking process. However, with the similar amplitudes of responses under the constant acceleration, the frequency-sensitive characteristic is also not presented in this theoretical model. Therefore, the excitations with increased amplitude at constant frequency are applied in the following analysis.

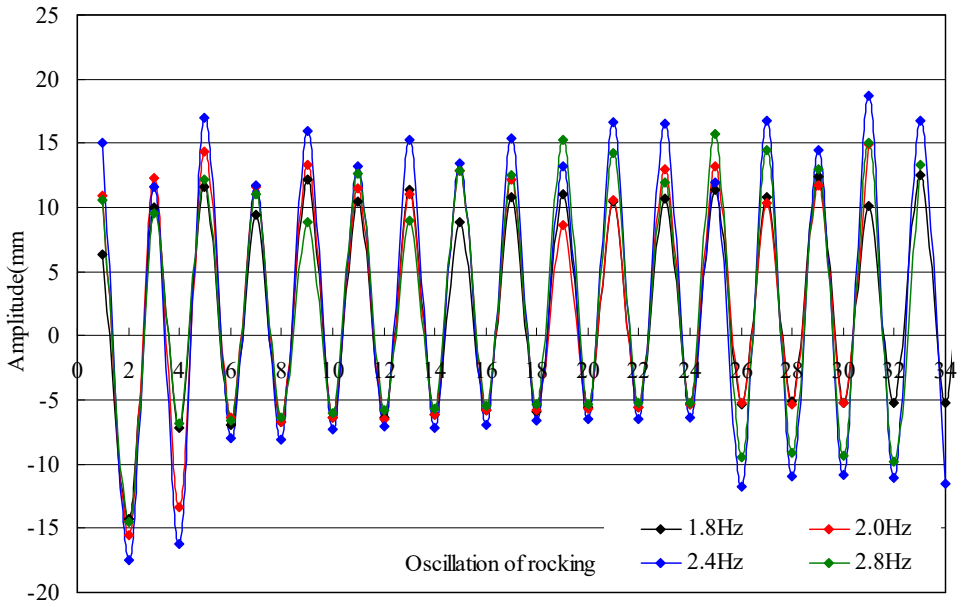

Figure 5.14 The rocking amplitudes of the theoretical model of Model II

In Figure 5.15, the differences in the displacement amplitudes of rocking from the theoretical and experimental models at each excitation are shown. The theoretical and experimental rocking amplitudes present basic consistencies in the positive direction, but shows clear differences in the negative direction. This originates from the larger influence of the separate motions of bricks in this direction in Chapter 4. The average errors at 1.8Hz, 2.0Hz, 2.4Hz and 2.8Hz are respectively 33.2%, 34.7%, 36.8% and 31.4%, which are acceptable for a simplified theoretical model taking into account the experimental separate motions in the negative direction. As the experimental model is frequency-sensitive, the experimental amplitude decreases consistently when the frequency of excitation decreases from the characteristic frequency of 2.8Hz. In contrast, the theoretical results present smaller variations on the rocking magnitude at different frequencies. The smallest error between the experimental and theoretical results is at 2.8Hz, which has been identified to be the characteristic frequency for Model II. Therefore, this theoretical model can relatively better describe the magnitude of rocking for the masonry façade at resonance.

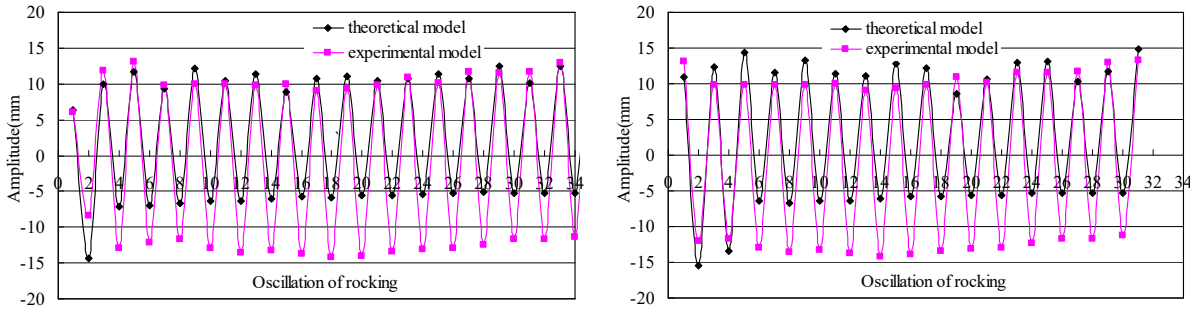

(a) (b)

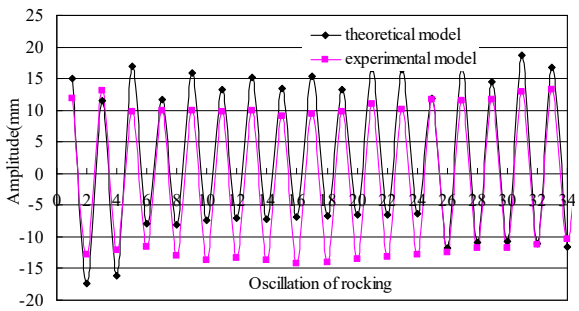

(c)

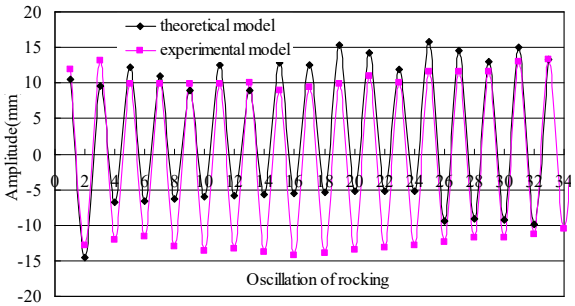

(d)

Figure 5.15 The comparisons between theoretical and experimental amplitudes of Model II ((a) 1.8Hz; (b) 2.0Hz;(c) 2.4Hz; (d) 2.8Hz))

For resonance, the rocking pattern in each oscillation of rocking with its duration is studied in Figure 5.16. This shows that during the process of theoretical rocking, Pattern 3 is the most common pattern, while Pattern 1 and Pattern 2 exist intermittently. Meanwhile, the oscillation in Pattern 3 keeps in a longer time, while the oscillation in Pattern 1 and Patten 2 end to impact quickly, especially in Patten 2. Compared with the stable Pattern 3 and Pattern 1 in the process of response, Pattern 2 only exists for a very short time. The large rocking angle θ_2 falls down quickly so that θ_1 and θ_2 become zero at the same time and the transition to Pattern 3 occurs. Pattern 3 may transit to Pattern 1 without an impact; Pattern 1 then transits to Pattern 2 each time by an impact between Part 2 and Part 1.

The experimental data also shows that when Pattern 3 transits to Pattern 1, the rocking angle θ_1 reduces to a smaller value. The upper rocking angle θ_2 obtains a slightly larger magnitude than θ_1. The magnitudes of both θ_1 and θ_2 remain stable in different oscillations of rocking. At the end of each oscillation of Pattern 1, Part 1 first impacts on the ground and changes its rocking reference point and velocity, to generate Pattern 2. Referring to Figure 5.14, the magnitude of θ_1 decreases a little due to the impulsive effect, while θ_2 increases quickly to a very high level. Therefore, the process of transitions during the rocking illustrates that the façade has much larger displacement on the top and lower stability in Pattern 2, and correspondingly the highest vulnerability. The rocking in Pattern 3 and Pattern 1 is relatively stable during the process.

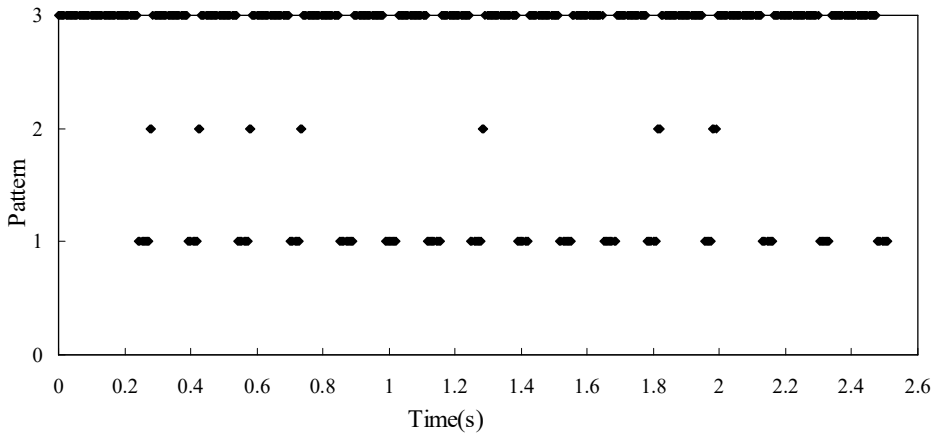

Figure 5.16 The rocking pattern of Model II in the process of response at 2.8Hz

This rocking process of the theoretical model of Model II shown in Figure 5.14 and Figure 5.16 coincides with the experimental behaviour of the model. Based on the experimental observation, the portion being excited within the façade rocks integrally as one portion most of the time. However, the upper part will sometimes present a little extra rock. Occasionally, the separate rocking at the upper part may suddenly become extremely large and causes final collapse. This consistency in rocking patterns between the theoretical and experimental observations also validates this theoretical model. Therefore, besides presenting the rocking magnitude at resonance with an acceptable extent of error, this theoretical model with two rigid bodies also gives proper description of the predominant out-of-plane rocking of the masonry structure during the process of response on the mechanism.

As has been concluded in the literature (Peña, Prieto et al. 2007), the rigid-body model is very sensitive. Even slight changes on parameters can cause large variations on the theoretical results. The modelling of Model II shows that because the hypotheses assumed by the classical theory are not completely fulfilled, the theoretical model cannot present the experimental behaviour completely.

In summary, the modelling work on Model II with this theoretical model substantially evaluates its reliability and stability, and presents some characteristics of it. This two-rigid-body theoretical model cannot present the frequency-sensitive characteristics of the experimental mode. The constant responding frequency of Model II in experiments cannot be presented properly, due to the inherent properties of the rigid body. On the other hand, stable rocking magnitudes and patterns during the process of response are given by the theoretical model. The rocking magnitude can be presented with acceptable error to the experimental rocking at resonance. Both the rocking patterns given by the theoretical model and the

characteristic that the variation of the rocking pattern is not related to the excitations coincide with the experimental observations in practice.

5.5.4 Parameter analysis on the theoretical model

The modelling work in Case 1 evaluates the consistency and reliability of the theoretical model. The characteristics of the theoretical model that can describe the experimental behaviour of Model II properly are presented and discussed. The characteristics of the rigid-body system it contains are illustrated as well.

From Case 2 to Case 5 in this section, parameters of both excitation and structure in this theoretical model are varied, on the basis of modelling work on Model II, to carry out a parameter analysis. This analysis can further validate the theoretical model, and clarify the influence of different parameters on the rocking behaviour of this theoretical model.

In Case 2, the theoretical modelling is carried out on the y-axis façade of Model III. The theoretical results are compared with the corresponding experimental results, to validate this theoretical model. The results presented are also used to compare the characteristics of the rocking behaviour from modelling Model II and Model III by this theoretical model.

As shown in Table 5.1, the ratio of the heights of the theoretical model of Model III and of Model II is 1.375, with the ratio of their total mass as 1.347. Furthermore, the distributions in geometric and mass of Model III also vary from those in Model II. The ratio of height for Model II is 1.0 between Part 2 and Part 1, while this ratio for Model III increases to 1.2. The ratio of mass between Part 2 and Part 1 varies from 1.56 for Model II to 2.10 for Model III. Therefore, the comparison between the results from the theoretical modelling of Model II and Model III can illustrate the influence of the geometric and mass distributions on the characteristics of rocking behaviour for this theoretical model.

When performing Case 2, the mathematical program fails in the case with the excitation at 2.2Hz. This may rely on the instability when solving the highly nonlinear equations. The increased vulnerability and difficulties to obtain stable solution with the increase on its height and mass of Model III may have some influences. Therefore, only the results at 2.0Hz, 2.4Hz and 2.8Hz are used in the following analysis.

Consistent characteristics of the theoretical results are presented when modelling Model III

with the characteristics shown in the modelling of Model II. The comparison between the displacement amplitudes on the top from the theoretical model and the experimental model are shown in Figure 5.18. The theoretical displacements are derived based on Eq. 5-31.

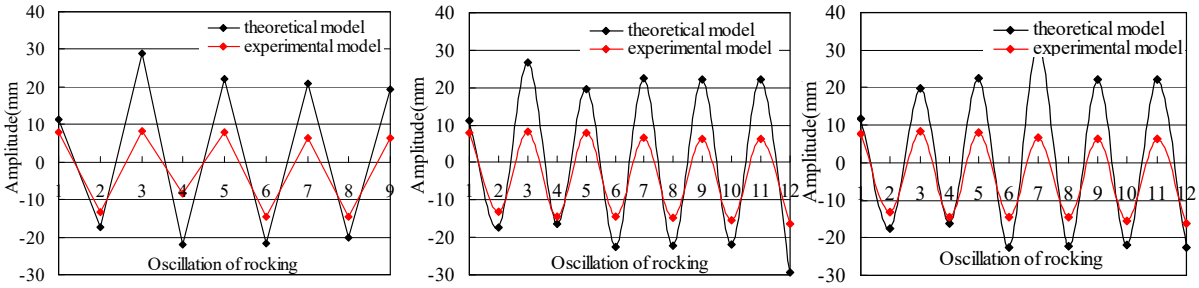

Figure 5.17 The comparisons between theoretical and experimental amplitudes of Model III ((a) 2.0Hz; (b) 2.4Hz; (c) 2.8Hz)

Stable and consistent theoretical responses are observed at different excitations once again on Model III. The observations and conclusions from the modelling work on Model II are also confirmed. The theoretical model being set up in the former section is validated. On the other hand, larger errors are presented by the theoretical model of Model III in Figure 5.17. At 2.0Hz, 2.4Hz and 2.8Hz, the average errors are respectively 45%, 39% and 38%, compared with the corresponding average errors as 33.2%, 34.7%, 36.8% and 31.4% in Model II. It is shown in Figure 5.17 that the errors are principally generated in the opposite direction, while in the negative direction the theoretical and experimental amplitudes present better consistencies. Because the experimental results are influenced little by the separate motions on bricks, the larger errors are caused by the larger portion contained in the continuous arching effect with the increased height in the experiments, which differs from the discrete separate rocking in the theoretical model. Meanwhile, the asymmetric geometry and mass distribution in the experiments and the simplified theoretical assumptions also present larger influence with the increase of the brick numbers in Model III. As it has been observed in Chapter 4 that the characteristics of the discrete models are stable and the same test is repeatable, the errors from the experimental tests are limited. Therefore, the clear errors shown in Figure 5.15 and Figure 5.17 principally come from the assumptions in the theoretical model, which needs to be improved in the future work. For example, the simplifications on mass and geometry of the model, the descriptions on the impact behaviour and the contact with the ground, etc.

The rocking angles of θ_1 and θ_2 at 2.8Hz are shown in Figure 5.18. Similar stable processes

of development of θ_1 and θ_2 in the response are also given by the other excitations at the constant peak acceleration. This, consistent with the responses of Model II, proves the validity and reliability of this theoretical model. Compared with the displacement amplitudes obtained from the theoretical model of Model II, clear increase has been presented by the amplitude of the theoretical model of Model III. Additionally, the highly vulnerable conditions are consistently shown in Figure 5.18. Substantially increased rocking angle θ_2 in Part 2 can be observed. The large magnitude of θ_2 is reached suddenly after the impact from Pattern 1 in all cases. This demonstrates the large effect of the geometrical form on the magnitude of the rocking in this theoretical model, which also explains the errors between the theoretical and experimental models.

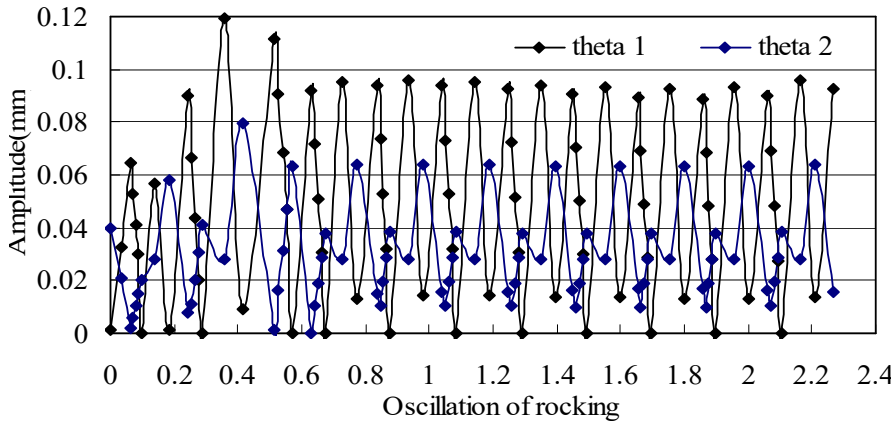

Figure 5.18 The rocking angles of the theoretical model of Model III in the process of response at 2.8Hz ((a) θ_1 ; (b) θ_2)

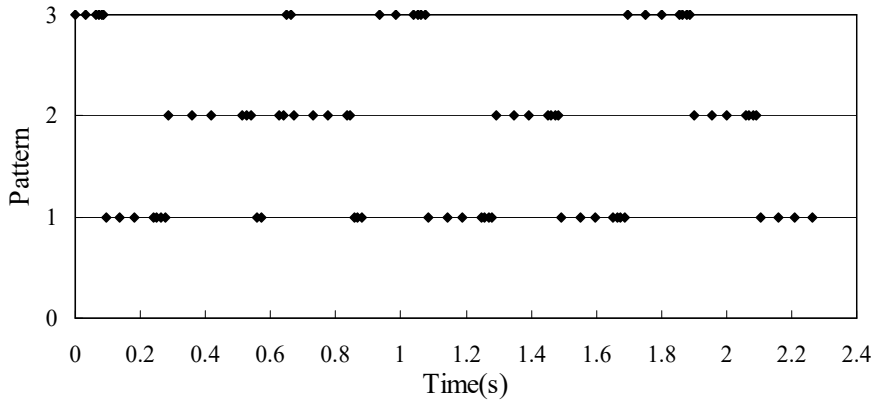

Figure 5.19 The rocking pattern of Model III in the process of response

More frequent transitions among patterns with more types are observed in the rocking of Model III, as shown in Figure 5.19. The duration of oscillation in each pattern reduces to a shorter time. The rocking pattern from Pattern 3 transits to Pattern 1 shortly after the first impact. In the subsequent response, the transition between Pattern 1 and Pattern 2 occurs in most of the time. In contrast, Pattern 3 only occurs occasionally and transits to other patterns quickly after the occurrence. Pattern 2 is shown to be an unstable and vulnerable status, which generates large displacements in a short time.

In the model of Model III, consistent and stable rocking is presented once more, which is similar with the behaviour shown by the theoretical model of Model II. Conclusions obtained from Model II in the above section are confirmed, which further validates the theoretical model. On the other hand, the heights of both Part 1 and Part 2 increase in Model III. The greater slenderness indicates a smaller critical acceleration to initiate a motion and higher vulnerability. Additionally, the upper Part 2 becomes higher than Part 1 and gains especially larger mass. These variations influence the rocking patterns and the transitions. These differences have demonstrated the sensitivity of the rocking response of this theoretical model to its geometric and mass distributions.

In Case 3, as similar rocking magnitudes have been given at different frequencies of excitations with the constant acceleration, more excitations at 2.8Hz with different amplitudes are applied on the theoretical models. Excitations with constant frequency as 2.8Hz, but increased amplitudes of 4.69mm, 8mm and 11mm are applied.

The theoretical results show that at excitations with increased amplitudes of 8mm and 11mm but constant frequency as 2.8Hz, the same rocking patterns as at 2.8Hz 4.69mm excitation in Figure 5.16 are presented. This further stresses the stable rocking given by the theoretical model. The consistent rocking pattern at different groups of excitations also coincides with the conclusion from the experimental model that the damage mechanism only relates to the structural configuration and does not influenced by the type of excitation. The proper description of this theoretical model on the rocking behaviour of the experimental model on mechanism is further proved.

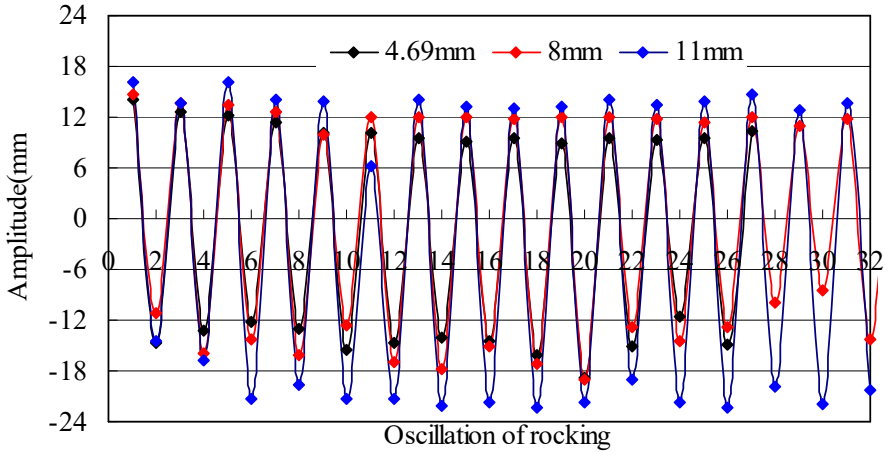

Figure 5.20 Comparison of the rocking amplitudes at excitations with different amplitudes

Figure 5.20 gives the comparison of the rocking amplitudes at excitations with 2.8Hz frequency but 4.69mm, 8mm and 11mm amplitudes. With the similar stable processes presented at these three excitations, clear increase can be observed on the amplitude of response with the increase of amplitude of excitation. Therefore, the theoretical model illustrates the acceleration-sensitive characteristic, which is consistent with the response of the masonry model in experiments at excitations with constant frequency.

Case 4 is carried out to study the influence of the top load on the rocking behaviour of this theoretical model. The compression force N on the top is removed. The frictional force F is correspondingly as $\mu N = 0$. In this way, the theoretical model becomes a two-rigid-body system standing freely on the rigid ground without any constraint. The same group of excitations in Table 5.2 applied formerly on Model II is used.

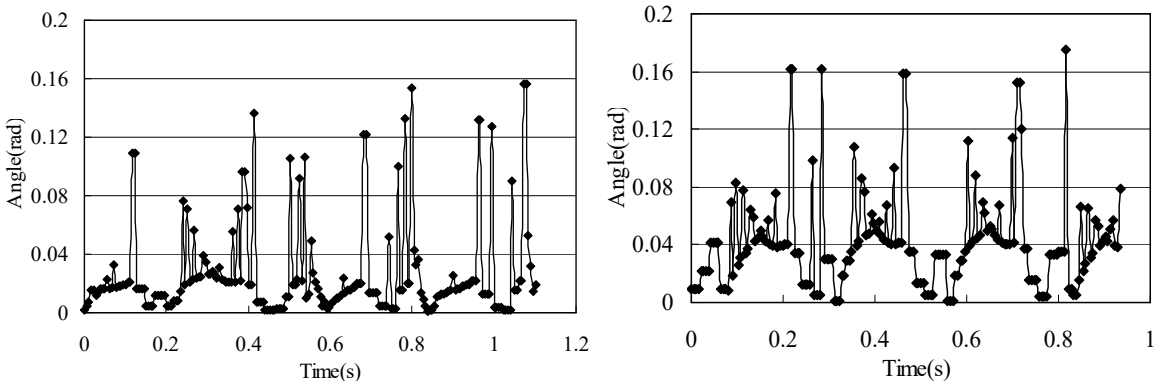

(a) (b)

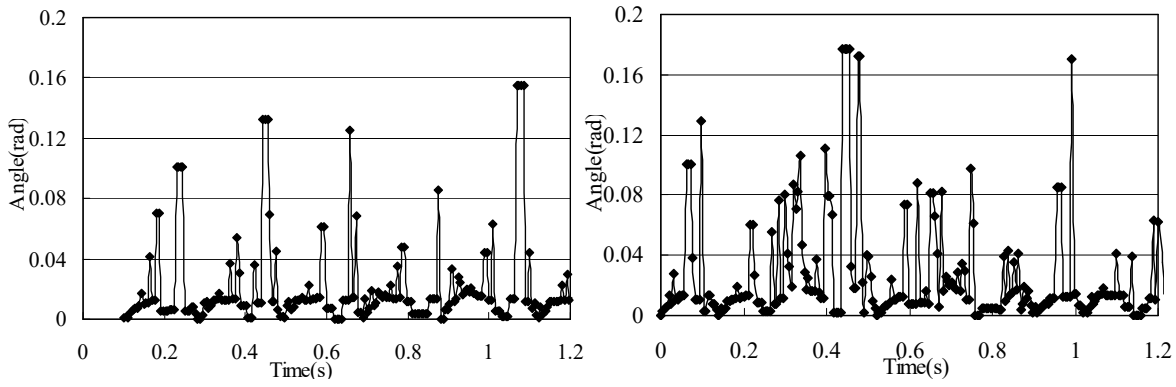

(c) (d)

Figure 5.21 The rocking angle θ_1 of the theoretical model of Model II with *N*=0 ((a) 1.8Hz; (b) 2.0Hz; (c) 2.4Hz; (d) 2.8Hz)

The rocking characteristics vary largely in Case 4 as the top loads being removed. First, only Pattern 3 is observed during the responses in all cases. No transition to Pattern 1 or Pattern 2 can be observed. Meanwhile, the variation on the rocking angle at each excitation is no longer stable and consistent with each other.

Figure 5.21 gives the developments of the rocking angles θ_1 at different excitations in Case 4. The release of *N* and *F* changes the rocking response to a random process, in both the frequency and the magnitude. The characteristics of the rigid-body motion are illustrated to a much larger extent. Therefore, the main effect of the loads and frictions on the top is to maintain the stability of the rocking behaviour of this rigid-body model, including the consistent amplitudes and pattern transitions. These characteristics have made the theoretical rocking of this discrete model closer to the rocking of the experimental model in practice. It is the proper constraints on the top that ensures the proper modelling of the masonry structure with rigid-body system.

In Case 5, the situation of elastic impact is applied in the theoretical model of Model II, which assumes restitution coefficient to be $\gamma = 1$, to study the influence of the restitution coefficient on the theoretical rocking behaviour. The excitations which were formerly applied in Model II in Table 5.2 are used in this situation once again. The results with the two restitution coefficients of, respectively, Eq.(5-19) as the inelastic impact, and $\gamma = 1$ as the elastic impact, are compared.

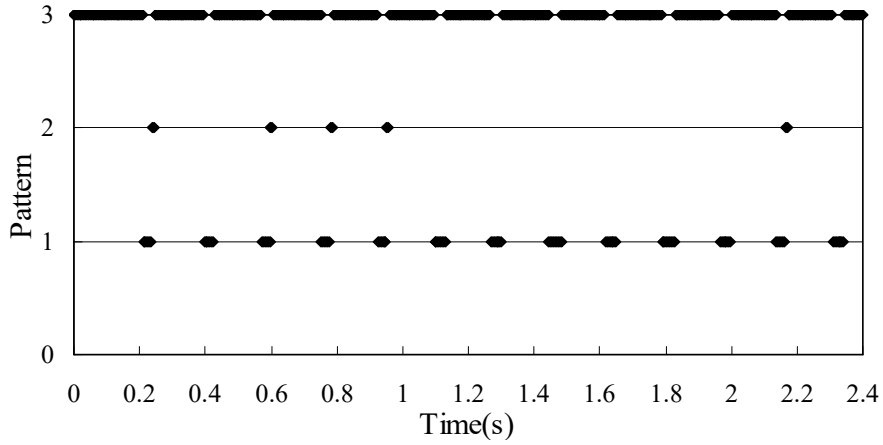

Figure 5.22 The rocking pattern of Model II at 2.8Hz under elastic impact

Figure 5.22 presents the rocking patterns of each oscillation of rocking during the process at 2.8Hz in Case 5. The time-history curves of θ_1 and θ_2 at 2.8Hz, compared with the original inelastic case, are shown in Figure 5.23. The responses at other excitations present the similar patterns in the processes. The amplitudes of the top displacements at these four excitations are presented in Figure 5.24.

The rocking pattern at 2.8Hz presents stable variations in Figure 5.22. The variations at other excitations present consistent variations. The patterns and the transitions are similar with the situations in the corresponding cases with inelastic impact in Case 1. However, Pattern 2 occurs on fewer occasions on the rocking pattern. Pattern 3 and Pattern 1 gain higher dominance. The oscillation at Pattern 3 develops in a longer time, compared with the corresponding observation in Case 1 with inelastic impact.

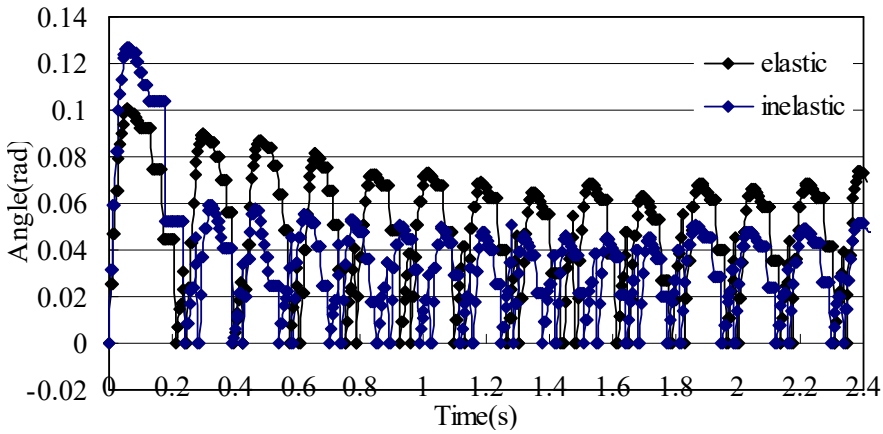

(a)

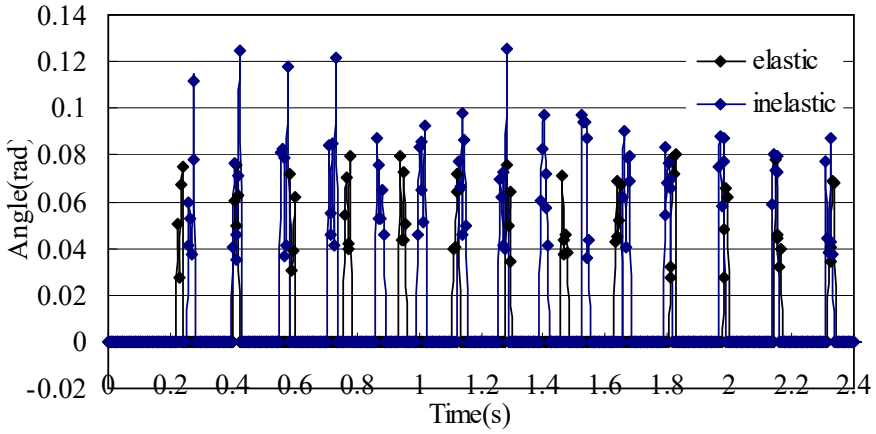

(b)

Figure 5.23 The comparison of the rocking angles between elastic and inelastic cases

In Figure 5.23, the larger rocking angles are illustrated on both θ_1 and θ_2 at elastic impact. The assumption that there is no energy dissipation on elastic impact offers larger rocking angles after each impact. However, a response process similar to that seen in the inelastic impact is presented. Meanwhile, in Figure 5.24, consistent and stable amplitudes have been shown at different excitations, which is similar to the behaviour in the other cases. The larger values obtained at the elastic impact also validate the reliability of this theoretical model. The developments of displacements further identify the stable rocking process at the elastic impact.

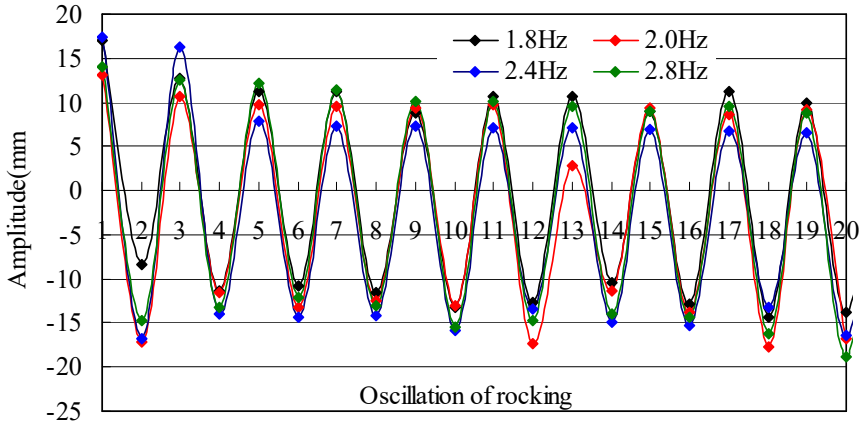

Figure 5.24 Comparison of the rocking amplitudes at different excitations with elastic impact

Therefore, these results have consistently demonstrated that the magnitude of the restitution coefficient being defined cannot influence the stability of the rocking behaviour, and has limited effect on the rocking pattern and transitions. It only influences the magnitude of

rocking after each impact.

5.6 Conclusions

The rocking behaviour of the masonry façade is mathematically modelled in this chapter, based on the theory of rigid-body dynamics. According to the experimental observation that the excited portion can in fact be divided into two parts, a mathematical model consisting of two stacked rigid bodies on a rigid base is set up. The loads and frictional force from the beams on the top are included as top constraints, with a base excitation being applied. The separate sliding and rotation of individual bricks are not taken into account in the model. Some basic assumptions of rigid ground, inelastic impact and point contact are adopted.

These two rigid bodies may rock either as one integral system or separately with either corner as the joint point. Three patterns of motion have been defined. Each pattern was subdivided into two further cases, depending on the reference points of rocking for each part. The nonlinear dynamic equations of motion for each pattern are derived and solved. The impact is described by the restitution coefficient and the conservation of angular momentum. The conditions for possible transitions between different patterns with or without impact are given. The challenge is associated with the high nonlinearity and complexity in the equations of motions and transitions. The equations were solved using a four-order Runge-Kutta algorithm with ODE-45 available in MATLAB.

Two models are set up and analysed, which are the y-axis façade of Model II and the y-axis façade of Model III. Sets of excitations used in the shaking-table experiments are applied. The theoretical model is evaluated through comparing the theoretical results with the experimental results. The influences of the parameters, including the amplitude of excitation, the structural geometry, the top compression force, the restitution coefficient, are studied, based on the theoretical model of Model II.

Stable and consistent results are given in all cases. Stable rocking, in magnitudes and transitions between patterns, can be given by this theoretical model. This stable rocking being presented, can identify the magnitude of experimental rocking at resonance with an acceptable error. The mechanisms of the rocking behaviour in practice are modelled properly, with integral rocking in the excited portion globally and a little extra rocking in the upper part. Pattern 1 and Pattern 3 are identified to be the stable status. Pattern 3 is the most common

pattern in rocking. Pattern 2 is the least likely to occur but is the most vulnerable and unstable pattern, which suddenly generates extremely large displacement.

The parameter analysis demonstrates that the rocking pattern and transitions are determined by the inherent properties of geometric form and mass distribution of the model. The slender model, especially when the upper part is higher with larger mass, presents more frequent transitions and larger rocking. The stability and characteristics of the theoretical model that are consistent with the characteristics shown in the experiments are maintained by the load and constraint on the top. The release of the top compression can induce the random rocking behaviour of the theoretical model, as a rigid body. The magnitude of restitution coefficient influences the rocking magnitudes, but cannot influence the stability and has limited effect on the patterns of rocking.

However, limitations still exist. This theoretical model, with the inherently rigid-body property, cannot present the frequency-sensitive characteristic of the experimental model, but can present the increased rocking amplitude with the increase of the amplitude of excitation at certain frequency. These should be improved in the future work, by adjusting the properties of the rigid body. The consideration of possible sliding and viscous may also help to present these characteristics.

Chapter 6 Conclusions

6.1 Conclusions

A systematic study of the post-crack dynamic behaviour of the masonry structure treated as rigid bodies was conducted. Pseudo-static experiments, dynamic shaking-table experiments and mathematical modelling work based on rigid-body dynamics theory were all involved. The main emphasis was on the damage mechanism, the effect of the structural configurations and characteristics of the responses to horizontally imposed ground level excitation.

The pseudo-static experiments investigated the behaviour of the dry masonry wall under the action of a steadily increasing horizontal force. These experiments were carried out on scaled masonry walls using two sizes of bricks. Out-of-plane and in-plane damage mechanisms were presented. This essential static-force experiment provided relatively conservative information on the capacity of a real masonry wall to bear a dynamic horizontal force. These dry brick walls behaved in qualitative terms just like the normally mortared walls on which previous researchers have reported in the literature. These experimental studies in the static phase also offer the basis for the following dynamic experimental study and theoretical modelling work.

The shaking table experiments can present the structural dynamic behaviour which is closer to the realities. The mortar has no influence on the post-crack behaviour, and this approach allows many more tests to be carried out economically in a certain time. Repeated experiments were carried out on three types of 1/10-scale masonry models. The out-of-plane behaviour of the façade, with the accompanied in-plane responses of the side wall on complete 3D models with model construction variables and model constraint variables, to a range of sinusoidal input excitations, was studied. Based on the pseudo-static experiments, the globally out-of-plane rocking was focused on. The experimental results validate the conclusions of the pseudo-static experiments undergoing dynamic vibration. The dry masonry models, relying on pure friction for cohesion, were used.

Based on the experimental studies, a mathematical model with two stacked rigid bodies was built up, based on the theory of rigid-body dynamics, describing the out-of-plane rocking of

the masonry structure dynamically. Sliding, rotation and viscous effects were ignored. The loads and frictional force on the top were included, with a horizontal excitation being applied. Assumptions of rigid ground, inelastic impact and point contact are applied. Six patterns of motion have been defined. Equations of motions and transition conditions considering the nonlinearities were formulated. The equations were solved using a four-order Runge-Kutta algorithm in MATLAB. The experimental models were modelled theoretically, to compare with the experimental results. Parameter analysis was carried out to study the influences on the theoretical rocking behaviour.

In sum, studies were made in discrete advancing steps which proved able to validate and supplement each other in a complementary fashion. Direct conclusions made, which are already included chapter by chapter above, can be summarised as follows:

A masonry wall subject to horizontal force may be damaged in either in-plane or out-of-plane collapse depending on the direction of the force. In-plane damage patterns vary gradually from sliding to overturning with the decrease of *L/H* ratios. In most cases, the wall is damaged in a mixed mechanism. The crack angle coincides with stagger angle of the brick course, and the direction of the main diagonal crack remains constant. Mechanisms A, B1, D, B2 and G, defined above for out-of-plane damage, occur according to the strengths of the connections at the two wall corners. Mechanism A, B1, D and B2 occur in turn as the two corners become stronger. For walls with strong connections at both corners, Mechanism G occurs with increase of the length of façade. Stronger corner connections also result in smaller collapsed wall portions. Out-of-plane behaviour is also influenced by brick bond type, the vertical pre-loading condition and geometric dimensions of the façade.

The load factor for a masonry wall relates to its geometric form, its scale, the number of bricks it contains, the stagger ratio, the bond type and the shape of brick being used. The load factor also increases with increase of friction coefficient. The out-of-plane collapse is the most likely to occur in practice. The out-of-plane load factor is clearly lower than the in-plane load factor for the same wall and is therefore the crucial value to identify when assessing the safety factor for a masonry wall. Corner connection strengths are most important in determining the magnitude of the out-of-plane load factor. In essence, better connections offer better load bearing capacities, except that very unsymmetrical corner connections in terms of strength result in walls that are particularly vulnerable to seismic attack. Walls of the same size but containing more bricks possess a poorer resistance to seismic excitation.

For the 3D model, in most cases, the out-of-plane rocking dominated the whole structural response. Separate sliding and rotation of individual bricks, to any extent, did not substantially influence the essentially continuum-like response of the model. With the decrease of façade *L/H* ratio, the predominance of out-of-plane rocking decreases and corner movements become progressively more influential on the final damage form. Corners are highly vulnerable to seismic damage in masonry structures. So corner constraint conditions, therefore, exert a substantial effect on the structural response. As to the façade itself, the excited rocking portion remains the same in size irrespective of the intensity and frequency of the excitation and is determined only by the vertical pre-loading conditions and the geometry of the façade. The excited portion is consistently divided into two parts. Integral rocking is presented globally in the two parts. The upper part, including the whole layers on the top and part of the side walls, presents a little extra rocking, clearer arching shape and more separate sliding on bricks. The lower part, then, shows smaller arching shape and little separate sliding on bricks. This also offers the experimental basis for the theoretical study.

The dynamic behaviour of the masonry structure has been shown to be frequency-sensitive. The characteristic frequency for excitations parallel to each axis depends on wall height, vertical pre-loading and façade corner constraints. A certain effective range of excitation frequencies exists, straddling the characteristic frequency within which the structural dynamic behaviour is very clear and remains similar across the range. Out-of-plane rocking predominates. Within the effective range, the wall better maintains its integrity and vibrates efficiently and any separate motions of individual bricks are lessened. Excitation frequencies outside the effective range did not generate much response even when the peak acceleration was imposed. The width of the effective range depends upon the ratio *L/H* of the façade. Façades with higher *L/H* have wider effective frequency ranges. The façade of lower *L/H* has much narrower effective ranges and bigger differences between effective and ineffective ranges. In addition, façades of lower *H* demonstrate more plastic characteristics and higher ductility and are less likely to collapse after damage is caused.

Two models are set up and analysed, which are the y-axis façade of Model II and the y-axis façade of Model III. Stable and consistent results are given by the mathematical model. The magnitudes and of experimental rocking are simulated with acceptable errors. The mechanisms of the rocking behaviour in practice are modelled properly, with integral rocking in the excited portion globally and a little extra rocking in the upper part. Pattern 3 is the most common pattern. Patterns 1 and 3 are identified as being stable, while Pattern 2 is the least likely to occur but is the most vulnerable and unstable pattern. The model shows the increased rocking

amplitude with the increase of the amplitude of excitation at certain frequency. However, limitations exist in this theoretical model. It cannot present the frequency-sensitive characteristic shown by the experimental model.

The slender façade, especially with larger mass on the upper part, presents more frequent transitions and larger rocking. The stability and characteristics of the theoretical model that are consistent with the characteristics shown in the experiments are maintained by the load and constraint on the top. The release of the top compression can induce the random rocking behaviour of the theoretical model, as a rigid body. The magnitude of restitution coefficient influences the rocking magnitudes, but cannot influence the stability and has limited effect on the patterns of rocking.

6.2 Future Work

For the static tests, the instruments can be modified so that velocity of the increasing horizontal force can be controlled and more data can be collected from the specimen. New studies can made concerning on the sliding of bricks and the angle that the crack is initiated in the in-plane collapse, as well as the arching behaviour in the out-of-plane collapse. The damage mechanism of masonry walls can be studied on the shaking table.

For the 3D masonry structure, more models in different scales can be tested on the shaking table to analyse the scale effect and the influence of the numbers of bricks within the facade. Real earthquake waves can be used as input to collect information about the more practical seismic structural behaviour. The practical conditions such as the soil, the connection conditions and the roof can be added. More specific studies can be carried out on the separate motion of bricks.

More work can be done on the mathematical model. Dynamic tests can be carried out on the rigid-body system to further validate this model. The impact and the contact at the cracked joint need more studies. The definitions of properties of the rigid body can be improved to make the two-rigid-body model closer to the reality. The arching effect on the out-of-plane rocking can be included. The consideration of possible sliding and viscous may help to better present the characteristics of the masonry structure.

References

Adams, D. (1996). "Effects of Scale and Loading Rate with Tests of Concrete and Masonry Structures." Earthquake Spectra **12**(1): 13-27.

Allen, R. and Duan, X. (1995). "Effects of Linearizing on Rocking Block." Journal of Structural engineering and mechanics **12**(7): 1146-1149.

Anagnostopoulou, M., et al. (2010). "Performance of Churches During the Darfield Earthquake of September 4, 2010." Bulletin Of The New Zealand Society For Earthquake Engineering **43**(4): 374-381.

Anderson, C. (1976). "Lateral Loading Tests on Concrete Block Walls." The Structural Engineer **54**(7): 239-246.

Benedetti, D., et al. (2001). "Evaluation of the Seismic Response of Masonry Buildings Based on Energy Functions." Earthquak Engineering and Structural Dynamics **30**: 1061–1081.

Benedetti, D., et al. (1998). "Shaking Table Tests on 24 Simple Masonry Buildings." Earthquak Engineering and Structural Dynamics **27**: 67-90.

Berto, L., et al. (2004). "Shear Behaviour of Masonry Panel: Parametric Fe Analyses." International Journal of Solids and Structures(41): 4383-4405.

Binda, L. and Saisi, A. (2005). "Research on Historic Structures in Seismic Areas in Italy." Progress in Structural Engineering and Materials **7**(2): 71-85.

Binda, L., et al. (2000). "Investigation Procedures for the Diagnosis of Historic Masonries." Construction and Building Materials **14**(4): 199–233.

Bothara, J. K., et al. (2010). "Seismic Performance of an Unreinforced Masonry Building: An Experimental Investigation." Earthquake Engineering & Structural Dynamics **39**(1): 45-68.

Caliò, I., et al. (2008). A Discrete Element Approach for the Evaluation of the Seismic Response of Masonry Buildings. The 14th World Conference on Earthquake Engineering. Beijing, China.

Casolo, S. (1999). "Rigid Element Model for Non-Linear Analysis of Masonry Facades Subjected to out-of-Plane Loading." Communications in Numerical Methods in Engineering **15**(7): 457-468.

Casolo, S. (2000). "Modelling the out-of-Plane Seismic Behaviour of Masonry Walls by Rigid Elements." Earthquake Engineering & Structural Dynamics **29**: 1797-1813.

Casolo, S., et al. (2000). "Analysis of Seismic Damage Patterns in Old Masonry Church Facades." Earthquake Spectra **16**(4): 757-773.

Cecchi, A. and Sab, K. (2002). "A Multi-Parameter Homogenization Study for Modeling Elastic Masonry." European Journal of Mechanics A/Solids **21**(2): 249-268.

Cecchi, A. and Sab, K. (2009). "Discrete and Continuous Models for in Plane Loaded Random Elastic Brickwork." European Journal of Mechanics A/Solids **28**(3): 610-625

Cohen, G. L., et al. (2004). "Seismic Evaluation of Low-Rise Reinforced Masonry Buildings with Flexible Diaphragms: Ii. Analytical Modeling." Earthquake Spectra **20**(3): 779–801.

Cundall, P. A. (1971). A Computer Model for Simulating Progressive Large Scale Movements in Blocky Rock Systems. the Symposium on Rock Fracture (ISRM), Nancy, France.

Cundall, P. A. (1988). "Formulation of a Three-Dimensional Distinct Element Model - Part I: A Scheme to Detect

and Represent Contacts in a System Composed of Many Polyhedral Blocks." International Journal of Rock Mechanics and Mining Sciences **25**(3): 107–116.

Cundall, P. A. and Hart, R. D. (1989). Numerical Modelling of Discontinua. DEM 1st U.S. Conference. Golden, Colorado, CSM Press.

D'Ayala, D. (1998). Correlation of Seismic Vulnerability and Damage between Classes of Buildings: Churches and Houses. The International Workshop on Measures of Seismic Damage to Masonry Buildings, Monselice, Padova, Italy, A. A. BALKEMA.

D'Ayala, D. (2005). "Force and Displacement Based Vulnerability Assessment for Traditional Buildings." Bulletin Of Earthquake Engineering **3**(3): 235-266.

D'Ayala, D. and Paganoni., S. (2011). "Assessment and Analysis of Damage in L'aquila Historic City Centre after 6th April 2009." Bulletin of Earthquake Engineering **9**(1): 81–104.

D'Ayala, D., et al. (2008). Dynamic Multi-Body Behaviour of Historic Masonry Buildings Models. the 6th International Conferene on Structural Analysis of Historical Construction, Bath, UK.

D'Ayala, D. and Speranza, E. (2003). "Definition of Collapse Mechanisms and Seismic Vulnerability of Historic Masonry Buildings." Earthquake Spectra **19**(3): 479-509.

Dafnis, A., et al. (2002). "Arching in Masonry Walls Subjected to Earthquake Motions." Journal of Structural Engineering **128**(2): 153–159.

Derakhshan, H., et al. (2010). Effects of Unreinforced Masonry Wall Slenderness Ratio on out-of-Plane Post-Cracking Dynamic Stability. New Zealand Society for Earthquake Engineering Conference (2010 : Wellington, New Zealand). Wellington, New Zealand, New Zealand Society for Earthquake Engineering Inc.

Dizhur, D., et al. (2011). Performance of Masonry Buildings During the 2010 Darfield (New Zealand) Earthquake. The 11st North American Masonry Conference. AE, S., JS, W., OE, B. and JR., B. P. Minneapolis, Minnesota**:** 321-339.

Doherty, K., et al. (2002). "Displacement-Based Seismic Analysis for out-of-Plane Bending of Unreinforced Masonry Walls." Earthquake Engineering and Structural Dynamics **31**(4): 833-850.

Dolce, M., et al. (2005). "Shaking Table Tests on Reinforced Concrete Frameswithout and with Passive Control Systems." Earthquake Engineering & Structural Dynamics (34): 1687–1717.

Dolce, M., et al. (1998). Damage to Buildings Due to 1997 Umbria-Marche Earthquake. The International Workshop on Measures of Seismic Damage to Masonry Buildings, Monselice, Padova, Italy, A.A.BALKEMA.

Dutta, D. (2006). Textbook of Engineering Mathematics. Delhi, New Age International Ltd.

Ehsani, M. R., et al. (1999). "Behavior of Retrofitted Urm Walls under Simulated Earthquake Loading." Journal of Composites for Construction **3**(3): 134-142.

Elvin, A. and Uzoegbo, H. C. (2011). "Response of a Full-Scale Dry-Stack Masonry Structure Subject to Experimentally Applied Earthquake Loading." Journal of the South African Institution of Civil Engineering **53**(1): 22-32.

Fujita, S., et al. (2000). "Study on Measurement Method for Structural Fracturing and Breakdown Process in Shake Table Tests." Seismic Engineering **402**(2): 225-230.

Giannini, R. and Masiani, R. (1991). "Random Vibration of the Rigid Block." Computational Stochastic Mechancis: 741-752.

Gilbert, M., et al. (2002). "The Performance of Unreinforced Masonry Walls Subjected to Low-Velocity Impacts: Mechanism Analysis." International Journal of Impact Engineering **27**(3): 253-275.

Griffith, M., et al. (2004). "Experimental Investigation of Unreinforced Brick Masonry Walls in Flexure." Journal of Structural Engineering **130**(3): 423-432.

Hammoud, M., et al. (2011). "A Coupled Discrete/Continuous Method for Computing Lattices. Application to a Masonry-Like Structure." International Journal of Solids and Structures **48**(21): 3091-3098

Hanazato, T., et al. (2008). Shaking Table Test of Model House of Brick Masonry for Seismic Construction. The 14th World Conference on Earthquake Engineering. Beijing, China.

Hart, R. D., et al. (1988). "Formulation of a Three-Dimensional Distinct Element Model — Part Ii: Mechanical Calculations." International Journal of Rock Mechanics and Mining Sciences **25**(3): 117–125.

Hendry, A. (1973). "The Lateral Strength of Unreinforced Brickwork." The Structural Engineer **51**(2): 43-50.

Hogan, S. J. (1990). "The Many Steady Stater Esponseso F a Rigid Block under Harmonic Forcing." Earthquake Engineering & Structural Dynamics **19**: 1057-1071

Housner, G. W. (1963). "The Behaviour of Inverted Pendulum Structures During Earthquakes." Bulletin of the Seismological Society of America **53**(2): 403-417.

Ishiyama, Y. (1983). Motions of Rigid Bodies and Criteria for Overturning by Earthquake Excitations. The 3rd South Pacific Regional Conference on Earthquake Engineering, Wellington.

Ismail, N., et al. (2011). Performance of Masonry Buildings During the 2010 Darfield (New Zealand) Earthquake. The 11st North American Masonry Conference. AE, S., JS, W., OE, B. and JR., B. P. Minneapolis, Minnesota**:** 1-13.

Juhasova, E., et al. (2002). "Assessment of Seismic Resistance of Masonry Structures Including Boundary Conditions." Soil Dynamics and Earthquake Engineering **22**(9-12): 1193-1197.

Koh, A. S. and Spanos, P. D. (1986). "Analysis of Block Random Rocking." Soil Dynamics and Earthquake Engineering **5**: 178-183.

L. Decanini, et al. (2004). "Performance of Masonry Buildings During the 2002 Molise, Italy, Earthquake." Earthquake Spectra **20**(18): 191-220.

L. Ramos and Lourenco, P. (2004). "Modeling and Vulnerability of Historical City Centers in Seismic Areas: A Case Study in Lisbon." Engineering structures **26**(9): 1295-1310

Lagomarsino, S. (1998). Damage Survey of Ancient Churches: The Umbria-Marche Experience. The International Workshop on Measures of Seismic Damage to Masonry Buildings, Monselice, Padova, Italy, A. A. BALKEMA.

Lagomarsino, S. and Podesta, S. (2004). "Damage and Vulnerability Assessment of Churches after the 2002 Molise, Italy, Earthquake." Earthquake Spectra **20**(1): 271-283.

Lenci, S. and Rega, G. (2006). "A Dynamical Systems Approach to the Overturning of Rocking Blocks." Chaos, Solitons and Fractals(28): 527–542.

Lestuzzi, P. and Bachmann, H. (2007). "Displacement Ductility and Energy Assessment from Shaking Table Tests on Rc Structural Walls." Engineering Structures(29): 1708–1721.

Livesley, R. K. (1978). "Limit Analysis of Structures Formed from Rigid Blocks." International Journal for Numerical Methods in Engineering **12**(12): 1853-1871.

Livesley, R. K. (1992). "A Computational Model for the Limit Analysis of Three-Dimensional Masonry Structures." Mecc **27**(3): 161-172.

Lourenço, P., et al. (2005). "Dry Joint Stone Masonry Walls Subjected to in-Plane Combined Loading." Journal of Structural Engineering **131**(11): 1665-1673.

Lourenço, P. B. (2002). "Computations on Historic Masonry Structures." Progress in Structural Engineering and Materials **4**(3): 301-319.

Lourenco, P. and Ramos, L. (2004). "Characterization of Cyclic Behavior of Dry Masonry Joints." Journal of Structural Engineering **130**(5): 779–786.

Lu, X., et al. (2007). "The Structural Design of Tall and Special Buildings." Design Tall Spec. Build(16):

131–164.

Magenes, G. and Calvi, G. (1997). "In-Plane Seismic Response of Brick Masonry Walls." Earthquak Engineering and Structural Dynamics **26**: 1091-1112.

Magenes, G. and Calvi, G. M. (1998). "In-Plane Seismic Response of Brick Masonry Walls." EARTHQUAKE ENGINEERING AND STRUCTURAL DYNAMICS **26**(11): 1091-1112.

Magenes, G., et al. (2010). A Full-Scale Shaking Table Test on a Two-Storey Stone Masonry Building. 14th European Conference on Earthquake Engineering. Ohrid, Republic of Macedonia.

Manos, G. C. and Clough, R. W. (1986). Earthquake Simulated Performance of an Unreinforced and a Reinforced Masonry Single-Story House Model. The 3rd U. S. National Conference on Earthquake Engineering, Charleston, SC, USA, Earthquake Engineering Research Inst, El Cerrito, CA, USA.

Martini, K. (1998). "Ancient Structures and Modern Analysis: Investigating Damage and Reconstruction at Pompeii." Automation in Construction(8): 125-137.

Mendola, L. L., et al. (1995). "Stability of Masonry Walls Subjected to Seismic Transverse Forces." Journal of Structural Engineering **121**(11): 1581–1587.

Menon, A. and Magenes, G. (2011a). "Definition of Seismic Input for out-of-Plane Response of Masonry Walls: I. Parametric Study." Journal of Earthquake Engineering **15**(2): 165-194.

Menon, A. and Magenes, G. (2011b). "Definition of Seismic Input for out-of-Plane Response of Masonry Walls: Ii. Formulation." Journal of Earthquake Engineering **15**(2): 195-213.

Munjiza, A., et al. (1995). "A Combined Finite/Discrete Element Method in Transient Dynamics of Fracturing Solids." Engineering Computations **12**(2): 145 - 174.

Nakagawa, T., et al. (2011). "Collapse Behavior of a Brick Masonry House Using a Shaking Table and Numerical Simulation Based on the Extended Distinct Element Method." Bulletin of Earthquake Engineering.

Owen, D. R., et al. (1995). Reinforcement Concrete Models for Combined Finite/Discrete Analysis. the Fifth International Conference on Reliability of Finite Element Methods for Engineering Computations, Amsterdam, The Netherlands.

Owen, D. R., et al. (1998). Finite/Discrete Element Models for Assessment and Repair of Masonry Structures. Conference on Arch Bridges, Balkema, Rotterdam.

Paquette, J., et al. (2004). "Seismic Testing of Repaired Unreinforced Masonry Building Having Flexible Diaphragm." Journal of Structural Engineering **130**(10): 1487-1496.

Paquette, J., et al. (2001). "Out-of-Plane Seismic Evaluation and Retrofit of Turn-of-the-Century North American Masonry Walls." Journal of Structural Engineering **127**(5): 561-569.

Peña, F., et al. (2007). "On the Dynamics of Rocking Motion of Single Rigid-Block Structures." Earthquake Engineering & Structural Dynamics **36**(15): 2383-2399.

Pietruszczak, S. and Ushaksaraei, R. (2003). "Description of Inelastic Behaviour of Structural Masonry " International Journal of Solids and Structures **40**(15): 4003-4019.

Pompei, A., et al. (1998). "Dynamics of Rigid Block Due to Horizontal Ground Motion." Journal of Engineering Mechanics **124**(7): 713-717.

Psycharis, I. (1990). "Dynamic Behaviour of Rocking Two-Block Assemblies " Earthquake Engineering and Structural Dynamics **19**: 555-575.

Ren, X., et al. (2008). "An Analytical Approach to Seismic Damage Information of the Masonry Buildings in Qinchuan County under 5.12 Wenchuan Earthquake Collected in Site Urgent Structural Evaluation " Structural Engineers.

Scalia, A. and Sumbatyan, M. A. (1996). "Slide Rotation of Rigid Bodies Subjected to a Horizontal Ground Motion." Earthquake Engineering and Structural Dynamics **25**(1): 139-149.

Shenton, H. W. (1996). "Criteria of Initiation of Slide, Rock, and Slide-Rock Rigid-Body Modes." Journal of Engineering Mechanics **122**(7): 690-693

Shi, Y. and D'Ayala, D. (2006). Analysis of in-Plane Damage of Unreinforced Masonry Walls. the 7th International Masonry Conference, London, UK, British Masonry Society.

Shi, Y., et al. (2008). Analysis of out-of-Plane Damage Behaviour of Unreinforced Masonry Walls. the 14th International Brick and Block Masonry Conference Sydney, Australia.

Sinha, B. (1978). "A Simplified Ultimate Load Analysis of Laterally Loaded Model Orthotropic Brickwork Panels of Low Tensile Strength." Structural Engineer **56**(4): 81-84.

Sinopoli, A. (1997). "Unilaterality and Dry Friction: A Geometric Formulation for Two-Dimensional Rigid Body Dynamics." Nonlinear Dynamics **12**: 343–366.

Sorrentino, L., et al. (2011). "The Relevance of Energy Damping in Unreinforced Masonry Rocking Mechanisms. Experimental and Analytic Investigations." Bulletin of Earthquake Engineering **9**(5): 1617-1642.

Spanos, P. D., et al. (2001). "Dynamic Analysis of Stacked Rigid Blocks." Soil Dynamics and Earthquake Engineering **21**: 559-578.

Stewart, D. E. (2000). "Rigid-Body Dynamics with Friction and Impact " SIAM Review **42**(1): 37.

Su, Q. and Zhao, S. (2010). "A Rapid Seismic Evaluation Method of Masonry Buildings Based on Earthquake Damage." Advanced Materials Research(893): 163-167.

Tomazevic, M., et al. (1996). "Seismic Behavior of Masonry Walls: Experimental Simulation." Journal of Structural Engineering **122**(9): 1040-1047.

Tomazevic, M. and Weiss, P. (2010). "Displacement Capacity of Masonry Buildings as a Basis for the Assessment of Behavior Factor: An Experimental Study." Bulletin of Earthquake Engineering **8**(6): 1267-1294.

Tominaga, Y. and Nishimura, Y. (2008). Experimental Study on Strucyural Performance of Historic Brick Masonry Buildings. The 14th World Conference on Earthquake Engineering. Beijing, China.

Trovalusci, P. and Masiani, R. (2005). "A Multifield Model for Blocky Materials Based on Multiscale Description." International Journal of Solids and Structures **42**(21-22): 5778-5794.

Wei, W., et al. (2008). "Lessons Learnt from Masonry Structural Damage in 2008 Wenchuan Earthquake." Earthquake Resistant Engineering and Retrofitting.

West, H., et al. (1977). "The Resistance of Brickwork to Lateral Loading." The Structural Engineer **55**(10): 411-421.

Wight, G. D., et al. (2007). "Shake Table Testing of Posttensioned Concrete Masonrywalls with Openings." Journal of Structural Engineering **133**(11): 1551–1559.

Yi, T., et al. (2006). "Lateral Load Tests on a Two-Story Unreinforced Masonry Building." Journal of Structural Engineering **132**(5): 643-652.

Yim, C.-S., et al. (1980). "Rocking Response of Rigid Blocks to Earthquakes." Earthquake Engineering and Structural Dynamics **8**(6): 567-587.

Yim, C. S. and Lin, H. (1991). "Nonlinear Impact and Chaotic Response of Slender Rocking Objects." Journal of Engineering Mechanics **117**(9): 2079-2100.

Zhu, H. and Wu., M. (2002). "The Characteristic Receptance Method for Damage Detection in Large Mono-Coupled Periodic Structures." Journal of Sound and Vibration **251**(2): 241~259.

Zucchini, A. and Lourenco, P. B. (2004). "A Coupled Homogenisation–Damage Model for Masonry Cracking." Computers and Structures(82): 917-929.

Appendix I Classification of the Shaking-table Experiments

Group	Test No.	Input signal			Model	
		Direction	Frequency	Amplitude	No. of layers	Additional mass
1	1	y	1.8Hz	12.00mm	9	NA
	2		2.0Hz			
	3		2.2Hz			
	4		2.5Hz			
	5		3.6Hz			
	6		5.4Hz			
	7		3.6Hz			
	8		5.4Hz			
2	1	y	1.7Hz	13.45mm	9	NA
	2		1.8Hz	12.00mm		
	3		2.0 Hz	9.70mm		
	4		2.5 Hz	6.00mm		
	5		3.6 Hz	3.00mm		
3	1	y	1.8Hz	12.00mm	9	5N mass on each corner
	2		2.0 Hz	9.70mm		
	3		2.5 Hz	6.00mm		
	4		3.6 Hz	3.00mm		
4	1	x	1.7Hz	12.00mm	9	NA
	2		1.8Hz			
	3		1.85Hz			
	4		1.9Hz			
	5		2.0Hz			
	6		2.2Hz			
	7		2.5Hz			
	8		3.6Hz			
	9		5.4Hz			
5	1	x	1.8 Hz	13.37mm	9	NA
	2		1.9 Hz	12.00mm		
	3		2.0 Hz	10.83mm		
	4		2.5 Hz	6.93mm		
	5		3..8 Hz	2.00mm		

Group	Test No.	Input signal			Model	
		Direction	Frequency	Amplitude	No. of layers	Additional mass
6	1	x	1.8 Hz	13.37mm	9	5N mass on each corner
	2		1.9 Hz	12.00mm		
	3		2.0 Hz	10.83mm		
	4		2.5 Hz	6.93mm		
	5		3..8 Hz	2.00mm		
7	1	x, y	1.7 Hz	9.50mm	9	5N mass on each corner
	2		1.8 Hz	8.50mm		
	3		1.9 Hz	7.62mm		
	4		2.0 Hz	6.86mm		
	5		2.5 Hz	4.24mm		
	6		3.6 Hz	2.12mm		
8	1	y	0.5 Hz	5.00mm	15	5N mass on each corner
	2		0.6 Hz			
	3		0.7 Hz			
	4		0.9 Hz			
	5		1.3 Hz			
	6		1.6 Hz			
	7		2.2 Hz			
	8		2.4 Hz			
	9		2.5 Hz			
9	1	y	2.5 Hz	5.00mm	15	5N mass on each corner
	2		2.2 Hz	6.46mm		
	3		3.6 Hz	2.41mm		

Appendix II the Flow Chart of the Mathematical Model

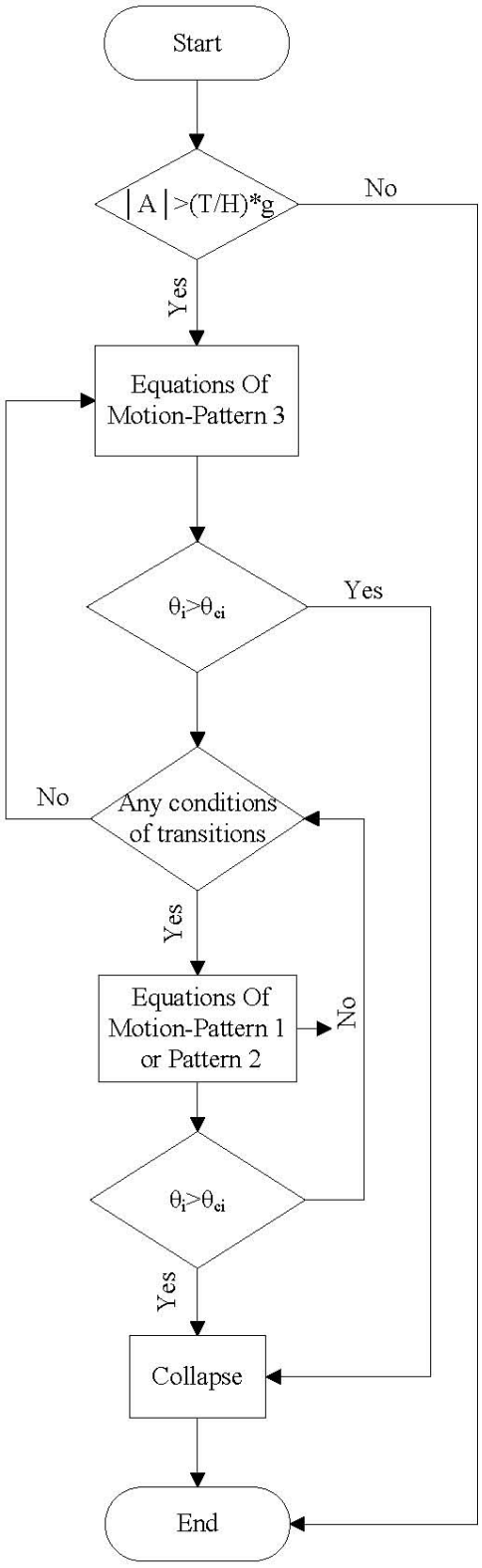

Figure II.1 The Flow Chart of the Rocking Process